

**STUDIES ON FERROELECTRIC AND MULTIFERROIC
MATERIALS FOR TUNNEL JUNCTION APPLICATIONS**

By

DANILO GREGORIO BARRIONUEVO DIESTRA

A thesis submitted in partial fulfillment of the requirements for the Degree of

DOCTOR OF PHILOSOPHY

Supervised by

Professor Ram S. Katiyar

San Juan, Puerto Rico

May 2016

**STUDIES ON FERROELECTRIC AND MULTIFERROIC
MATERIALS FOR TUNNEL JUNCTION APPLICATIONS**

**ACCEPTED BY FACULTY OF THE CHEMICAL PHYSICS PROGRAM OF
THE UNIVERSITY OF PUERTO RICO IN PARTIAL FULFILLMENT OF THE
REQUIREMENTS FOR THE DEGREE OF DOCTOR OF PHILOSOPHY**

Dr. Ram S. Katiyar
THESIS ADVISOR

Dr. Carlos Cabrera
THESIS COMMITTEE MEMBER

Dr. Gerardo Morell
THESIS COMMITTEE MEMBER

Dedicated to

*My parents Gregorio and Fermina,
my sister Olinda and brothers Hugo and Percy*

ABSTRACT

Due to the evolution of device miniaturization and the potential applications for new nonvolatile memory devices, the ferroelectric/multiferroic tunnel junctions are an emerging paradigm for these applications. Typical ferroelectric tunnel junctions (FTJs) consist of a few unit cells of a ferroelectric material sandwiched between two electrodes where the interplay of ferroelectricity and electron tunneling occurs. The electrical junction resistance can be manipulated reversibly via the polarization direction of the ferroelectric tunnel barrier, a phenomenon known as the tunneling electroresistance (TER) effect. FTJs have attracted interest both for the basic physics which is involved in controlling two conductance states (high resistance state (HRS) and low resistance state (LRS)) and for their potential applications with a resistance ratio of two orders of magnitude, in nanoelectronics operating with low power consumption. Realization of this idea is a task with many obstacles, because it requires fabrication of ultrathin films retaining pronounced ferroelectric properties at a thickness of only a few unit cells. For this reason, we started studying the thickness effect on the ferroelectric properties of $\text{PbZr}_{0.52}\text{Ti}_{0.48}\text{O}_3$ (PZT).

We have synthesized $\text{PZT}/\text{La}_{0.67}\text{Sr}_{0.33}\text{MnO}_3$ (LSMO) heterostructured films of a range of thicknesses (10-100 nm) on (001) $(\text{LaAlO}_3)_{0.3}(\text{Sr}_2\text{AlTaO}_6)_{0.7}$ (LSAT) substrates using a multi-target pulsed laser deposition (PLD) system. The dielectric anomalies and magnetic phase transition temperatures were shifted to lower temperatures with decreasing thickness of PZT films. Ferroelectric behavior persisted in films down to as thin as 10 nm.

After seeing that ferroelectricity could be retained at PZT-film thicknesses of only few nanometers, we fabricated the ferroelectric tunnel junction. Here, we demonstrated room temperature polar switching and tunneling behavior in PZT ultra-thin films of 3-7 nm thick, sandwiched between platinum and ferromagnetic LSMO layers. This junction also shows magnetic field dependent tunnel current switching in Pt/PZT/LSMO heterostructures. The effect of ferroelectric switching was observed in current density versus voltage curves with a large variation in the high-resistance/low-resistance (HRS/LRS) ratio (2:1 to 100:1, for different samples). However, these effects were more prominent in the presence of an in-plane external magnetic field. The effect of a magnetic field along the in-plane direction was observed when 10 kG was applied to the junction during J(V) measurements. The resistance decreased only in the positive voltage range (controlled by the LSMO electrode), while no significant change was observed in the negative voltage range (controlled by the Pt electrode). This is reasonable considering that LSMO becomes more metallic in its ferromagnetic state. For this LSMO/PZT junction, the resistance switching between LRS and HRS became sharper and the HRS/LRS ratio values at zero bias were ~60 at 0 G and 110 at 10 kG. The conductance curve fit Brinkman's model and the parabolic conductance upon bias voltage implies transport is governed by electron tunneling.

Another interesting type of tunnel junction is the multiferroic tunnel junction (MFTJ). MFTJs have two configurations: 1) a FTJ with ferromagnetic electrodes and 2) a multiferroic barrier sandwiched by a normal metal and a ferromagnet. This device shows four-resistance states: two states of the electroresistance effect and two states of magnetoresistance effect (when the current flows between two ferromagnets separated by

an ultrathin insulator, the total resistance of the device, in which tunneling is responsible for current flowing, changes with the relative orientation of the two magnetic layers). We are interested in the latter configuration, which employs a multiferroic barrier. However, most multiferroic materials exhibit multiferroic properties at low temperatures. This makes them limited for practical applications. For these reasons, $\text{Pb}(\text{Zr}_{0.53}\text{Ti}_{0.47})_{0.60}(\text{Fe}_{0.5}\text{Ta}_{0.5})_{0.40}\text{O}_3$ (PZTFT) is a good candidate for these applications, because this material is a single-phase magnetoelectric multiferroic at room temperature (this material was discovered in our laboratory). The four-resistance-state with multiferroic tunnel junctions has been reported by several researchers, however, these devices required liquid helium to operate, as the four-resistance-state was obtained at low temperature (10 K). For practical applications, devices need to work at room temperature. For this reason, we choose the PZTFT multiferroic material.

In this part of the study, we focused on the effect of the thickness of PZTFT on its magnetic and ferroelectric properties. We grew films of PZTFT on LSMO/LSAT (001) substrates with film thicknesses ranging from 4 to 80 nm, by PLD. Well saturated ferroelectric loops were observed for PZTFT with remnant polarizations of 43, 32, 25 and 10 $\mu\text{C}/\text{cm}^2$ for films of thicknesses 80, 50 and 20 nm respectively. An enhanced saturated magnetization was observed with increasing PZTFT layer thickness in PZTFT/LSMO heterostructures. At room temperature, we obtained polarization switching and stripe domains at 7 nm using piezoresponse and magnetic force microscopy that confirmed a multiferroic nature at the nanoscale level, thin enough for tunnel junctions. These devices work at room temperature and for this reason, PZTFT is good candidate for multiferroic tunnel junction applications.

ACKNOWLEDGEMENTS

I would like to express my sincere gratitude to my advisor, Prof. Ram S. Katiyar for giving me the opportunity to work on this exciting project and more importantly, proper guidance and support throughout the course of my Ph.D. research.

I would especially like to thank Dr. Nora Ortega, J. F. Scott, and Dr. Ashok Kumar, for helping in experimental work, for discussions and also for moral support, during my Ph. D research.

I would like to thank the other members of my Ph.D. committee, Prof. Gerardo Morell and Prof. Carlos Cabrera for taking time out of their busy schedules to evaluate my work.

Additionally, I would like to thank:

- Professor A. Sokolov (University of Nebraska-Lincoln) for transport properties measurements.
- Ms. Le Zhang (University of Nebraska-Lincoln) for transport properties measurements.

I also thank the entire group of SPECLAB members: William Pérez, Anand Gaur, Dilsom Sanchez, Alvaro Instan, Dhiren Pradhan, Geetika Khurana, Shalini Kumari, Adriana M. Rivera, Shojan Pavunny, Rajesh Katiyar, Loraine Torres, Yogesh Sharma and Radhe Agrawal. It is your constant efforts to create and maintain friendly and a cooperative atmosphere in the laboratory that made my Ph.D. work more fun.

I would like to thank Dr. Jamie Scott for review this document.

Finally, I want to thank my parents, my brothers and my sister for their love, enthusiasm and support. I would never have gone this far without their unwavering belief and support.

TABLE OF CONTENTS

ABSTRACT.....	IV
ACKNOWLEDGEMENTS.....	VII
TABLE OF CONTENTS.....	IX
LIST OF TABLES.....	XIV
LIST OF FIGURES.....	XV
LIST OF ABBREVIATIONS.....	XX
PUBLICATIONS AND PRESENTATIONS.....	XVII

CHAPTER 1

INTRODUCTION.....	1
1.1. FERROELECTRIC MATERIALS.....	1
1.1.1 Ferroelectricity	1
1.1.2 Piezoelectricity.....	4
1.1.3 Lead Zirconate Titanate $\text{Pb}(\text{Zr,Ti})\text{O}_3$ (PZT) - Perovskite	5
1.2. FERROMAGNETIC MATERIALS	7
1.2.1 Ferromagnetic effect.....	7
1.2.2 Lanthanum strontium manganite $(\text{La, Sr})\text{MnO}_3$ (LSMO) - Perovskite.....	9
1.3. MULTIFERROIC MATERIALS.....	12
1.3.1 Multiferroics.....	12
1.3.2 Magnetoelectric coupling.....	14
1.3.3 Lead Iron Tantalate-Lead Zirconate Titanate $\text{Pb}(\text{Fe,Ta})\text{O}_3\text{-Pb}(\text{Zr,Ti})\text{O}_3$ (PZTFT) - Perovskite	16

1.4. FERROELECTRIC AND MULTIFERROIC TUNNEL JUNCTIONS.....	18
1.4.1 Theory of ferroelectric and multiferroic tunnel junctions.....	22
1.4.2 Critical thickness for ferroelectricity.....	25
1.4.3 Effect of the depolarization field	26
1.4.4 Role of interface on ferroelectricity at the nanoscale.....	27
REFERENCES	30

CHAPTER 2

EXPERIMENTAL AND CHARACTERIZATION TECHNIQUES.....	35
2.1. EXPERIMENTAL.....	35
2.1.1 Pulsed laser deposition (PLD).....	35
2.2. STRUCTURAL AND MICROSTRUCTURE CHARACTERIZATION.....	37
2.2.1 X-ray diffraction technique.....	37
2.2.2 Atomic force microscopy (AFM).....	39
3. ELECTRICAL CHARACTERIZATION.....	41
2.3.1 Dielectric and impedance measurements.....	41
2.3.2 Ferroelectric measurements.....	41
2.3.3 Top electrode	42
2.3.4 Piezoresponse force microscopy (PFM).....	42
2.4. MAGNETIC CHARACTERIZATION.....	44
2.4.1 Vibration Sample Magnetometer (VSM).....	44
2.4.2 Superconducting Quantum Interference Device Magnetometer (SQUID).....	46

2.4.3 Physical Property Measurement System (PPMS).....	47
2.4.3.1 Theory of operation.....	48
2.4.4 Magnetic force microscopy (MFM).....	50
2.5. TRANSPORT PROPERTIES.....	52
2.5.1 Current-voltage characteristics.....	52
REFERENCES.....	53

CHAPTER 3

THICKNESS DEPENDENT FUNCTIONAL PROPERTIES OF MULTIFERROIC HETEROSTRUCTURES.....	54
3.1. INTRODUCTION.....	54
3.2. EXPERIMENTAL DETAILS.....	57
3.2.1 Growth of PZT and LSMO bilayer thin films by pulsed laser deposition.....	57
3.2.2 Structural, ferroelectric and magnetic experimental details.....	57
3.3. STRUCTURAL CHARACTERIZATION.....	59
3.4. DIELECTRIC CHARACTERIZATION.....	63
3.4.1 Dielectric properties.....	63
3.4.2 Dielectric permittivity properties.....	66
3.4.3 Dielectric spectroscopy.....	68
3.5. FERROELECTRIC PROPERTIES.....	70
3.6. MAGNETIC PROPERTIES.....	73
REFERENCES.....	76

CHAPTER 4

FERROELECTRIC TUNNEL JUNCTION.....	79
4.1 INTRODUCTION	79
4.2. EXPERIMENTAL DETAILS.....	81
4.2.1 PZT and LSMO bilayer ultrathin films grown by pulsed laser deposition....	81
4.2.2 Structural, ferroelectric, and transport experimental details.....	81
4.3. STRUCTURAL CHARACTERIZATION.....	82
4.4. FERROELECTRIC PROPERTIES.....	86
4.5. TRANSPORT PROPERTIES.....	88
4.6. CAPACITANCE VOLTAGE CHARACTERISTICS.....	91
4.7. TRANSPORT PROPERTIES UNDER A MAGNETIC FIELD.....	94
REFERENCES.....	98

CHAPTER 5

FERROELECTRIC CAPPED MAGNETIZATION IN TUNNEL JUNCTIONS.....	101
5.1 INTRODUCTION	101
5.2. EXPERIMENTAL DETAILS.....	104
5.2.1 PZT/LSMO ultrathin films grown by pulsed laser deposition.....	104
5.2.2 Structural, XPS and magnetic experimental details	105
5.3. STRUCTURAL CHARACTERIZATION.....	105
5.4. FERROELECTRIC PROPERTIES.....	107

5.5. MAGNETIC PROPERTIES.....	107
5.5. X-RAY PHOTOELECTRON SPECTROSCOPY (XPS).....	110
REFERENCES.....	114

CHAPTER 6

THICKNESS DEPENDENT MULTIFERROIC PROPERTIES OF PZTFT...	116
6.1. INTRODUCTION	116
6.2. EXPERIMENTAL DETAILS.....	118
6.2.1 PZTFT and LSMO bilayer thin films grown by pulsed laser deposition.....	118
6.2.2 Structural, ferroelectric, magnetic and transport experimental details.....	118
6.3. STRUCTURAL AND SURFACE MORPHOLOGY CHARACTERIZATION	120
6.4. DIELECTRIC PROPERTIES.....	122
6.5. FERROELECTRIC PROPERTIES.....	126
6.6. MAGNETIC PROPERTIES.....	129
6.7. MULTIFERROIC PROPERTIES AT NANOSCALE LEVEL.....	137
6.8. TRANSPORT PROPERTIES.....	140
REFERENCES.....	145

CHAPTER 7

7.1. CONCLUSIONS.....	149
------------------------------	-----

LIST OF TABLES

3.1. Grain size, average (R_a) and root mean square (R_{rms}) surface roughness obtained from atomic force microscope images for different thickness of the PZT layer deposited on deposited on LSMO(60 nm)/LSAT.....	62
4.1. The experimental barrier thickness (d_{exp}) and barrier thickness (d), average barrier height ($\bar{\varphi}$) and asymmetry in the barrier height ($\Delta\varphi$) obtained using Brinkman model in the low resistance state (LRS).....	91

LIST OF FIGURES

1.1 Schematic illustration of the variation of the (a) dielectric constant, ϵ_r , and the (b) spontaneous polarization, P_s , with temperature, for Barium titanate (BaTiO_3) with $T_C = 120^\circ\text{C}$	2
1.2 Schematic diagram of a typical ferroelectric hysteresis loop.....	3
1.3 The cubic perovskite structure. Displacement of Zr-Ti ions with the application of positive and negative electric fields.....	5
1.4 Different composition corresponds to different crystallite structures. Note the morphotropic phase boundary (MPB), at a composition of 52% lead zirconate to 48% lead titanate.....	6
1.5 (a) The M-H hysteresis loop of a typical ferromagnetic material.....	8
1.6 Unit cell of LSMO. The manganese atom (green) is surrounded by an oxygen octahedron (red). The atoms at the yellow sites can be either lanthanum or strontium.....	10
1.7 $\text{La}_{1-x}\text{Sr}_x\text{MnO}_3$ phase diagram system for $0 \leq x \leq 1$. C, T, R, O*, O', and O ⁺ denote, respectively, the cubic $Pm\bar{3}m$, tetragonal $I4/m\bar{c}m$, rhombohedral $R\bar{3}c$, two orthorhombic $Pbmn$, and orthorhombic $Fmmm$ structural phases. AF-A, AF-C, and AF-G stand for the antiferromagnetic phases of the A, C, and G type, respectively OO denotes the region of stability of the orbital and charge ordered, insulating, ferromagnetic phase. "Ins." stands for "insulating".....	11
1.8 (a) Relationship between multiferroic and magnetoelectric materials. Illustrates the requirements to achieve both in a material. (b) Schematic illustrating different types of coupling present in materials. Much attention has been given to materials where electric and magnetic order is coupled. These materials are known as magnetoelectric materials.....	13
1.9 Complex domain structures in PZTFT single crystal. Transmission electron microscopy (TEM) reveals the single crystal structure of the material. It seems that all the domain variants have formed from a single higher symmetry parent state, as the selected area diffraction patterns from different regions, indicated by the coloured circles in (b), are indistinguishable. Scale bar, 200 nm.	17
1.10 Modest magnetic fields induce partially reversible changes in ferroelectric domains. Phase images from lateral piezoresponse force microscopy (LPFM) change depending on the orientation of the magnetic field applied to the PZTFT lamella. Both the images in (a) and the area histograms of different phase colours (b) illustrate that 3 kOe applied in a nominally positive direction, perpendicular to	

the lamellar surface, favours the growth of polarization directions indicated in red. When applied in a nominally negative direction, these regions contract. Scale bar, 2 nm.....	18
1.11 Schematics of a ferroelectric tunnel junction consisting of two electrodes separated by a nm-thick ferroelectric barrier layer. The ferroelectric nature of the barrier changes the transmission probability in three ways (#1,#2,#3).....	22
1.12 (a) FE tunnel junction (FTJ), (b), and (c) MF tunnel junctions (MFTJ). Ferroelectric (FE), ferromagnetic metallic (FM), multiferroic (MF) and Metal (M).....	25
2.1 Configuration of PLD chamber.....	36
2.2 Bragg's law.....	38
2.3 Contact AFM concepts (Steps 1-5)	40
2.4 Schematic of piezoresponse measurement in contact mode AFM.....	43
2.5 Schematic of a VSM system. The signal in the pick-up coils is caused by the flux change produced by the moving magnetic sample.....	45
2.6 Two parallel Josephson junctions. SQUID.....	46
2.7 Operating principle for the VSM option.....	49
2.8 MFM Lift Mode principles	50
2.9 Topographic (left) and magnetic force gradient image (right) of metal evaporated tape at 100 nm	51
3.1 (a) A sketch of the PZT thin films sandwiched between Pt top and LSMO bottom electrodes, (b) θ -2 θ diffractograms for PZT films grown on LSMO (60 nm) coated LSAT (001) substrate for thicknesses ranging from 10 nm to 100 nm, (c) and (d) show a close view of (001) and (002) XRD reflections respectively.....	60
3.2 Atomic force microscopy (AFM) topography images, of 3 μm x 3 μm x 30 nm Z-scale of PZT films with thickness: a) 100 nm, b) 50 nm, c) 25 nm, and d) 10 nm, deposited on LSMO(60 nm)/LSAT. Insets show the 3D topography images area of 1 μm x 1 μm x 30 nm Z-scale respectively.....	61
3.3 Frequency dependence of the (a) real part (ϵ') (b) imaginary part (ϵ'') of dielectric permittivity and (c) thickness dependence of ϵ' for PZT/LSMO bilayer structures with different thickness of PZT	64

3.4 (a) Temperature dependence relative permittivity complex plane plot (ϵ'' vs. ϵ') for PZT/LSMO/LSAT structures for different thickness of PZT film. (b) Comparison of ϵ'' vs. ϵ' plots for different thickness of PZT at various temperatures.....	67
3.5 Temperature dependent (a) real and (b) imaginary dielectric permittivity for PZT/LSMO/LSAT structures for different thickness of PZT film.....	69
3.6 Room temperature ferroelectric hysteresis loops for: (a) P25 heterostructure thin film at different voltages at 2 kHz. (b) PZT/LSMO/LSAT structures for different thickness of PZT film (from 100 nm to 10 nm) at 5 V and 2 kHz. (c) PZT film thickness dependence of the remanent polarization (P_r) and electric coercive field (E_c).....	71
3.7 Ferromagnetic hysteresis loop at (a) 300 K, (b) 5 K and temperature dependent magnetization for PZT/LSMO/LSAT structures for different thickness of PZT film (from 100 nm to 10 nm).....	74
4.1 (a) XRD patterns for PZT ultra-thin films grown on LSMO (30 nm) coated LSAT (001) substrate for thickness from 3 nm (P3) to 7 nm (P7). (b) RHEED patterns of LSAT (001) substrate before deposition; and after deposition of: 30 nm of LSMO film, 3 nm (P3), 5 nm (P5) and 7 nm (P7) of ultrathin films of PZT.	83
4.2 Atomic force microscopy (AFM) surface topography images, of $3 \times 3 \mu\text{m}^2$ having 5 nm in Z-scale of (a) LSMO/LSAT, PZT ultra-thin films with thickness: (b) 7 nm- P7, (c) 5 nm- P5, and (d) 3 nm- P3, deposited on LSMO(30 nm)/LSAT.	85
4.3 Piezoresponse force microscopy (PFM) measurements shows: (a) Polarization switching images for P7, P5, and P3 ultra-thin films. PFM phase and amplitude hysteresis loops measured in two configurations (b) Tip/P7/LSMO and (c) LSMO/P7/LSMO, where P7 represents 7 nm thick of PZT barrier.....	87
4.4 Brinkman's model fitting of the low-resistance conductance-voltage curves for: (a) 5 nm and (b) 7 nm thick of $\text{PbZr}_{0.52}\text{Ti}_{0.48}\text{O}_3$ ultrathin films at two different temperatures (80 K and 297 K).....	89
4.5 Evolution of the capacitance-voltage curve for Pt/P5/LSMO junction at different applied DC voltage (a) 2 V and (b) 3 V. (c) The resistance vs voltage curve exhibited resistance switching properties for the junction.....	93
4.6 (a) Current density versus voltage $J(V)$ curves of the sample P7 showing highly reproducible resistance switching at +2.7 V for a junction area of $64 \mu\text{m}^2$. Left side inset show $J(V)$ loop for the same sample with a junction area of $4 \mu\text{m}^2$. Right side inset present the $J(V)$ curve for sweep voltages from ± 1.1 V to ± 1.5 V. (b) $J(V)$ switching curves of another junction from the same P7 sample showing	

the effect of an applied 10 kG magnetic field.....	95
5.1 The XRD patterns of PZT (5 nm and 7 nm)/LSMO/LSAT heterostructures oriented along the (001/002) plane. Inset illustrates their 3D PFM images under (+/- 3V).....	106
5.2 M-T graphs of PZT/LSMO(30 nm)/LSAT heterostructures; (a) 5-nm PZT capping; (b) 7-nm PZT capping [at 100 and 1000 Oe magnetic field]. The inset of Fig. 2 (b) shows dM/dT as function of temperature at 1000 Oe field.....	108
5.3 M-H graphs of PZT (5 nm and 7 nm)/LSMO(30 nm)/LSAT heterostructures at 50 K; inset shows applied field dependence up to 1.0 T.....	109
5.4 (a-d) The core-level XPS spectra of Pb 4p _{3/2} , Mn 2p _{3/2} , and Mn 3s peaks: (a) Pb 4p _{3/2} , Mn 2p _{3/2} for 5-nm PZT capping; (b) Pb 4p _{3/2} , Mn 2p _{3/2} for 7-nm PZT capping; (c) Mn 3s for 5-nm PZT capping; and (d) Mn 3s for 7-nm PZT capping...	111
5.5 (a-f) Show the core level XPS spectra of (a) Ti 2p _{3/2} , Ti 2p _{1/2} , for 5-nm PZT capping; (b) Ti 2p _{3/2} , Ti 2p _{1/2} , for 7-nm PZT capping; (c) comparative Ti 2p peaks; (d) comparative Pb 4f peaks; (e) Zr 3d peaks; and (f) O1s peaks for both 5- and 7-nm PZT capping.....	112
6.1 (a) XRD patterns for different PZTFT thicknesses grown on LSMO/LSAT show only peaks of these materials without any additional second phase. (b) The effect of thickness on crystallization, possibly due to the quick increase of compressive stresses with a decrease in film thickness due to PZTFT and LSMO lattice mismatch.....	120
6.2 Atomic force microscopy surface topography images for different PZTFT thicknesses: (a) 80 nm, (b) 50 nm, (c) 20 nm, (d) 7 nm, (e) 5 nm, and (f) 4 nm. The reduction in roughness with decreasing film thickness may be due to a reduction in grain size.....	122
6.3 (a) The dielectric constant (ϵ_r), and (b) loss tangent ($\tan \delta$) versus frequency for different thicknesses of PZTFT at room temperature. (c), (d), (e) and (f) show Cole-Cole plots of the temperature-dependent dielectric permittivity real (ϵ') and imaginary (ϵ'') parts for different thicknesses. The semicircles imply a single relaxation time.....	124
6.4 The ferroelectric hysteresis loops for different thickness (a) 80 nm, (b) 50 nm and (c) 20 nm PZTFT at room temperature. An increase in remnant polarization and coercive field was observed with increasing voltage. (d) The reduction of the polarization when the thickness of PZTFT is reduced to 20 nm.....	127
6.5 Shows the values of remnant polarization and coercive field for different	

thicknesses of PZTFT. The ferroelectric properties are dependent on the grain size of the films; this behavior has been reported by many researchers.	128
6.6 The magnetization versus magnetic field for PZTFT/LSMO hetero-structures at (a) 5K and (b) 300 K for different thicknesses of PZTFT. In all samples ferromagnetic behavior and a decrease in saturated magnetization was observed with decreasing PZTFT thickness.....	130
6.7 Magnetization versus magnetic field for the range (-10 to 10 kOe); the ferromagnetic properties of the LSMO and PZTFT/LSMO hetero-structures for different thicknesses of PZTFT at (a) 5 K and (b) 300 K.....	131
6.8 Magnetization versus magnetic field for pure PZTFT 300 nm thick at (a) 5 K and 300 K showing the ferromagnetic properties of the PZTFT films; (b) the small hysteresis loop at room temperature.....	133
6.9 The magnetization versus temperature for PZTFT/LSMO hetero-structures for different thicknesses of PZTFT. (a) The irreversible ZFC and FCC curves show the presence of glassy behavior; (b) The transition temperature decreases when the PZTFT thickness was decreased.....	135
6.10 The magnetization versus temperature for PZTFT/LSMO hetero-structures for different thicknesses of PZTFT. The irreversible ZFC and FCC curves show the presence of glassy behavior. Ergodic temperature increases when the PZTFT thickness was decreased.....	136
6.11 (a) and (b) show the magnetization versus temperature of 300 nm thick pure PZTFT films.....	138
6.12 The multiferroic properties of ultrathin 7-nm PZTFT films. (a) shows the switching polarization of 7-nm PZTFT using piezoresponse force microscopy, and (b) displays the stripe magnetic domains for ultrathin 7-nm PZTFT using magnetic force microscopy.....	139
6.13 (a) The J vs. E plots for different thickness of PZTFT; (b) The $\ln J$ vs. $\ln E$ plots for space-charge-limited conduction (SCLC); Thickness dependence $I(d)$ for the leakage current in PZTFT. c) In the linear region (slope ~ 1 in (b)), the upper curve assumes d is the film thickness and yields $d^{-1.3}$, whereas the lower curve assumes ~ 7 nm accommodation length a and gives the expected space-charge-limited d^{-1} dependence. d) The quadratic region (slope ~ 2 in (b), the upper curve yields $d^{-3.8}$, whereas the lower curve assumes ~ 7 nm accommodation a and gives d^{-3} dependence.....	142

LIST OF ABBREVIATIONS

AFM	Atomic Force Microscopy
PFM	Piezoresponse Force Microscopy
MFM	Magnetic Force Microscopy
CV	Capacitance Voltage
E_c	Electric Coercive Field
ZFC	Zero Field Cooled
FCC	Field Cooled Cooling
FE	Ferroelectric
FM	Ferromagnetic
MF	Multiferroic
FTJ	Ferroelectric Tunnel Junction
MFTJ	Multiferroic Tunnel Junction
FeRAM	Ferroelectric Random Access Memory
MRAM	Magnetic Random Access Memory
E	Electric Field
H	Magnetic Field
H_c	Magnetic Coercive Field
M	Magnetization
T	Temperature
M_R	Remnant Magnetization

M_S	Spontaneous Magnetization
P	Polarization
P_R	Remnant Polarization
P_S	Spontaneous Polarization
PLD	Pulsed Laser Deposition
T_C	Curie Temperature
VSM	Vibrating Sample Magnetometer
ϵ	Dielectric Constant
PZT	$\text{PbZr}_{0.52}\text{Ti}_{0.48}\text{O}_3$
LSMO	$\text{La}_{0.67}\text{Sr}_{0.33}\text{MnO}_3$
LSAT	$(\text{LaAlO}_3)_{0.3}(\text{Sr}_2\text{AlTaO}_6)_{0.7}$
PZTFT	$\text{Pb}(\text{Zr}_{0.53}\text{Ti}_{0.47})_{0.60}(\text{Fe}_{0.5}\text{Ta}_{0.5})_{0.40}\text{O}_3$
XRD	X-Ray Diffraction
ϵ'	Real Dielectric Permittivity
ϵ''	Imaginary Dielectric Permittivity
PPMS	Physical Property Measurement System (PPMS)
J	Current Density
TER	Tunneling Electroresistance
TMR	Tunneling Magnetoresistance
XPS	X-Ray Photoelectron Spectroscopy

LIST PUBLICATIONS /PRESENTATIONS

PUBLICATIONS

1. N. Ortega, A. Kumar, J. F. Scott, Douglas B. Chrisey, M. Tomazawa, S. Kumari, **D. Barrionuevo Diestra**, and R. S. Katiyar. Relaxor-ferroelectric superlattices: A high energy density capacitor. *J. Phys.: Condens. Matter.* **24**, 445901 (2012).
2. S. Sahoo, G. Khurana, S. Barik, S. Dussan, **D. Barrionuevo**, R. S. Katiyar. In-situ Raman Studies of Electrically Reduced Graphene Oxide and Its Field Emission Properties. *J. Phys. Chem. C.* **117** (10), pp 5485-5491. (2013).
3. A. Charris-Hernández, R. Melgarejo, **D. Barrionuevo**, A. Kumar, and M. S. Tomar. Multiferroic properties of $\text{CoFe}_2\text{O}_4/\text{Bi}_{3.4}\text{La}_{0.6}\text{Ti}_3\text{O}_{12}$ bilayer structure at room temperature. *J. Appl. Phys.* **114**, 034108 (2013).
4. J. Beltran-Huarac, J. Carpena-Nunez, **D. Barrionuevo**, F. Mendoza, Ram S. Katiyar, L. F. Fonseca, B. R. Weiner, G. Morell. Synthesis and transport properties of $\text{La}_{0.67}\text{Sr}_{0.33}\text{MnO}_3$ conformally-coated on carbon nanotubes. *CARBON* **65**, 252-260 (2013).
5. **D. Barrionuevo**, N. Ortega, A. Kumar, R. Chatterjee, J. Scott, and R. S. Katiyar. Thickness Dependent Functional Properties of $\text{PbZr}_{0.52}\text{Ti}_{0.48}\text{O}_3/\text{La}_{0.67}\text{Sr}_{0.33}\text{MnO}_3$ Heterostructures. *J. Appl. Phys.* **114**, 234103 (2013).
6. M. S. Tomar, A. Charris-Hernández, **D. Barrionuevo** and A. Kumar. Structural and Multiferroic Properties of $\text{Bi}_{3.6}\text{La}_{0.6}\text{Ti}_3\text{O}_{12}/\text{CoFe}_2\text{O}_4$ Composite Thin Films. *Integrated Ferroelectrics* **157**, 63-70 (2014).
7. S. Kooriyattil, S. P. Pavunny, **D. Barrionuevo**, and R. S. Katiyar. Optical, ferroelectric, and piezoresponse force microscopy studies of pulsed laser deposited Aurivillius $\text{Bi}_5\text{FeTi}_3\text{O}_{15}$ thin films. *J. Appl. Phys.* **116**, 144101 (2014).
8. **D. Barrionuevo**, Le Zhang, N. Ortega, A. Sokolov, A. Kumar, Pankaj Misra, J. F. Scott, R. S. Katiyar. Tunneling Electroresistance in Multiferroic Heterostructures. *Nanotechnology.* **25**, 495203 (2014).
9. **D. Barrionuevo**, Le Zhang, N. Ortega, A. Sokolov, A. Kumar, Pankaj Misra, J. F. Scott, R. S. Katiyar. Tunneling Electroresistance in Multiferroic Heterostructures. *Nanotechweb.* (2014). <http://nanotechweb.org/cws/article/lab/59626>
10. R. K. Katiyar, Y. Sharma, **D. Barrionuevo**, S. Kooriyattil, S. P. Pavunny, J. S. Young, G. Morell, B. R. Weiner, R.S. Katiyar, and J. F. Scott. Ferroelectric photovoltaic

properties in doubly substituted $(\text{Bi}_{0.9}\text{La}_{0.1})(\text{Fe}_{0.97}\text{Ta}_{0.03})\text{O}_3$ thin films. *Appl. Phys. Lett.* **106**, 082903 (2015).

11. R. K. Katiyar, Y. Sharma, **D. Barrionuevo**, Pankaj Misra, S. Kooriyattil, S. P. Pavunny, G. Morell, B. R. Weiner, J. F. Scott, and R. S. Katiyar. Unipolar resistive switching in planar Pt/BiFeO₃/Pt structure. *AIP Advances* **5**, 037109 (2015).

12. N. Ortega, **D. Barrionuevo**, A. Kumar, J. F. Scott and R. S. Katiyar. Ferroelectric/Multiferroic Tunnel Junctions for Multifunctional Applications. *Wiley Encyclopedia of Electrical and Electronics Engineering*. 1-18 (2015).

13. Y. Sharma, Pankaj Misra, **D. Barrionuevo**, R. Chatterjee, R. S. Katiyar. Room Temperature Weak Multiferroism and Magnetodielectric Effect in Highly Oriented $(\text{Y}_{0.9}\text{Bi}_{0.1})(\text{Fe}_{0.5}\text{Cr}_{0.5})\text{O}_3$ Thin Films. *Materials Research Bulletin* **68**, 49-53 (2015).

14. Ashok Kumar, **D. Barrionuevo**, N Ortega, A. K. Skukla, Santirajan Shannigrahi, J. F. Scott and Ram S. Katiyar. Ferroelectric Capped Magnetization in Multiferroic PZT/LSMO Tunnel Junctions. *Appl. Phys. Lett.* **106**, 132901 (2015).

15. Y. Sharma, **D. Barrionuevo**, R. Agarwal, S. P. Pavunny, R. S. Katiyar. Ferroelectricity in Rare-Earth Modified Hafnia Thin Films Deposited by Sequential Pulsed Laser Deposition. *ECS Solid State Letters* **4** (11), N13-N16 (2015).

16. T. B. Limbu, F. Mendoza, **D. Barrionuevo**, J. Carpena, B. Maruyama, R. S. Katiyar, B. R. Weiner, and G. Morell. Study on the optical and electrical properties of tetracyanoethylene doped bilayer graphene stack for transparent conducting electrodes. *AIP Advances* **6**, 035319 (2016).

17. **D. Barrionuevo**, Le Zhang, N. Ortega, A. Sokolov, A. Kumar, J. F. Scott, R. S. Katiyar. Enhanced Tunneling electroresistance in Pt/PZT/LSMO Ferroelectric tunnel junctions in presence of magnetic field. (*Submitted*) (2016).

18. **D. Barrionuevo**, N. Ortega, D. Sanchez, A. Kumar, J. F. Scott, R. S. Katiyar. Thickness dependent multiferroic properties of nanoscale PZTFT: A 7-nm Multiferroic Tunnel Junction. (*Submitted*) (2016).

CONFERENCE PRESENTATIONS

1. **D. Barrionuevo**, N. Ortega, A. Kumar, and R. S. Katiyar. Structural and Ferroelectric Properties of Epitaxial Ultrathin $\text{PbZr}_{0.52}\text{Ti}_{0.48}\text{O}_3$ Films Prepared on $\text{La}_{0.67}\text{Sr}_{0.33}\text{MnO}_3/(\text{LaAlO}_3)_{0.3}(\text{Sr}_2\text{AlTaO}_6)_{0.7}$ Substrates. American Physical Society March Meeting, Boston, MA, February 27-March 2, 2012.
2. **D. Barrionuevo**, N. Ortega, A. Kumar, and R. S. Katiyar. Structural, Magnetic and Electric Properties of Epitaxial Ultrathin $\text{PbZr}_{0.52}\text{Ti}_{0.48}\text{O}_3$ Films Prepared on $\text{La}_{0.67}\text{Sr}_{0.33}\text{MnO}_3/(\text{LaAlO}_3)_{0.3}(\text{Sr}_2\text{AlTaO}_6)_{0.7}$ Substrates. Materials Science & Technology 2012. Pittsburgh, Oct. 7-11, 2012.
3. **D. Barrionuevo**, N. Ortega, A. Kumar, and R. S. Katiyar. Magnetic, Electrical and Ferroelectric Properties of High Oriented Ultrathin $\text{PbZr}_{0.52}\text{Ti}_{0.48}\text{O}_3/\text{La}_{0.67}\text{Sr}_{0.33}\text{MnO}_3$ Heterostructures for Tunnel Junction Applications. Materials Research Society Fall Meeting, Boston, MA, Nov. 25-30, 2012.
4. **D. Barrionuevo**, Le Zhang, N. Ortega, A. Sokolov, A. Kumar, and R. S. Katiyar. Dielectric, Magnetic and Ferroelectric Properties of High Oriented Ultrathin $\text{PbZr}_{0.52}\text{Ti}_{0.48}\text{O}_3/\text{La}_{0.67}\text{Sr}_{0.33}\text{MnO}_3$ Heterostructures for Ferroelectric Tunnel Junction Applications. Materials Research Society Fall Meeting, Boston, MA, Dec. 1-6, 2013.
5. **D. Barrionuevo**, Le Zhang, N. Ortega, A. Sokolov, and R. S. Katiyar. Studies of the Structural, Transport and Electrical Properties in Multiferroic Tunnel Junctions. 2014 IEEE ISAF/IWATMD/PFM Workshop, Penn State University in State College, Pennsylvania, May 12-16, 2014.
6. **D. Barrionuevo**, N. Ortega, D. Sanchez, and R. S. Katiyar. Studies of the Magnetic, Dielectric and Electrical Properties of PZTFT for Multiferroic Tunnel Junction Applications. 59th Annual Magnetic and Magnetic Materials (MMM) Conference. Honolulu, Hawaii, Nov. 3-7, 2014.
7. **D. Barrionuevo**, N. Ortega, D. Sanchez, and R. S. Katiyar. Studies of the Magnetic, Dielectric and Electrical Properties of PZTFT for Multiferroic Tunnel Junction Applications. Materials Research Society Fall Meeting, Boston, MA, Nov. 30-Dec. 5, 2014.
8. **D. Barrionuevo**, Le Zhang, N. Ortega, A. Sokolov, and R. S. Katiyar. Ferroelectric tunnel junction with PZT barrier and thickness effect in PZTFT for multiferroic tunnel junction applications. 2015 Workshop on the Fundamental Physics of Ferroelectrics and Related Materials, Knoxville, TN, January 25-28, 2015.

9. **D. Barrionuevo**, N. Ortega, A. Kumar, and R. S. Katiyar. Thickness Dependent Multiferroic Properties of Nanoscale PZT/LSMO and PZTFT for Multiferroic Tunnel Junction Applications. Materials Research Society Fall Meeting, Boston, MA, Nov. 29-Dec. 4, 2015.

10. **D. Barrionuevo**, N. Ortega, and R. S. Katiyar. Studies of Dielectric, Magnetic and Ferroelectric Properties of Novel Multiferroic Material PCZTFT at Room Temperature. Materials Research Society Fall Meeting, Boston, MA, Nov. 29-Dec. 4, 2015.

CHAPTER 1

INTRODUCTION

1.1. FERROELECTRIC MATERIALS

1.1.1 Ferroelectricity

A ferroelectric crystal shows a reversible spontaneous electric polarization and a hysteresis loop that can be observed in certain temperature regions, delimited by a transition point called the Curie temperature, T_C . At temperatures above T_C , the crystal is no longer ferroelectric and exhibits normal dielectric behavior [1-2].

Ferroelectric materials usually, but not always, exist in a nonpolar state at temperatures above Curie temperature (T_C), and have anomalously high dielectric constants, especially near T_C . Typical dielectric constant temperature and polarization temperature characteristics is shown in Figure 1.1. The dielectric constant increases very sharply to a very high peak value at T_C . The anomalously high value of ϵ_r in the neighborhood of T_C is generally referred to as the anomalous value. At $T > T_C$, anomalous behavior closely follows the Curie-Weiss law

$$\epsilon_r = \frac{C}{T - T_C} \quad (1)$$

where C is known as the Curie constant. In fact, anomalous behavior always appears near any transition point between two different phases, even at T below T_C . At the transition points, there are anomalies not only in the dielectric constant and polarization, but also in

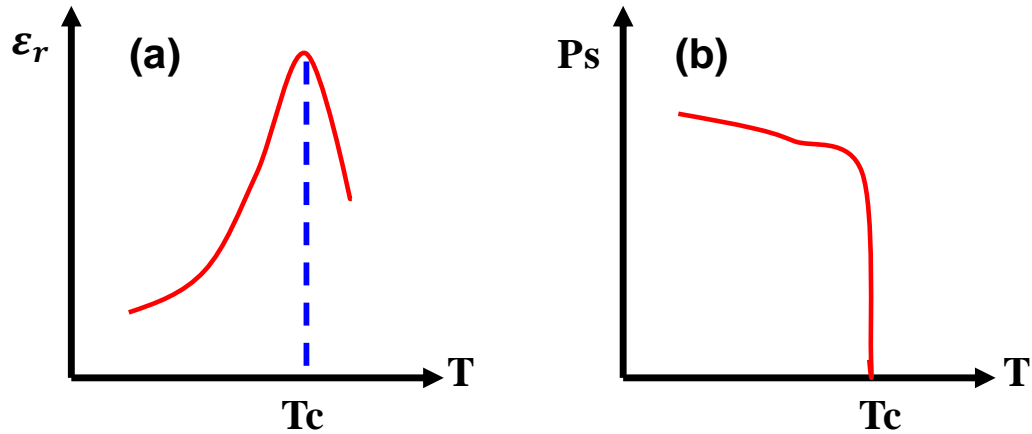


Figure 1.1. Schematic illustration of the variation of the (a) dielectric constant, ϵ_r , and the (b) spontaneous polarization, P_s , with temperature, for Barium titanate (BaTiO_3) with $T_c = 120^\circ\text{C}$ [1].

piezoelectric and elastic constants and specific heat, because of the change in crystal structure.

Ferroelectrics have reversible spontaneous polarization. The word spontaneous may mean that the polarization has a nonzero value in the absence of an applied electric field. The word reversible refers to the direction of the spontaneous polarization that can be reversed by a field applied in opposite direction. The spontaneous polarization, P_s , usually increases sharply, as the temperature is lowered across the transition point and then gradually reaches a saturation value at lower temperatures. The most prominent features of ferroelectric properties are hysteresis and nonlinearity in the relation between polarization P and an applied electric field E . A typical hysteresis loop is shown schematically in Figure 1.2. When the field is small, the polarization increases linearly with the field. This is mainly due to field-induced polarization; because the field is not large enough to cause orientation of the domains (path AB). At high fields, polarization

will reach a state of saturation corresponding to point B, in which most domains are aligned toward the direction of the poling field. Now, if the field is gradually

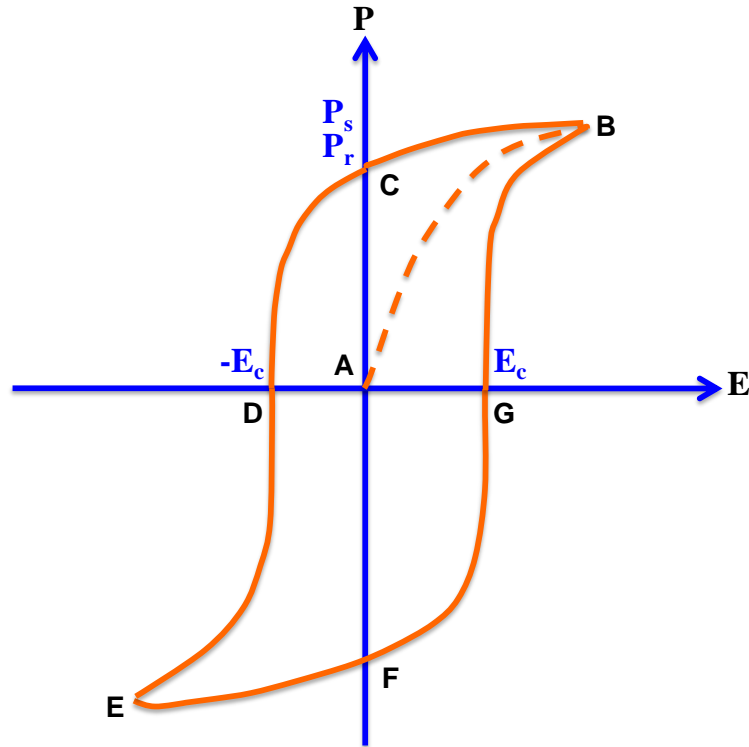


Figure 1.2. Schematic diagram of a typical ferroelectric hysteresis loop [2].

decreased to zero, the polarization will decrease, following the path BC. The point C represents the remnant polarization P_r .

The field required to bring the polarization to zero is called the coercive field E_c (portion AD on zero polarization axis). E_c depends not only on temperature, but also on the measuring frequency and the waveform of the applied field. When the field in the opposite direction decreases to zero, the polarization is left reversed, indicating that domains were formed during poling and that the motion of the domain walls results in the change of direction of polarization [3-4].

1.1.2 Piezoelectricity

All ferroelectrics exhibit the piezoelectric effect (although all piezoelectrics are not necessarily ferroelectric). The piezoelectric effect is a phenomenon whereby mechanical stress or strain leads to reorientation of electric dipoles through a material, inducing a spontaneous change in the charge polarization. This effect may be formally described by the following set of equations, which provide a relationship between the electric displacement D , the electric field E , and the stress and strain, T and S respectively [5]:

$$D = \epsilon_T E + d_{33} T \quad (2)$$

$$S = d_{33} E + s_E T \quad (3)$$

where ϵ_T is the dielectric constant and d_{33} is the piezoelectric constant, s_E is the material's compliance (elastic modulus) in the presence of a constant electric field. This constant describes the stress strain relationship for a material and is based on the material's Young's modulus and Poisson's ratio [6]. From the equations above, it can be seen that any increase or decrease in stress (T) or strain (S) on the material will lead to an increase or decrease in electric displacement (D) and in the material's electric field (E). These relations also predict the existence of the converse piezoelectric effect, whereby a piezoelectric material physically changes shape when an external electric field E is introduced. This altered shape is a result of an increase in stress T and strain S on the material due to the electric field change. The piezoelectric effect is used in a variety of applications because the crystal motion resulting from the electric field is both predictable and precise. Common piezoelectrics include lead zirconate titanate (PZT) and bismuth ferrite [7]. The piezoelectric effect can only be observed for those below the

ferroelectric Curie temperature since above this temperature, the net electric polarization is zero.

1.1.3 Lead Zirconate Titanate $\text{Pb}(\text{Zr,Ti})\text{O}_3$ (PZT) - Perovskite

Many ferroelectrics have the chemical formulas of an ABO_3 type, with a perovskite structure. One representative ferroelectric material having a perovskite structure is lead zirconate titanate ($\text{Pb}(\text{Zr,Ti})\text{O}_3$ -PZT) which is a solid solution of lead zirconate (PZ) and lead titanate (PT). In the perovskite structure, *A* atoms (Pb), with large cations are located at the corner of the unit cell, oxygen at the face center positions and an octahedron constructed by six oxygen atoms including a smaller metallic element *B* (Zr and Ti) at the center of the perovskite unit cell, which are the active ions in promoting ferroelectricity (Figure 1.3).

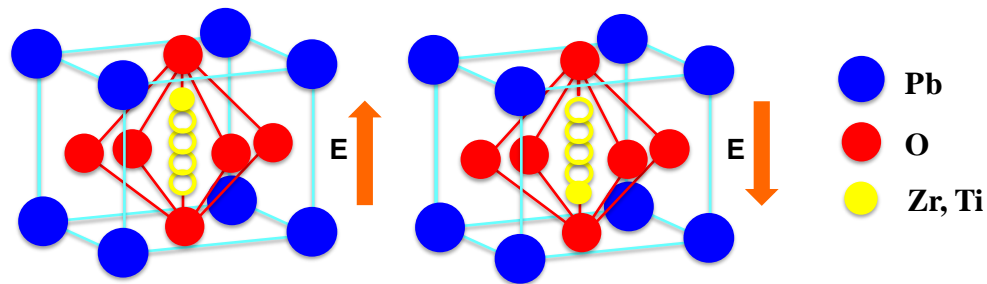


Figure 1.3. The cubic perovskite structure. Displacement of Zr-Ti ions with the application of positive and negative electric fields.

The bonding in an ideal cubic perovskite is ionic and the short range repulsions between the adjacent closed ions shell (electrons clouds) are minimized for symmetric structures. The existence or absence of ferroelectricity depends on the balance between these short range repulsions, which are favored by the non-centrosymmetric structures, and

additional bonding considerations which act to stabilize the distortions necessary for the ferroelectric phase.

In the tetragonal crystal system, the perovskite structure has one axis of the lattice (001) extended, while the other two axes are shortened. Along the extended axis, the displacement of positive ions (A and B), negative anions and their valence electrons, separate the center of gravity of the positive and negative electric charges, which allow the occurrence of an electric polarization moment [8, 9].

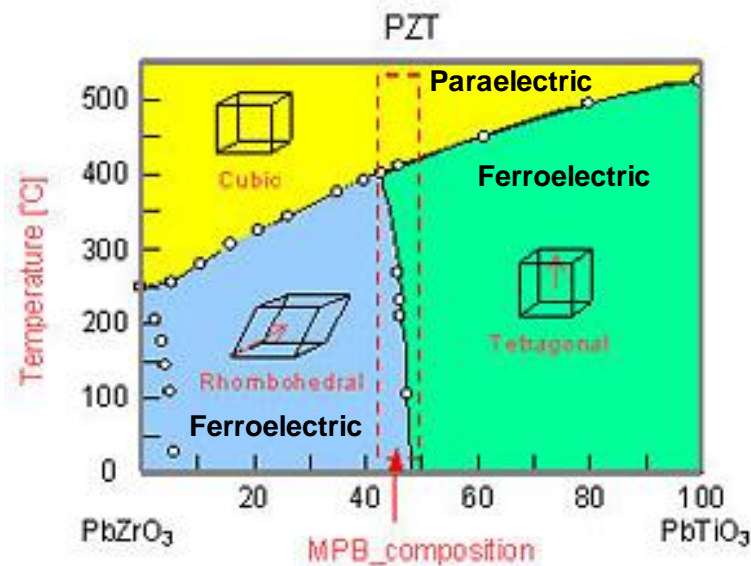


Figure 1.4. Different composition corresponds to different crystallite structures. Note the morphotropic phase boundary (MPB), at a composition of 52% lead zirconate to 48% lead titanate [9].

The phase diagram of PZT is shown in Figure 1.4, substitution of Ti by Zr in PT reduces the tetragonal distortion and above the Zr/Ti ratio of 0.52/0.48, the rhombohedral ferroelectric phase is formed. The boundary between tetragonal and rhombohedral phases is independent of temperature and is referred to as the morphotropic phase boundary

(MPB). At the MPB, the lead zirconate titanate $\text{Pb}(\text{Zr}_{0.52}\text{Ti}_{0.48})\text{O}_3$ perovskite has lattice parameters $a = b = 4.03 \text{ \AA}$ and $c = 4.14 \text{ \AA}$, with an extremely large dielectric constant, a marked piezoelectric effect and a ferroelectric nature. Another significant observation is that most of the perovskite ferroelectrics contain d^0 (B cation such as Ti^{+4} , Zr^{+4} , Nb^{+5} are formally in a d^0 state) [10].

There has been great interest in understanding of the fundamental physics of ferroelectrics over the last 50 years, which, in turn, has contributed to the optimization of materials for specific device applications. Today, ferroelectrics are used to make high energy density capacitors, transducers and actuators, because of their piezoelectric and ferroelectric random access memory-FeRAM exploiting their ferroelectric hysteresis properties, resulting in two stable states of opposite polarization [11].

1.2. FERROMAGNETIC MATERIALS

1.2.1 Ferromagnetic effect

Ferromagnetic materials are magnetic materials. General ferromagnetic properties are summarized as follows: (1) The magnetization is spontaneous, (2) The magnetization may reach a saturation value by a weak magnetizing field, (3) The material may have zero magnetization at zero (or very small) magnetic fields, and the magnetization remains after the removal of the magnetic field, and (4) The ferromagnetic behavior (i.e., the spontaneous magnetization) completely disappears at temperatures higher than a critical temperature, called the Curie temperature T_C . At $T > T_C$, spontaneous magnetization is destroyed, and the material becomes paramagnetic, not ferromagnetic.

The exchange energy principle, coupled with the Pauli's exclusion principle, shows that the potential energy of the electrons in the magnetized state is lower than when they are

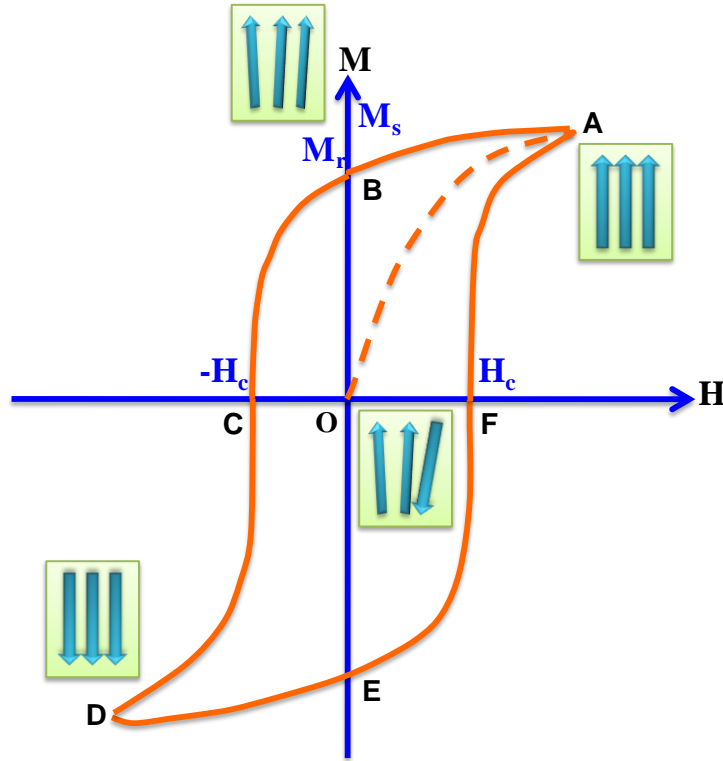


Figure 1.5. (a) The M-H hysteresis loop of a typical ferromagnetic material [14].

in the nonmagnetized state [12-14]. This conclusion can also be realized on the basis of band theory, by considering that the spin-up electrons form one band and those that are spin-down, form another. Also, we would expect that there is a critical temperature, at or above which, the magnetized state would become an unmagnetized state and spontaneous magnetization would be completely destroyed. This critical temperature is called the Curie temperature T_C . Its value is different for different magnetic materials.

The influence of an applied magnetic field on the orientation of the magnetic moments in the domains toward the direction of the magnetic field (H) to produce an overall magnetization of the whole material. Suppose that we apply a magnetic field H to a non-magnetized ferromagnetic solid, starting with zero field and gradually increasing the field

in steps (Figure 1.5). The magnetization (M) increases with increasing H (portion OA), corresponding to rotation of domains from the original “easy” crystal direction to another “easy” direction more parallel to H . In point “A” the magnetic moments of all domains parallel to H , implying that the magnetization has reached a saturation value.

Now we start to reduce the magnetic field H , also in steps. As can be seen in Figure 1.5, with further decrease of H to zero (portion AB), M does not go back to zero, but decreases following a different curve and reaches a finite value M_R at $H = 0$. M_R is referred to as the remnant magnetization. To bring M to zero (BC), we need a reverse magnetic field $-H_C$, which is generally referred to as the coercive field. This is the size of magnetic field, opposite in direction to the magnetization field, required to bring the magnetization to the vanishing point. The formation of a hysteresis loop implies that the magnetization of a ferromagnetic material is irreversible.

The most well-known material that exhibits magnetic properties is the ferromagnet. For a ferromagnet, all magnetic dipoles in a domain are in parallel alignment. Even if all magnetic dipoles are not aligned, however, a net magnetic moment may still be observed. Such is the case with a ferrimagnet, a material in which the sum of the magnetic dipole moments in one direction is stronger than the net magnetic moment in the antiparallel direction.

1.2.2 Lanthanum strontium manganite (La, Sr)MnO₃ (LSMO) - Perovskite

Lanthanum strontium manganite is an oxide with perovskite structure. The chemical composition of LSMO is $\text{La}_{1-x}\text{Sr}_x\text{MnO}_3$, where x is a variable indicating the doping level. The unit cell of LSMO is given in Figure 1.6. The manganese atoms are

surrounded by an octahedron of oxygen atoms. The oxygen atoms are ionized to O^{2-} , lanthanum to La^{3+} , and strontium to Sr^{2+} . The manganese atoms are either ionized to Mn^{3+} or to Mn^{4+} depending on the doping level. This results in the 3d shell of the manganese atoms being filled with either 4 or 3 electrons. The electrical and magnetic behavior is largely determined by the electrons in the 3d shell of the manganese atoms [15].

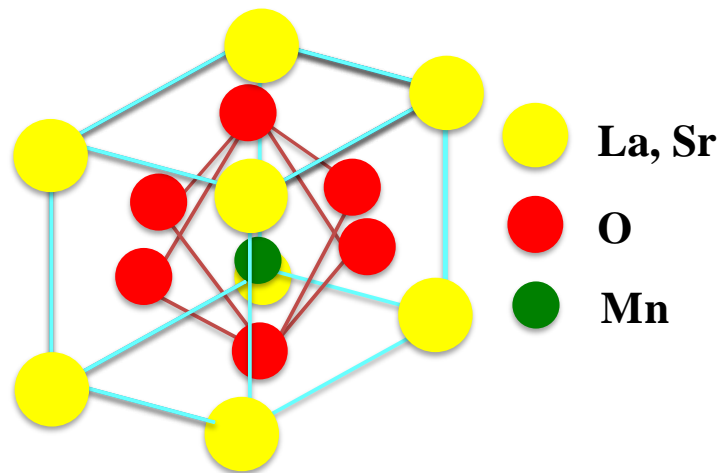


Figure 1.6. Unit cell of LSMO. The manganese atom(green) is surrounded by an oxygen octahedron(red). The atoms at the yellow sites can be either lanthanum or strontium [15].

Phase diagrams of the mixed valence perovskite manganites are rich in different magnetic, resistive and structural phases. Even though the phase diagram of each composition is different there are some features that are common. A sketch of the phase diagram of the perhaps most well studied manganite $La_{1-x}Sr_xMnO_3$ is depicted in Figure 1.7. A typical manganite phase diagram looks like this: The compositions at either end of the x-range, are insulators at all temperatures and antiferromagnets at low temperatures [16]. With a small amount of doping ($x \geq 5\%$) the ferromagnetic phase can be obtained. Further doping ($x \geq 15 - 30\%$) results in a metallic phase and an increase in the magnetic

transition temperature. Then close to $x = 0.5$, where the Mn^{4+} to Mn^{3+} ratio is about 1:1, a charge-ordered (antiferromagnetic) insulating phase starts to evolve at low temperatures. In the $\text{La}_{1-x}\text{Sr}_x\text{MnO}_3$ compound a structural transition from orthorhombic ($x \geq 20\%$) to rhombohedral ($x \leq 20\%$) as described in Figure 1.7 is present. The structural transition is modified not only by composition but also with temperature. In general, the orthorhombic phase is stable at lower temperatures, while the rhombohedral phase requires higher temperatures.

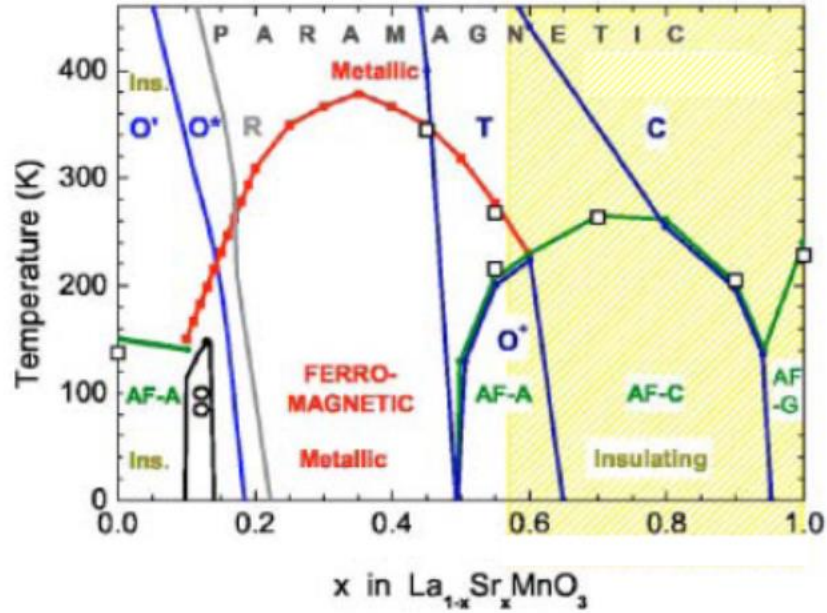


Figure 1.7. $\text{La}_{1-x}\text{Sr}_x\text{MnO}_3$ phase diagram system for $0 \leq x \leq 1$. C, T, R, O*, O', and O⁺ denote, respectively, the cubic $Pm\bar{3}m$, tetragonal $I4/mcm$, rhombohedral $R\bar{3}c$, two orthorhombic $Pbmn$, and orthorhombic $Fmmm$ structural phases. AF-A, AF-C, and AF-G stand for the antiferromagnetic phases of the A, C, and G type, respectively OO denotes the region of stability of the orbital and charge ordered, insulating, ferromagnetic phase. “Ins.” stands for “insulating” [16].

LSMO is one of the perovskite manganites that show the colossal magnetoresistance (CMR) effect and is also observed to be a half-metal for compositions around $x=0.33$. For this reason, we chose this composition.

1.3. MULTIFERROIC MATERIALS

1.3.1 Multiferroics

A multiferroic is a material in which two or all three of the properties of ferroelectricity, ferromagnetism and ferroelasticity occur in the same phase [17, 18]. The overlap required of ferroic materials that allows them to be classified as multiferroic, is shown schematically in Figure 1.8 (a). Only small subgroups of all magnetically and electrically polarizable materials are either ferromagnetic or ferroelectric and fewer still simultaneously exhibit both order parameters. In these select materials, however, there is the possibility that electric fields cannot only reorient the polarization but also control magnetization; similarly, a magnetic field can change electric polarization. This functionality offers an extra degree of freedom and hence we refer to such materials as magnetoelectrics (Figure 1.8 (b)). Magnetoelectricity is an independent phenomenon that can arise in any material with both magnetic and electronic polarizability, regardless of whether it is multiferroic or not. By definition, a magnetoelectric multiferroic must be simultaneously both ferromagnetic and ferroelectric [19]. It should be noted, however, that the current trend is to extend the definition of multiferroics to include materials possessing two or more of any of the ferroic or corresponding antiferroic properties such as antiferroelectricity and antiferromagnetism. The scarcity of magnetoelectric multiferroics can be understood by investigating a number of factors including symmetry, electronic properties, and chemistry. We note that there are only 13 point groups that can give rise to multiferroic behavior. Additionally, ferroelectrics by definition are insulators (and in 3d transition metal based oxides, typically possess ions that have a formal d^0 electronic state), while itinerant ferromagnets need conduction electrons; even in double

exchange ferromagnets such as the manganites, magnetism is mediated by incompletely filled 3d shells. Thus there exists a seeming contradiction between the conventional mechanism of off-centering in a ferroelectric and the formation of magnetic order which explains the scarcity of ferromagnetic-ferroelectric multiferroics [20]. The focus of many researchers, in turn, has been in designing and identifying new mechanisms that lead to magnetoelectric coupling and multiferroic behavior. It has been proposed that one can engineer multiferroic properties by chemically controlling the functionality on a site by site basis. Many researchers have focused on model systems, such as the perovskites with chemical formula ABO_3 , as a pathway for the creation of multiferroic behavior. Single phase multiferroism has been identified in only a few perovskite oxides and is typically achieved by making use of the stereochemical activity of the lone pair on large (A site) cations to provide ferroelectricity while retaining magnetism on the smaller (B site) cations.

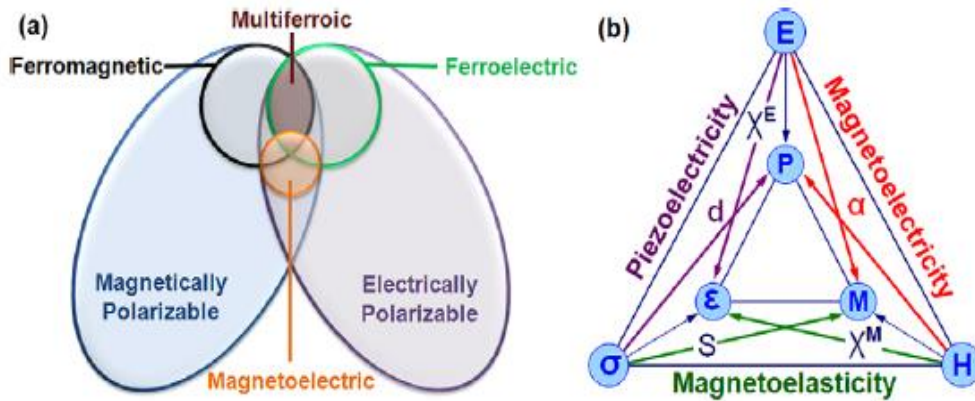


Figure 1.8. (a) Relationship between multiferroic and magnetoelectric materials. Illustrates the requirements to achieve both in a material. (b) Schematic illustrating different types of coupling present in materials. Much attention has been given to materials where electric and magnetic order is coupled. These materials are known as magnetoelectric materials [19].

1.3.2 Magnetoelectric coupling

The magnetoelectric effect in a single-phase crystal is traditionally described [21, 22] in Landau theory by writing the free energy F of the system in terms of an applied magnetic field H whose i th component is denoted H_i , and an applied electric field E whose i th component is denoted E_i . Note that this convention is unambiguous in free space, but that E_i within a material encodes the resultant field that a test particle would experience. Let us consider a non-ferroic material, where both the temperature-dependent electrical polarization $P_i(T)$ (μCcm^{-2}) and the magnetization $M_i(T)$ (μ_B per formula unit, where μ_B is the Bohr magneton) are zero in the absence of applied fields and there is no hysteresis. It may be represented as an infinite, homogeneous and stress-free medium by writing F under the Einstein summation convention in S.I. units as:

$$-F(\vec{E}, \vec{H}) = \frac{1}{2} \epsilon_0 \epsilon_{ij} E_i E_j + \frac{1}{2} \mu_0 \mu_{ij} H_i H_j + \alpha_{ij} E_i H_j + \frac{\beta_{ijk}}{2} E_i H_j H_k + \frac{\gamma_{ijk}}{2} H_i E_j E_k + \dots \quad (4)$$

The first term on the right hand side describes the contribution resulting from the electrical response to an electric field, where the permittivity of free space is denoted ϵ_0 , and the relative permittivity $\epsilon_{ij}(T)$ is a second-rank tensor that is typically independent of E_i in non-ferroic materials. The second term is the magnetic equivalent of the first term, where $\mu_{ij}(T)$ is the relative permeability and μ_0 is the permeability of free space. The third term describes linear magnetoelectric coupling via $\alpha_{ij}(T)$; the third-rank tensors $\beta_{ijk}(T)$ and $\gamma_{ijk}(T)$ represent higher-order (quadratic) magnetoelectric coefficients. In the present scheme, all magnetoelectric coefficients incorporate the field independent material response functions $\epsilon_{ij}(T)$ and $\mu_{ij}(T)$. The magnetoelectric effects can then easily be established in the form $P_i(H_j)$ or $M_i(E_j)$. The former is obtained by differentiating F with respect to E_i , and then setting $E_i=0$. One obtains the polarization:

$$P_i(\vec{E}, \vec{H}) = -\frac{\partial F}{\partial E_i} = \epsilon_0 \epsilon_{ij} E_j + \alpha_{ij} H_j + \frac{\beta_{ijk}}{2} H_j H_k + \gamma_{ijk} H_j E_k + \dots \quad (5)$$

$$P_i(\vec{H}) = \alpha_{ij} H_j + \frac{\beta_{ijk}}{2} H_j H_k + \dots \quad (6)$$

The former is obtained by differentiating F with respect to H_i , and then setting $H_i=0$. One obtains the magnetization:

$$M_i(\vec{E}, \vec{H}) = -\frac{\partial F}{\partial H_i} = \mu_0 \mu_{ij} H_j + \alpha_{ij} E_j + \beta_{ijk} E_j H_k + \frac{1}{2} \gamma_{ijk} E_j E_k + \dots \quad (7)$$

$$M_i(\vec{E}) = \alpha_{ji} E_j + \frac{\gamma_{ijk}}{2} E_j E_k + \dots \quad (8)$$

In ferroic materials, the above analysis is less rigorous because $\epsilon_{ij}(T)$ and $\mu_{ij}(T)$ display field hysteresis. Moreover, ferroics are better parameterized in terms of resultant rather than applied fields [23]. This is because it is then possible to account for the potentially significant depolarizing/demagnetizing factors in finite media, and also because the coupling constants would then be functions of temperature alone, as in standard Landau theory. In practice, resultant electric and magnetic fields may sometimes be approximated [24] by the polarization and magnetization respectively.

A multiferroic that is ferromagnetic and ferroelectric is liable to display large linear magnetoelectric effects. This follows because ferroelectric and ferromagnetic materials often (but not always) possess a large permittivity and permeability, respectively, and $\alpha_{ij}(T)$ is bounded by the geometric mean of the diagonalized tensors $\epsilon_{ii}(T)$ and $\mu_{jj}(T)$ such that [59]:

$$\alpha_{ij}^2 \leq \epsilon_0 \mu_0 \epsilon_{ii} \mu_{jj} \quad (9)$$

Equation (9) is obtained from equation (4) by forcing the sum of the first three terms to be greater than zero, that is, ignoring higher-order coupling terms. It represents a stability condition in $\epsilon_{ij}(T)$ and $\mu_{ij}(T)$, but if the coupling becomes so strong that it drives a phase

transition to a more stable state, then $\alpha_{ij}(T)$, $\epsilon_{ij}(T)$ and $\mu_{ij}(T)$ take on new values in the new phase. Note that a large $\epsilon_{ij}(T)$ is not a prerequisite for a material to be ferroelectric (or vice versa); and similarly ferromagnets do not necessarily possess large $\mu_{ij}(T)$. Therefore, large magnetoelectric couplings need not arise in, or be restricted to, multiferroic materials.

1.3.3 Lead Iron Tantalate-Lead Zirconate Titanate $\text{Pb}(\text{Fe,Ta})\text{O}_3\text{-Pb}(\text{Zr,Ti})\text{O}_3$ (PZTFT) - Perovskite

$\text{Pb}(\text{Zr}_{0.53}\text{Ti}_{0.47})_{0.60}(\text{Fe}_{0.5}\text{Ta}_{0.5})_{0.40}\text{O}_3$ (PZTFT) [25-31] is a single-phase magnetoelectric multiferroic material that has the ability to control magnetization with an electric field and polarization with a magnetic field, at room temperature, making this material potentially important for the next generation of multiferroic spintronic devices. This material was discovered in our laboratory. The single-crystal slices (Figure 1.9), using transmission electron microscopy (TEM) techniques, showed that even within a single-crystal lamella the microstructure is extremely rich. Domains with curved domain walls, are present both as individual units and grouped into bundles, such that structure occurs across a number of different length scales. When selected area diffraction patterns were taken across different regions, they were extremely similar (Figure 1.9), strongly suggesting that domain variants had formed from a single higher symmetry parent state.

In Figure 1.10 (a) (i) show the lateral piezoresponse force microscopy (LPFM) phase information from a region of a different PZTFT single-crystal lamellae, after a magnetic field of 3 kOe has been applied perpendicular to the imaged surface and then removed

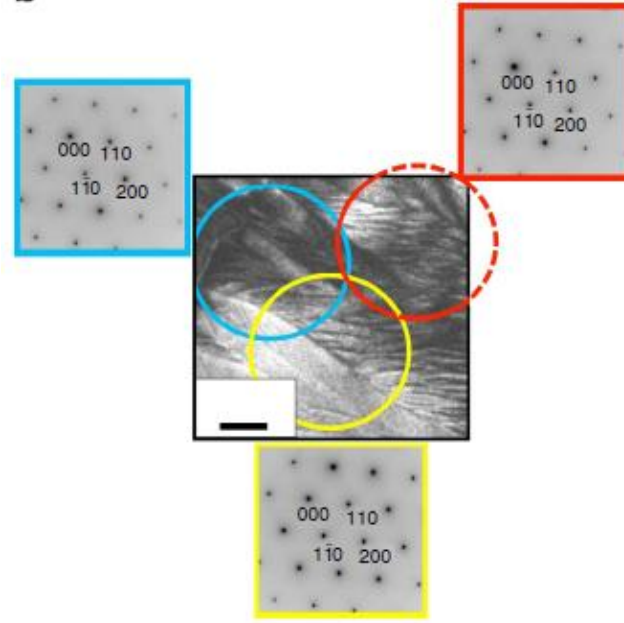


Figure 1.9. Complex domain structures in PZTFT single crystal. Transmission electron microscopy (TEM) reveals the single crystal structure of the material. It seems that all the domain variants have formed from a single higher symmetry parent state, as the selected area diffraction patterns from different regions, indicated by the coloured circles in (b), are indistinguishable. Scale bar, 200 nm [27].

before imaging. Different domains, with in-phase and anti-phase responses, are represented by the blue and red colours. The direction of the magnetic field was subsequently reversed and distinct changes in the phase image, Figure 1.10 (a) (ii), resulted: ferroelectric domains with orientations yielding the red phase contracted, while those mapped by the blue phase expanded. When the magnetic field was again applied in the original direction, changes in the domain distribution were partially reversed: Figure 1.10 (a) (iii). Figure 1.10 (b) summarizes the extent to which magnetically-induced ferroelectric domain changes could be reversed by changing the orientation of the applied magnetic field.

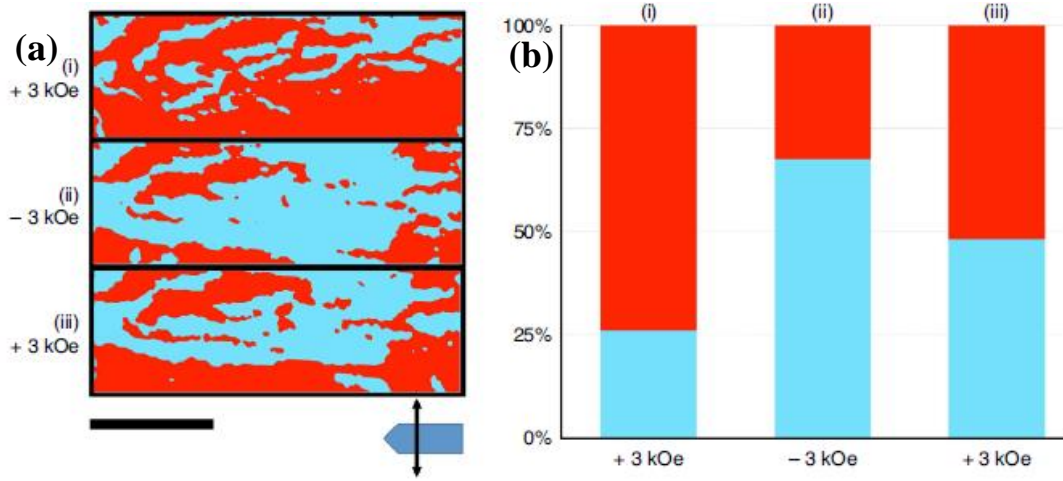


Figure 1.10. Modest magnetic fields induce partially reversible changes in ferroelectric domains. Phase images from lateral piezoresponse force microscopy (LPFM) change depending on the orientation of the magnetic field applied to the PZTFT lamella. Both the images in (a) and the area histograms of different phase colours (b) illustrate that 3 kOe applied in a nominally positive direction, perpendicular to the lamellar surface, favours the growth of polarization directions indicated in red. When applied in a nominally negative direction, these regions contract. Scale bar, 2 mm [27].

1.4. FERROELECTRIC AND MULTIFERROIC TUNNEL JUNCTION

One of the most important considerations in fabricating ferroelectric tunnel junctions (FTJ) is that the tunnel thickness must be greater than the minimum coherence length for stable ferroelectric polarization. For many years, it was thought that this would not work. Until the work of Gregg's group [32], most in the ferroelectrics community believed that ferroelectricity disappeared due to depolarization fields for films much thinner than 100 nm. Since the tunneling of electrons in oxide films thicker than 6 nm is negligible, this appeared to imply that ferroelectric tunnel junctions were impossible. However, we now know that the minimum thickness for stable ferroelectricity in a ferroelectric oxide [33] is ~ 1 nm, hence giving rise to the possibility of fabricating FTJ's.

The idea, based on the tunnel junction concept, in which a ferroelectric (polar) is employed as the barrier material is fairly new. This device, called ferroelectric tunnel junction (FTJ) can be used to interplay ferroelectricity and electron tunneling. The basic idea of a FTJ device was formulated in 1971 by Esaki et al. [34] which they called a polar switch at that time, an ultrathin FE tunneling barrier placed between two metallic electrodes [35]. FTJ may exhibit a tunneling electroresistance (TER) effect associated with the polarization switching of the ferroelectric barrier layer, leading to a change in resistance of the junction [36, 37]. The realization of this idea is a task with many obstacles, because it requires the fabrication of ultrathin films retaining pronounced ferroelectric properties at a thickness of only a few unit cells. However, the tremendous achievement in the field of complex oxide epitaxy [38, 39] and ferroelectric polymer [40] ultrathin films and also the advance in the nanoscale characterization techniques during the last few years, along with the theoretical studies, has made the fabrication and characterization of FTJs possible.

Another important consideration to recognize in any discussion of FE junctions, contrary to the discussions in most textbooks, is that ferroelectrics are generally NOT insulators. For many years, transport in FEs was dismissed as unimportant, because they were regarded as insulating crystals. However, the most widely used and studied FEs are perovskite oxides, and the bandgaps of BaTiO_3 and SrTiO_3 lie between 3.2 and 3.6 eV, with that of PbTiO_3 slightly less at ca. 2.9 eV. By comparison, the bandgap of III-Vs such as GaN or II-VIs such as ZnO are both approximately 3.4 eV. Even $\text{SrBi}_2\text{Ta}_2\text{O}_9$ has a band gap of only 4.0 eV; while BiFeO_3 has one of 2.74 eV. Thus oxides FEs are simply wide-gap semiconductors. This was relatively unimportant for bulk materials of a few

mm or more in thickness, but for very thin films it dominates electrical behavior. Hence we need to know everything about their band structure such as we do for Ge, Si, InSb or GaAs, if we are to design optimum devices. These materials are rather complicated, typically with *d*-like conduction bands exhibiting both light and heavy electrons (analogous to the light and heavy holes in the p-like valence bands of p-type II-VIs such as CdS). The effective masses are large, with typical free electron masses of $m^* = 5.5 - 6.5$.

It is well known that FE thin films are being used for technological applications in electronic devices, such as ferroelectric memories and microelectronic sensors and actuators. The existence of ferroelectricity persisting in ultrathin films (~ 1 nm), opens the possibility to further miniaturize devices based on FE materials. On the other hand, multiferroics can bring many more unique opportunities to exploit several functionalities in a single material or artificial nano-heterostructures. Heterostructures that combine ferroelectric with other functional materials can exhibit unusual physical properties. A way to exploit the ferroelectric properties of ultrathin films and multifunctional character of multiferroic materials, is to design tunnel junctions integrating ferroelectric or multiferroic films as the tunnel barrier or making the tunnel junction itself, a multiferroic heterostructures. At present, tunnel junctions using insulator (non-polar) barriers are the basis of MRAMs (magnetic random access memories). The ferroelectric and multiferroic heterostructures mentioned above may take advantage of tunnel magnetoresistance (TMR) and tunnel electroresistance (TER) effects.

A typical tunnel junction consists of two metal layers separated by a thin insulator layer (tunnel barrier). However, the tunneling probability becomes significant only for ultrathin

(< 10 nm thin) barriers. The tunnelling effect played a significant role during the development of quantum mechanics, as was first discussed in this context by Frenkel in 1930, because it provided a proof for the wave-particle dualism [41]. At present, various types of tunnel junctions have been studied fundamentally and used in microelectronic industry. In 1970, spin-dependent electron tunneling from FM metal electrodes across an amorphous Al_2O_3 film was observed by Tedrow and Meservey [42]. Michael Julliere, in 1975, proposed and demonstrated a magnetic tunnel junction using iron as the ferromagnet and germanium as the insulator. When the current flows between the two ferromagnets separated by an ultrathin insulator, the total resistance of the device, in which tunneling is responsible for current flowing, changes with the relative orientation of the two magnetic layers. The resistance is normally higher in the anti-parallel case [43]. This effect is called the tunnel (or junction) magnetoresistance effect (TMR), however, this experiment was carried out at an extremely low temperature (4.2 K), so it did not attract much attention for practical applications. The room temperature TMR was discovered in 1995 first by Miyazaki et al. [44] and independently by Moodera [45]. In 2001, Butler [46] and Mathon [47] independently made theoretical predictions that using iron as the ferromagnet and MgO as the insulator, the tunnel magnetoresistance can reach several thousand percent. In 2004, Parkin [48] and Yuasa [49] were able to make Fe/MgO/Fe junctions that reach over 200% TMR at room temperature. It is now the basis for the magnetic random access memory (MRAM) and the read sensor in hard disk drives. Despite the diversity of materials used in tunnel junctions, the common feature of almost all existing tunnel junctions is that they are based on non-polar barrier dielectrics.

Theoretical and experimental studies have demonstrated the existence of TMR (the magnetization aligned/disaligned in the metallic electrodes) and TER (dependence with the polarization state of the barrier) properties in TJs, using a polar barrier (i.e. ferroelectric/multiferroic tunnel junctions (FTJ/MFTJ)). These systems can produce a four-resistance state system [50], which is a novel tunnel junction with potential applications in future technology.

1.4.1 Theory of ferroelectric and multiferroic tunnel junctions

The concept of the FTJ is illustrated in Figure 1.11 (left side), which shows a simplified band diagram of the metal-ferroelectric-metal (MFM) heterostructures [56]. Due to the reversible electric polarization, the current-voltage characteristics of FTJs are

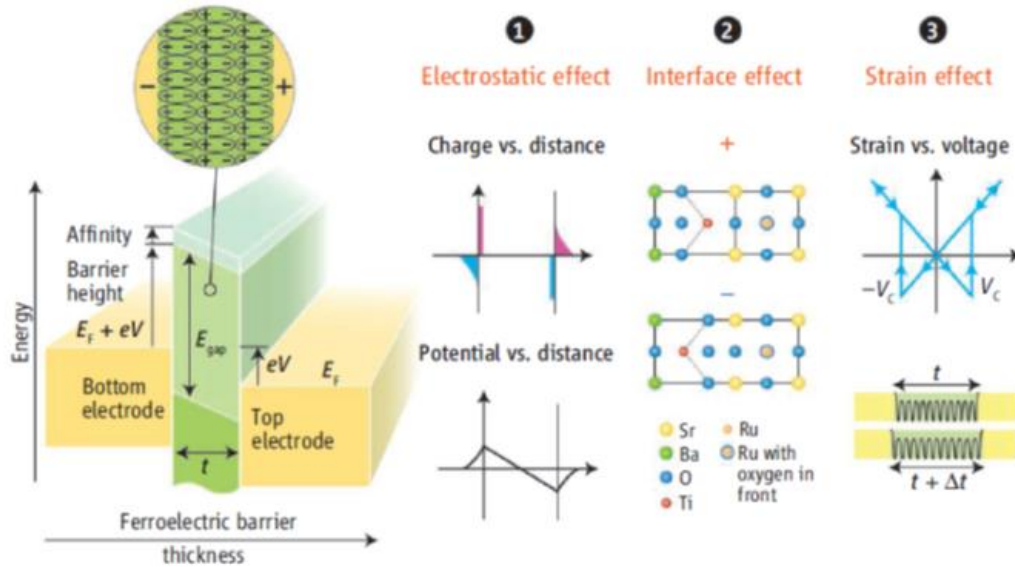


Figure 1.11. Schematics of a ferroelectric tunnel junction consisting of two electrodes separated by a nm-thick ferroelectric barrier layer. The ferroelectric nature of the barrier changes the transmission probability in three ways (#1, #2, #3) [56].

expected to be different from those of convention metal-insulator-metal junction. The electric polarization (P) in the FE barrier, which can be switched by an applied electric field, may have a pronounced effect on the conductance of a FTJ [51]. The reversal of polarization from $+P$ to $-P$ in the FE alters the switching of polarization charges at the barrier/electrode interfaces, changing the position of the ions in the FE unit cell and modifying the lattice strain inside the barrier.

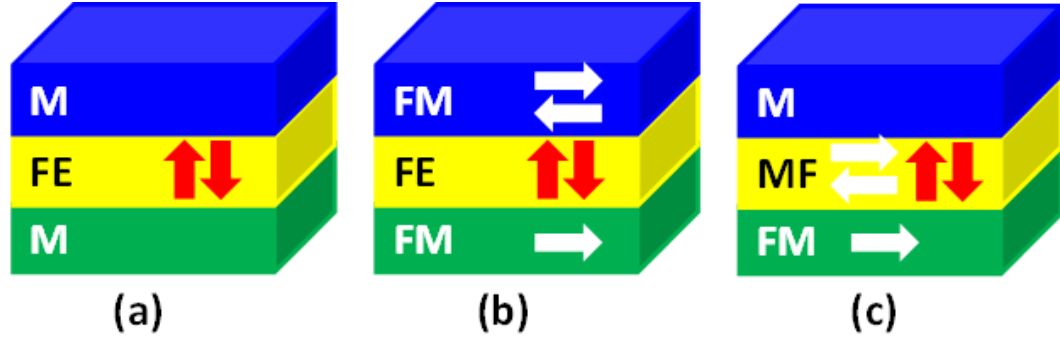
Figure 1.11 [(1), (2), and (3)] summarizes how the ferroelectric nature of the barrier changes the transmission probability in three ways: **(1)** The incomplete screening of the FE bound charge leads to an electrostatic potential that superimposes the contact potential in the tunnel junction; **(2)** The displacement of the B-site atom affects the atomic orbital hybridizations at the interface which makes the transmission probability different for the two opposite polarization orientations (here we consider a BaTiO₃/SrRuO₃ interface, as an example) and **(3)** Due to the piezoelectricity of a FE barrier, an applied voltage produces a strain which changes the transport characteristics of the barrier, such as the barrier width and attenuation constant.

Theoretical and experimental work indicates that the TER in MFM junctions with ultrathin barriers depends on the orientation of the electric polarization which can be switched by an applied electric field. Velez et al. [52], on the basis of first principle calculations, have shown that the polarization of a BaTiO₃ barrier leads to a substantial drop in the tunneling conductance due to changes in the electronic structure driven by ferroelectric displacement. FTJs have attracted interest both for the basic physics which is involved in controlling their properties and for their potential applications in nanoelectronics and data storage [53-56].

In the last few years a significant number of experimental work on FTJs has been carried out based on inorganic polar barriers, where TER effects have been observed: i.e. $\text{Pb}(\text{Zr,Ti})\text{O}_3$ [57-62], BaTiO_3 [63-66], BiFeO_3 [67,68] and $(\text{Ba,Sr})\text{TiO}_3$ [69] and organic barriers such as copolymers films of polyvinylidene fluoride (PVDF) (70%)-trifluoroethylene (TrFe) (30%) [70]. Researchers observed reversal of polarization through an apparent lattice shift, which was accompanied by an I - V diode-like tunneling dependence.

Other interesting types of tunnel junctions are multiferroic tunnel junctions (MFTJ) and are shown in Figure 1.12 (b) and (c). To obtain the Figure 1.12 (b) configuration, the normal metallic electrode in FTJ (Figure 1.12 (a)) is replaced by a ferromagnetic metallic electrode (i.e. $\text{La}_{0.5}\text{Sr}_{0.5}\text{CoO}_3$, LaNiO_3 , SrRuO_3 , $\text{La}_x\text{Sr}_{1-x}\text{MnO}_3$). Another MFTJ structure is shown in Figure 1.12 (c) where a thin multiferroic layer is sandwiched between a ferromagnetic metallic and a metallic electrode. The barrier itself is made of a material that exhibits multiferroic properties in the bulk, such as BFO or BMO. In this case, we expect the following: i) One can obtain a ME MF structure (FE barrier, ferromagnetic metallic electrodes and the respective coupling between them); ii) This coupling in the MFTJ devices allows one to control magnetization M via an electric field E and polarization P via a magnetic field H ; iii) The combination of the TMR and TER effects in MFTJs allow the devices to operate as a four-state resistive system.

Another important point to consider is the effect of the interface bonding and the direction of polarization in the FE barrier. Velez et al. [71], using first-principles calculations of SRO/BTO/SRO MFTJs show that the interface terminations (BaO and TiO_2 for BTO and RuO_2 and SrO for SRO) can significantly change the displacement of



atoms that in turn affects the atomic orbital hybridizations at the interface, which makes the transmission probability different for the two opposite polarization orientations.

Figure 1.12. (a) FE tunnel junction (FTJ), (b), and (c) MF tunnel junctions (MFTJ). Ferroelectric (FE), ferromagnetic metallic (FM), multiferroic (MF) and Metal (M).

1.4.2 Critical thickness for ferroelectricity

Since ferroelectricity is a collective phenomenon, FE thin films are expected to sustain a spontaneous electric polarization only above critical thickness due to extrinsic effects. However, understanding size effects in ferroelectrics is complicated because polarization interacts more strongly with other order parameters, such as compositional fluctuations, strain, and charge, which in turn produce large extrinsic effects, if these variables are uncontrolled. It was believed for a long time that the critical thickness for ferroelectricity is of a few tens of nm [72]. However, from a recent theoretical studies by Junquera and Ghosez [54], the critical thickness was estimated to be ~ 2.4 nm, which makes it possible to effect a FTJ at the nanometer scale (≤ 6 nm) thickness. Due to recent advances in thin film synthesis, it has now become possible to make heterostructures with single crystalline perovskite–oxide films of thickness down to 1 to 2 lattice constants

with epitaxially and atomically sharp interfaces [73]. Typically, these films are prepared with advanced thin film deposition techniques, such as molecular beam epitaxy (MBE), pulsed laser deposition (PLD), chemical vapor deposition (CVD) and atomic layer deposition (ALD). Another important point to consider is the appropriate choice of the substrate materials that permits control of the lattice mismatch between the ferroelectric film and the substrate, allowing the films to grow coherently.

Pulsed laser deposition is one of the most versatile methods to grow high quality films [74]. Several studies had found stable polarization in ultrathin ferroelectric films. Tybell et al. [59] have demonstrated the presence of stable polarization in a 4-nm thick epitaxial film of perovskite ferroelectric $\text{Pb}(\text{Zr}_{0.2}\text{Ti}_{0.8})\text{O}_3$. Experimental evidence for ferroelectricity in ultrathin epitaxial PbTiO_3 films was found at the Argonne National Laboratory where structural investigations by synchrotron radiation demonstrated ferroelectric properties in these films down to 1.2 nm in thickness [60]. Also, ferroelectricity has been observed in mono- molecular layers of FE polymers in the form of PVDF and its copolymers with TrFE [61]. Since it is possible to produce high quality ultrathin FE films, novel applications can be realized by incorporating such films into heterostructures with other materials, producing FTJ and MFTJ structures.

1.4.3 Effect of the depolarization field

In parallel with advances in synthesis, theoretical work has been done to understand the atomic scale of ferroelectricity. Junquera et al. [54] reported first principle calculations of realistic FE-electrode interfaces in BaTiO_3 ultrathin films between two metallic SrRuO_3 electrodes, that when short circuited lose their ferroelectric properties below a critical

thickness of about six-unit cells ($24 \text{ \AA} = 2.4 \text{ nm}$). Physically, this criticality comes from the imperfect screening of the depolarization field, as shown earlier by Dawber et al. [75]. The latter paper incorporated Fermi-Thomas screening in the metal electrodes, whereas the paper by Junquera et al. [54] was a full theoretical model of the system.

The existence of a critical thickness for ferroelectricity is usually explained by depolarization fields produced by the polarization charges accumulated on the surfaces of the film. If the interface films are placed between two metal electrodes, the polarization charges are screened. However, when the thickness is sufficiently reduced, the screening becomes incomplete and at some critical thickness the electrostatic energy associated with the depolarization fields overcomes the energy gained due to the ferroelectric ordering. At this thickness, the ferroelectric state becomes unstable. These results indicate that the screening of the depolarization field is the key to decreasing the critical film thickness.

1.4.4 Role of interface on ferroelectricity at the nanoscale

Another aspect to consider for the ferroelectricity in ultrathin films is the effect of ferroelectric/electrode interfaces due to the bonding of the interfacial atoms [76]. Nanoscale ferroelectricity is strongly affected by interfaces, which significantly influence soft mode displacements of the interfacial atoms in ferroelectrics due to bonding of these atoms to adjacent atoms in the metal electrodes. If the interface bonding is sufficiently strong, the presence of interfaces imposes restrictions on the soft mode motion since the atoms at the boundary of the ferroelectric are pinned to the electrodes. This inevitably affects the displacements of other atoms in the ferroelectric and may completely destroy

the soft mode instability. Furthermore, the presence of interfaces reduces the symmetry of a solid due to the asymmetric local environment at the interfaces compared to the bulk. The reduced symmetry may produce electric dipoles at the interfaces even for a paraelectric state and often gives rise to second harmonic generation. The interface dipoles can be created as a result of interface strain, atomic rippling, non-stoichiometry, and/or modified valence at the interface. Duan et al. [76] performed first principle calculations of ultrathin KNbO_3 ferroelectric films placed between two metal electrodes (i.e. SrRuO_3 or Pt). They show that bonding at the FE-metal interfaces imposes severe constraints on the displacements of atoms, destroying the bulk tetragonal soft mode.

We [62] demonstrated the room temperature polar switching and tunneling behavior in $\text{PbZr}_{0.52}\text{Ti}_{0.48}\text{O}_3$ (PZT) ultra-thin films of 3-7 nm (P3-P7) thickness, sandwiched between platinum and FM $\text{La}_{0.67}\text{Sr}_{0.33}\text{MnO}_3$ (LSMO) layers, this junction also shows magnetic field dependent tunnel current switching in a Pt/PZT/LSMO heterostructure. The capacitance versus voltage graphs show butterfly loops above the coercive field ($> \pm 3$ V) of PZT for a small probe area ($\sim 16 \mu\text{m}^2$). The effect of FE switching was observed in current density versus voltage curves with a large variation in high-resistance/low-resistance (HRS/LRS) ratio (2:1 to 100:1, for different samples). However, these effects were more prominent in the presence of an in-plane external magnetic field. We show the effect of a magnetic field along the in-plane direction. It was observed that when 10 kG was applied to the junction during $J(V)$ measurements, the resistance is decreased only in the positive voltage range (controlled by the LSMO electrode), while no significant change was observed in the negative voltage range (controlled by the Pt electrode). This

is reasonable considering that LSMO becomes more metallic in its FM state. For this junction, the resistance switching between LRS and HRS became sharper, and the HRS/LRS ratio values at zero bias were ~ 60 at 0 G and it increased to 110 with 10 kG. The conductance is fit with Brinkman's model and the parabolic conductance upon bias voltage suggests that electron tunneling governs the transport.

REFERENCES

1. W.J. Merz, *Phys. Rev.* **91**, 513 (1953).
2. E.J. Huibregtse and D.R. Young, *Phys. Rev.* **103**, 1705 (1956).
3. A.F. Davenshire, *Phil. Mag.* **42**, 1065 (1951).
4. C.A. Kittel, 7th ed. (John Wiley & Sons, Inc., New York, 1996).
5. A. Preumont, 2nd ed. (Springer, Netherlands, 2006) 98.
6. F. Gona and G. Shirane. Pergamon press. Oxford (1962).
7. M.E. Lines and A.M. Glass. Clarendon press. Oxford (1977).
8. Robert E. Newnhan. Oxford University Press. Oxford 2005.
9. Eric Cross, *Nature* **432**, 24-25 (2004).
10. Nicola A Hill. *AIP Conf. Proc.* 535, 372 (2000).
11. N. Spaldin and M. Fiebig, *Science* 309, 391 (2005).
12. R.M. Bozorth, (Van Nostrand, New York, 1951), *Rev. Mod. Phys.* **19**, 29 (1947).
13. A.H. Morrish, (John Wiley and Sons, New York, 1965).
14. C. Kittel and J.K. Galt, *Solid State Physics*, **3**, 437 (1956).
15. Yoshinori Tokura. Advance in Condensed Matter Science, volume 2. Gordon and Breach Science Publishers, 2000.
16. E. Dagotto, T. Hotta, and A. Moreo. *Physics Report*, **344**, 1-153 (2001).
17. Schmid, H. *Ferroelectrics*, **162**, 665-685 (1994).
18. L. Martin, S. Crane, Y. Chu, M. Holcomb, M. Gajek, M. Huijben, C. Yang, N. Balke and R. Ramesh, *J. Phys.: Condens. Matter.* **20**, 434220 (2008).
19. Eerenstein W., Mathur N. D. and Scott J. F. *Materials Nature* **442**, 759 (2006).
20. N.A. Hill, *J. Phys. Chem. B* **104**, 6694-6709 (2000).
21. Schmid, H, *Ferroelectrics* **161**, 1-28 (1994).

22. Rivera, J. P. *Ferroelectrics* **161**, 165-180 (1994).
23. Lines, M. E. and Glass, A. M. (Clarendon Press, Oxford) (1977).
24. T. Lottermoser, T. Lonkai, U. Amann, D. Hohlwein, J. Ihringer and M. Fiebig, *Nature* **430**, 541-544 (2004).
25. D. Sanchez, A. Kumar, N. Ortega, R. S. Katiyar, and J. F. Scott. *Appl. Phys. Lett.* **97**, 202910 (2010).
26. D. Sanchez, N. Ortega, A. Kumar, G. Sreenivasulu, R. S. Katiyar, J. F. Scott, D. M. Evans, Miryam Arredondo-Arechavala, A. Schilling, and J. M. Gregg. *J. Appl. Phys.* **113**, 074105 (2013).
27. D. M. Evans, A. Schilling, A. Kumar, D. Sanchez, N. Ortega, M. Arredondo, R. S. Katiyar, J. M. Gregg and J. F. Scott. *Nature Commun.* **4**, 1534 (2013).
28. D. Sanchez, N. Ortega, A. Kumar, R. Roque-Malherbe, R. Polanco, J. F. Scott, and Ram S. Katiyar. *AIP Advances* **1**, 042169 (2011).
29. D. M. Evans, A. Schilling, A. Kumar, D. Sanchez, N. Ortega, R. S. Katiyar, J. F. Scott and J. M. Gregg. *Phil. Trans. R. Soc. A* **372**, 20120450 (2014).
30. J. Schiemer, M. A. Carpenter, D. M. Evans, J. M. Gregg, A. Schilling, M. Arredondo, M. Alexe, D. Sanchez, N. Ortega, R. S. Katiyar, M. Echizen, E. Colliver, S. Dutton, and J. F. Scott. *Adv. Funct. Mater.* **24**, 2993-3002 (2014).
31. Donald M. Evans, Marin Alexe, Alina Schilling, Ashok Kumar, Dilsom Sanchez, Nora Ortega, Ram S. Katiyar, James F. Scott, and J. Marty Gregg. *Adv. Mater.* **27**, 6068-6073 (2015).
32. A. Lookman, R. M. Bowman, J. M. Gregg, J. Kut, S. Rios, M. Dawber, A. Ruediger and J. F. Scott. *J. Appl. Phys.* **96**, 555 (2004).
33. J. Junquera and P. Ghosez. *Nature*. **422**, 506 (2003).
34. L. Esaki, R. B. Laibowitz, P. J. Stiles, *IBM Tech. Discl. Bull.* **13**, 2161 (1971).
35. E. Y. Tsymbal and H. Kohlstedt. *Science*, **313**, 181 (2006).
36. A. Gruverman, D. Wu, H. Lu, Y. Wang, H. W. Jang, C. M. Folkman, M. Ye. Zhuravlev, D. Felker, C. B. Etom, E. Y. Tsymbal, *Nano Lett.*, **9**, 3539 (2009).
37. V. Garcia, S. Fusil, K. Bouzehouane, S. Enouz-Vedrenne, N. D. Mathur, A. Barthelemy, M. Bibes, *Nature*, **460**, 81 (2009).

38. T. Tybell, C. H. Ahn, J.-M. Triscone. *Appl. Phys. Lett.* **75**, 856 (1999).
39. D. D. Fong, G. B. Stephenson, S. K. Streiffer, J. A. Eastman, O. Auciello, P. H. Fuoss, C. Thompson. *Science* **304**, 1650 (2004).
40. A.V. Bune, V.M. Fridkin, S. Ducharme, L.M. Blinov, S.P. Palto, A.V. Sorokin, S.G. Yudin and A. Zlatkin. *Nature*. **391**, 874 (1998).
41. J. Frenkel, *Phys. Rev.* **36**, 1604 (1930).
42. P. M. Tedrow, R. Meservey, *Phys. Rev. Lett.* **26**, 192 (1971); *Phys. Rev. B* **7**, 318 (1973).
43. M. Jullière, *Phys. Lett. A* **54**, 225 (1975).
44. T. Miyazaki and N. Tezuka. *J. Magn. Magn. Mater.* **139**, L231 (1995).
45. J. S. Moodera, Lisa R. Kinder, Terrilyn M. Wong, and R. Meservey. *Phys. Rev. Lett.* **74**, 3273 (1995).
46. W. H. Butler, X.-G. Zhang, T. C. Schulthess, and J. M. MacLaren. *Phys. Rev. B.* **63**, 054416 (2001).
47. J. Mathon and A. Umerski. *Phys. Rev. B.* **63**, 220403 (2001).
48. S.S.Parkin, C. Kaiser, A. Panchul , P.M. Rice, B. Hughe , M. Samant, S.H. Yang. *Nat. Mat.* **3**, 862 (2004).
49. S. Yuasa, T. Nagahama, A. Fukushima, Y. Suzuki, and K. Ando. *Nat. Mat.* **3**, 868 (2004).
50. J. F. Scott, *Nat. Mater.* **6**, 256 (2007).
51. H. Kohlstedt, N. A. Pertsev, J. Rodríguez Contreras, and R. Waser. *Phys. Rev. B.* **72**, 125341 (2005).
52. J. P. Velez, Chun-Gang Duan, K. D. Belashchenko, S. S. Jaswal, and E. Y. Tsymbal. *Phys. Rev. Lett.* **98**, 137201 (2007).
53. A. M. Ionescu, *Nat. Nanotechnol.* **7**, 83 (2012).
54. J. F. Scott, *Science* **315**, 954 (2007).
55. D. Pantel, H. D. Lu, S. Goetze, P. Werner, D. J. Kim, A. Gruverman, D. Hesse, M. Alexe, *Appl. Phys. Lett.* **100**, 232902 (2012).

56. E. Y. Tsymbal, A. Gruverman, V. Garcia, M. Bibes, A. Barthélémy, *Mater. Res. Soc. Bull.* **37**, 138 (2012).
57. J. Rodríguez Contreras, H. Kohlstedt, U. Poppe, R. Waser, C. Buchal, and N. A. Pertsev. *Appl. Phys. Lett.* **83**, 4595 (2003).
58. P. Maksymovych, S. Jesse, P. Yu, R. Ramesh, A. Baddorf, S. Kalinin, *Science*, **324**, 1421 (2009).
59. D. Pantel, S. Goetze, D. Hesse, M. Alexe, *ACS Nano* **5**, 6032 (2011).
60. D. Pantel, H. Lu, S. Goetze, P. Werner, D. J. Kim, A. Gruverman, D. Hesse, M. Alexe. *Appl. Phys. Lett.* **100**, 232902 (2012).
61. H. J. Chen, H. J. Lu, Y. H. Liu, S. Chu, K. Dunn, Ostrikov, A. Gruverman, N. Valanoor, *Appl. Phys. Lett.*, 102, 182904 (2013).
62. D. Barrionuevo, Le Zhang, N. Ortega, A. Sokolov, A. Kumar, Pankaj Misra, J. F. Scott, R. S. Katiyar. *Nanotechnology*. **25**, 495203 (2014).
63. X. S. Gao, J. M. Liu, K. Au, J. Y. Dai, *Appl. Phys. Lett.* **101**, 142905 (2012).
64. A. Chanthbouala, A. Crassous, V. Garcia, K. Bouzehouane, S. Fusil, X. Moya, J. Allibe, B. Dlubak, J. Grollier, S. Xavier, C. Deranlot, A. Moshar, R. Proksch, N. Mathur, M. Bibes, A. Barthélémy, *Nat. Nanotechnol.* **7**, 101 (2012).
65. D. J. Kim, H. Lu, S. Ryu, C.W. Bark, C.B. Eom, E. Y. Tsymbal, A. Gruverman, *Nano Lett.* **12**, 5697 (2012).
66. A. Zenkevich, M. Minnekaev, Y. Matveyev, Y. Lebedinskii, K. Bulakh, A. Chouprik, A. aturin, K. Maksimova, S. Thiess, W. Drube, *Appl. Phys. Lett.* **102**, 062907 (2013).
67. H. Yamada, V. Garcia, S. Fusil, S. Boyn, M. Marinova, A. Gloter, S. Xavier, J. Grollier, E. Jacquet, C. Carrétéro, C. Deranlot, M. Bibes, A. Barthélémy, *ACS Nano*. **7**, 5385 (2013).
68. H. Béa, M. Bibes, S. Cherifi, F. Nolting, B. Warot-Fonrose, S. Fusil, G. Herranz, C. Deranlot, E. Jacquet, K. Bouzehouane, and A. Barthélémy. *Appl. Phys. Lett.* **89** 242114 (2006).
69. Y. W. Yin, M. Raju, W. J. Hu, X. J. Weng, K. Zou, J. Zhu, X. G. Li, Z. D. Zhang, Q. Li, *Front. Phys.* **7**, 380 (2012).
70. H. Qu, W. Yao, T. Garcia, J. Zhang, A. V. Sorokin, S. Ducharme, P. A. Dowben, and V. M. Fridkin. *Appl. Phys. Lett.* **82**, 4322 (2003).

71. J. P. Velev, Ch-G Duan, J. D. Burton, A. Smogunov, M. K. Niranjan, E. Tosatti, S. S. Jaswal, and E. Y. Tsymbal. *Nano Lett.*, **9**, 427, (2009).
72. H. Kohlstedt, N. A. Pertsev, and R. Waser, in *Ferroelectric Thin Films X*, edited by S. R. Gilbert, Y. Miyasaka, D. Wouters, S. Trolier-McKinstry, and S. K. Streiffer, MRS Symposia Proceedings No. 688 (Materials Research Society, Pittsburg, 2002).
73. A. Ohtomo, D.A. Muller, J.L. Grazul, H.Y. Hwang. *Nature*. **419**, 378 (2002).
74. I. Vrejoiu, M. Alexe, D. Hesse, and U. Gösele. *Adv. Funct. Mater.* **18**, 3892 (2008).
75. M. Dawer, P. Chandra, P. B. Littlewood and J.F. Scott. *J. Phys: Condens. Matter*. **15**, L393 (2003).
76. Ch-G. Duan, R. Sabirianov, W.N. Mei, S.S. Jaswal and E. Y. Tsymbal. *Nano Lett.* **6**, 483 (2006).

CHAPTER 2

EXPERIMENTAL AND CHARACTERIZATION TECHNIQUES

2.1. EXPERIMENTAL

2.1.1 Pulsed laser deposition (PLD).

The components of a PLD system (Figure 2.1) are vacuum chamber connected to a turbo pump with a rotating target holder capable of carrying up to six targets, substrate heater, and a laser beam source. The film formation process in PLD generally can be divided into the following four stages:

1. Laser radiation interaction with the target
2. Dynamics of the ablation material
3. Deposition of the ablation material with the substrate.
4. Nucleation and growth of a thin film on the substrate surface.

Each stage in PLD is critical to the formation of high quality oriented and polycrystalline stoichiometric, and uniform thin films.

In the first stage the laser is focused onto the surface of the target by an external lens to the chamber. The laser used in this work was an excimer laser with the wavelength of 248 nm (Krf), the pulse rate range from 1 Hz to 10 Hz and the energy is adjustable from 200 mJ to 550 mJ. In the interaction of the pulsed laser beam with the target the laser energy is converted into thermal, chemical, and mechanical energies, to cause target atoms to be ablated from the surface and the highly directional plasma is formed. The plasma plume contained energetic atoms, molecules, ions and electrons which are highly stoichiometric.

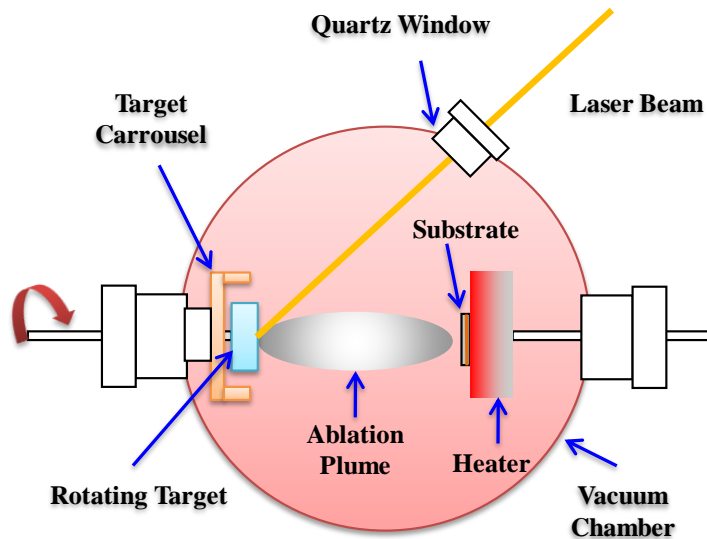


Figure 2.1. Configuration of PLD chamber [1].

The ablation mechanism involved many complex physical phenomena, such as collision, thermal, and electrons excitations.

During the second stage the substance ablated from a target, “the plume” is transported to and deposited on the substrate. The substrate is mounted on the temperature variable heater block. During and after the deposition reactive gases such oxygen is usually injected into the deposition chamber to adjust the stoichiometric of the film. The target to substrate distance is another parameter that governs the angular spread of the ablated materials.

In the third stage there are several other parameters that determine the quality of thin film, these include substrate temperature, the energy density and the frequency of the laser beam. The substrate temperature determines if the films is amorphous or crystalline during the deposition process. The energy density of the laser beam has significant effect on the uniformity of the films.

Multiple targets can be loaded inside the chamber on a rotating holder which can be used to sequentially expose different target to the laser beam, thereby enabling the in-situ growth of heterostructures like multilayer films composed of two or more materials [2].

2.2. STRUCTURAL AND MICROSTRUCTURE CHARACTERIZATION

2.2.1 X-ray diffraction technique

X-Rays are only a small part of the electromagnetic spectrum with wavelengths (λ) ranging from 0.02 Å to 100 Å having typical photon energies in the range of 100 eV - 100 KeV. X-rays used to study crystals have λ of the order of 1 to 2 Å (1 KeV- 120 KeV), these are much more energetic, i.e. they can penetrate deeper into a material. X-ray diffraction is the result of interaction between x-ray and the periodic electronic potential geometry of the crystal. The diffraction of an x-ray beam striking a crystal occurs because the wavelengths (λ) of the x-ray beam is similar to the spacing of atoms in materials (1-10 Å). When an x-ray beam encounters the regular 3-D arrangement of atoms in a crystal most of the x-ray will destructively interfere with each other and cancel each other out, but in some specific directions they constructively interfere and reinforce one another. It is these reinforced (diffracted), because of which the diffracted waves will consist of sharp interference maxima (peaks) with the same symmetry as in the distribution of atoms in a material, later these x-rays produce the characteristic x-ray diffraction patterns to determine the crystal structure of the material.

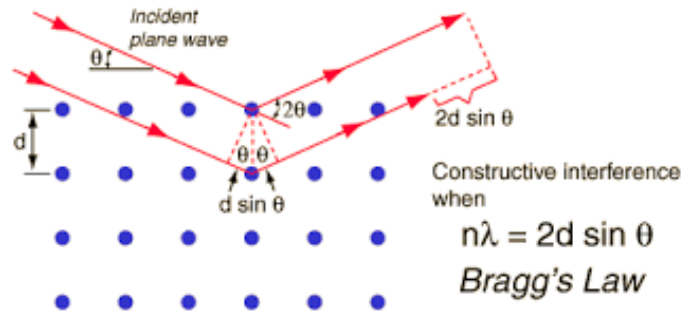


Figure 2.2. Bragg's law [3].

W.L. Bragg showed that diffracted x-rays act as if they were "reflected" from a family of planes within crystals (Figure 2.2). Bragg's planes are the rows of atoms that make up the crystal structure. These "reflections" were shown to only occur under certain conditions which satisfy the Bragg equation:

$$n\lambda = 2d \sin \theta \quad (2.1)$$

Where, n is an integer (1, 2, 3, n), λ is the wavelength, d is the distance between atomic planes, and θ is the angle of incidence of the x-ray beam and the atomic planes. $2d \sin \theta$ is the path length difference between the two incident x-ray beams, where one x-ray beam takes a bit longer (but parallel) path because, it reflects off an adjacent atomic plane. This path length difference must equal an integer value of λ the incident x-ray beam for constructive interference to occur, such that a reinforced diffracted beam is produced [3].

2.2.2 Atomic force microscopy (AFM)

The atomic force microscopy (AFM) system is comprised of the scanner and the AFM detection system. The scanner houses the piezoelectric transducer. The piezo

element physically moves the sample in the X, Y and Z direction. The detection system consists of a laser which generates a spot of light that is reflected off of a micro-fabricated cantilever onto a mirror and finally into a photodetector (Figure 2.3). The position of the spot is determined by circuitry which generates a voltage from the difference between the photodiode segments ($A - B$). The circuit outputs a voltage ranging from +10 V to -10 V depending on the position of the spot on the two photodiodes.

The AFM system maintains the tip at the end of the cantilever in contact with the sample surface. The sample is scanned under the tip in X and Y. Features on the sample surface deflect the cantilever, which in turn change the position of the laser spot on the photodiodes. This position change is read by the feedback loop [4].

The feedback loop moves the sample in Z to restore the spot to its original position (Figure 2.3).

1. A flat portion of the sample surface is scanned beneath the tip left-to-right, maintaining the laser beam at the center of the photodiode array.
2. As the tip encounters a raised feature, the cantilever is pushed up and the laser beam is deflected onto the “A” portion of the array. With the “A” photodiode receiving an increased portion of the laser light, its voltage increases while portion “B’s” decreases ($A > B$).
3. The Vertical Deflection ($A-B$) voltage differential is sensed by the feedback electronics, causing a dropped voltage to the Z piezo crystal-the piezo retracts. As the Z piezo retracts, the cantilever recenters the laser beam onto the photodiode array ($A = B$).

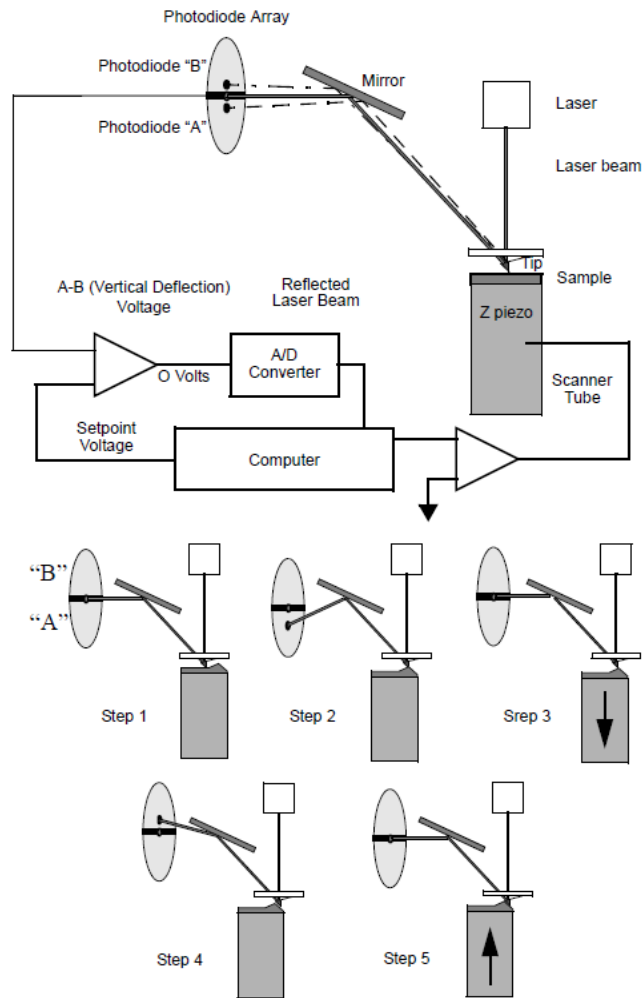


Figure 2.3. Contact AFM concepts (Steps 1-5) [4].

4. As the tip encounters a decline in the sample topology, the tip drops. This directs more of the beam onto the “B” portion of the photodiode array. With the “B” photodiode receiving an increased portion of the laser light, its voltage increases while portion “A’s” decreases ($A < B$).

5. Again, the Vertical Deflection (A-B) voltage differential is sensed by the feedback electronics, increasing voltage to the Z piezo crystal-the piezo extends. As the Z piezo

extends, the tip is pushed down until the laser beam recenters on the photodiode array (A = B).

The AFM always first engages in the repulsive region of its operating range. In other words, the cantilever exerts a positive pressure on the sample surface. The AFM block diagram shows the relationship between the cantilever movement and the laser spot on the photodiode array. The diagram shows that the spot moves onto “A” when the cantilever is pushed up.

2.3. ELECTRICAL CHARACTERIZATION

2.3.1 Dielectric and impedance measurements

The capacitance (C) and loss tangent ($\tan \delta$) were measured using an HP 4294 impedance analyzer. The Agilent 4294A covers a broader test-frequency range (40 Hz to 100 MHz) with Basic impedance accuracy: $\pm 0.08\%$. The DC bias range is 0 V to ± 40 V or 0 mA to ± 100 mA. The temperature dependence of the impedance/dielectric measurements were carried out over the wide range from 100 K to 640 K and the temperature was controlled with an accuracy of $\pm 0.7^\circ\text{C}$ using a temperature controller (K-20 MMR technologies, Inc.).

2.3.2 Ferroelectric measurements

The ferroelectric hysteresis loops of the multilayer thin films were examined using a ferroelectric measurement system RT6000 HVS; Radiant Technologies, Inc. [5] The polarization hysteresis of the films were measured with a voltage range of - 20 V to 20 V and temperature dependence in the range 100 K to 650 K. Apart from the

hysteresis, the instrument also allows us to measure fatigue properties of the films. Frequency variation of the ferroelectric hysteresis loop was done in the frequency (50 Hz – 100 KHz) and temperature (100 K - 300 K) ranges using a Precision Premier II from Radiant technologies equipped with vision data management software.

2.3.3 Top electrode

In this work the dielectric, impedance and ferroelectric properties were studied in planar capacitor with metal-ferroelectric-metal (MFM) configuration by using Platinum Pt/TiO₂/SiO₂/Si as top electrode. It was deposited by DC sputtering with a square mask of ~100 μ m side and ~ 70 nm thick.

2.3.4 Piezoresponse force microscopy (PFM)

To measure the deformations of a piezoresponse (PR) material in the vertical or lateral direction, the sample is actuated using an AC electric field. The atomic force microscopy (AFM) is operated in contact mode where the tip touches the surface of the PR material and maintains a constant average deflection δ [6, 7]. In response to the applied AC electric field, the sample expands and contracts. The vertical deflection of the cantilever measured by the four-quadrant photodiode detector is the input source to a lock-in amplifier. The vertical deflection is modulated at the same frequency as the applied electric field.

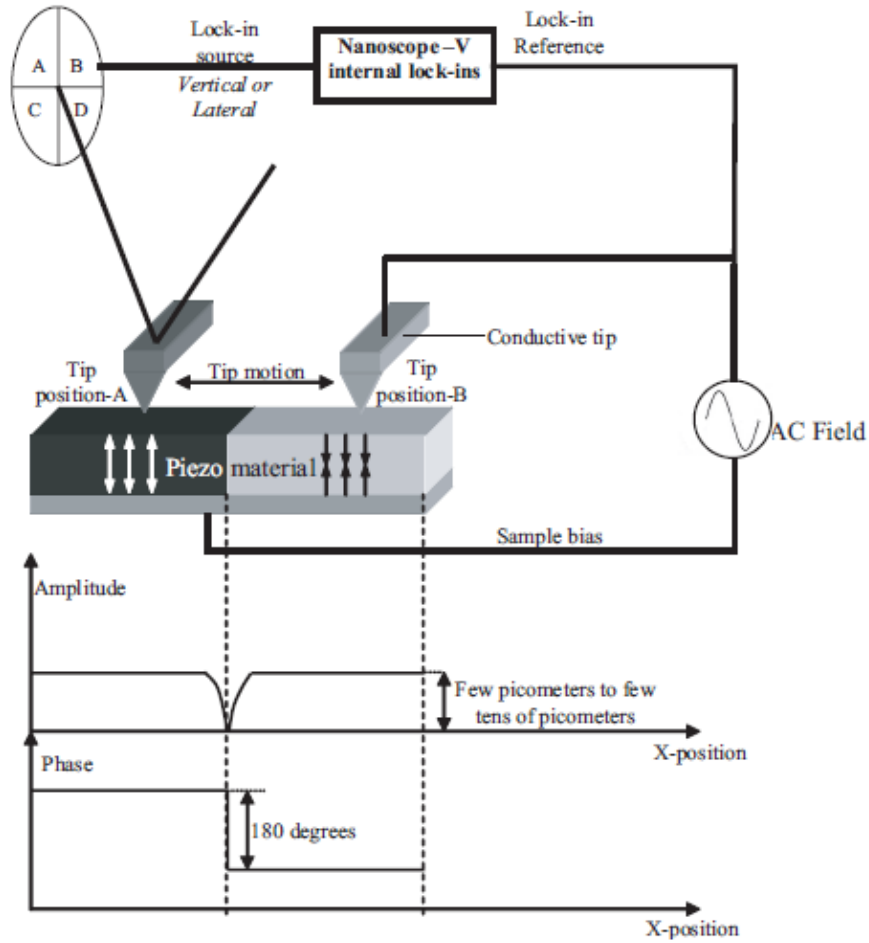


Figure 2.4. Schematic of piezoresponse measurement in contact mode AFM [6].

An important point is that the changes in the vertical deflection, when translated into physical units, are of the order of a few picometers to a few tens of picometers. This necessitates the use of a lock-in amplifier to measure such small signals. The applied electric field is the reference input to the lock-in amplifier.

The NanoScope V Controller has three internal lock-ins. Lock-ins 1 and 2 are capable of operating up to 5MHz (denoted as high-speed) while lock-in 3 is capable of operating up to 50kHz (denoted as low-speed). Figure 2.4 shows a schematic of a contact mode AFM with a piezoresponse measurement set-up. The AFM tip is maintained with a constant

deflection delta on the surface of a PR material. The vertical (or lateral) deflection of the cantilever signal is the first input (source) to the NanoScope Controller internal lock-in. AC bias is applied to the sample (or tip) causing the PR material to expand and contract. This is the second input (reference) to the NanoScope Controller internal lock-in. At tip position-A in Figure 2.4, suppose that the domains of the PR material oscillate in-phase with the AC drive signal. The lock-in amplifier measures the component of the deflection signal that oscillates in-phase with the AC drive signal and the component of the deflection signal that oscillates perpendicular (at 90 degrees) to the AC drive signal. From these two signals, the amplitude and the phase angles of the deflection signal are calculated and displayed in the software. When the tip moves over to position-B, the domains of the PR material oscillate out-of-phase with respect to the AC drive signal and similar information is collected via the lock-in amplifier.

At the domain wall, ideally the amplitude drops to zero and the phase measured by the lock-in amplifier changes by 180 degrees. To translate the amplitude of the PR oscillations from volts to picometers, you must calibrate the deflection sensitivity of the cantilever. Similar measurements may be performed to image the lateral domains in a PR material by setting the lock-in source for the amplifier to lateral deflection.

2.4. MAGNETIC CHARACTERIZATION

2.4.1 Vibration Sample Magnetometer (VSM)

In a VSM a sample is vibrating in the vicinity of a set of pick-up coils. The flux change (Φ) caused by the moving magnetic sample causes an induction voltage (V) across the terminals of the pick-up coils which is proportional to the magnetization of the

sample: $V(t) = C \frac{\partial \Phi}{\partial t}$. Figure 2.5 shows a VSM diagram. The sample is suspended from a vibrating drive head by a non-magnetic rod and placed between two electromagnets which produce a magnetic field. The vibrator generates a vertical sinusoidal vibration. Therefore, the sample experiences sinusoidal motion, which induces an electrical signal in the coils mounted on the pole faces of the electromagnets.

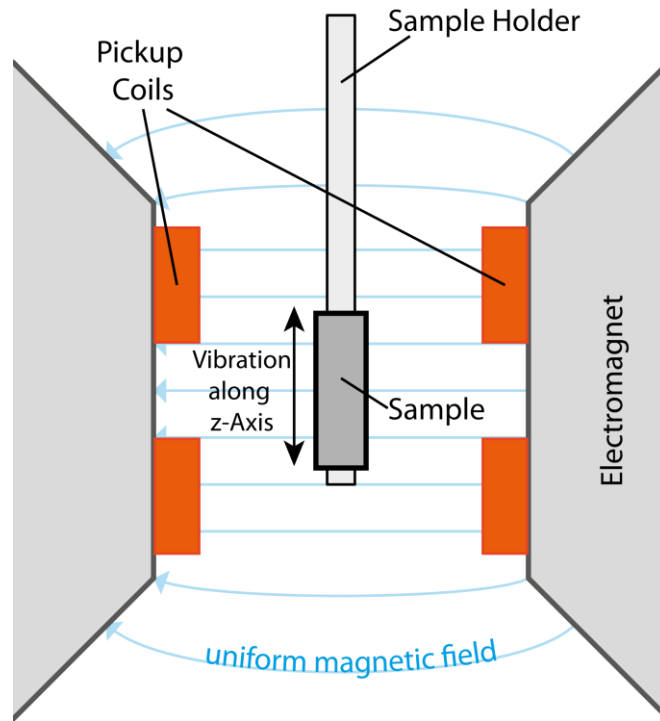


Figure 2.5. Schematic of a VSM system. The signal in the pick-up coils is caused by the flux change produced by the moving magnetic sample [12].

The signal picked up by the coils is proportional to the frequency and amplitude of the sinusoidal motion, and the total magnetic moment of the sample at the applied magnetic field. The frequency and amplitude of the sinusoidal motion are maintained constant by a capacitor (reference signal generator). By feeding the signals from the pick-up coils and

the reference signal into a demodulator, the magnetic moment of the sample is extracted [8].

2.4.2 Superconducting Quantum Interference Device Megnetometer (SQUID)

SQUID is very sensitive magnetometer used to measure very small magnetic fields, based on superconducting loops containing Josephson Junctions. A Josephson junction is made up of two superconductors, separated by an insulating layer so thin that electron can tunnel through. In superconductors, current is carried by pairs of electrons, known as Cooper pairs, the superconductive electron pairs are not scattered they are coupling over a range of hundreds of nanometers. The SQUID uses the properties of electron-pair wave coherence and Josephson junctions to detect very small magnetic fields. The resolution threshold for SQUID is $\sim 10^{-12}$ T. SQUIDs generally use two Josephson junctions, as is show in Figure 2.6.

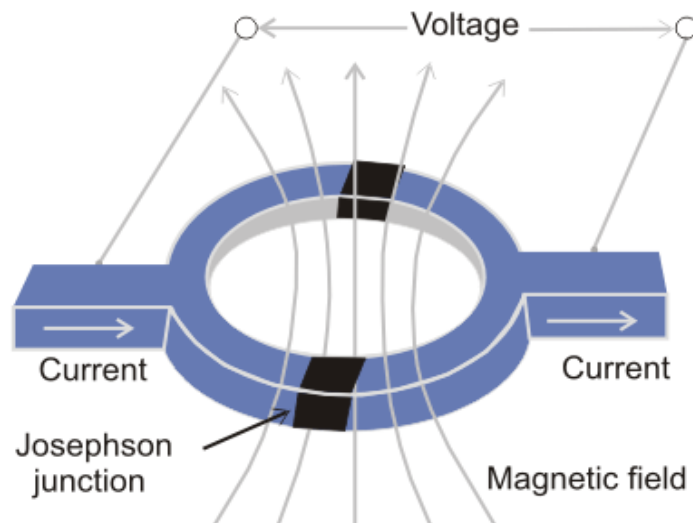


Figure 2.6. Two parallel Josephson junctions. SQUID [9].

When the insulator layer is thin enough, electron pairs can actually tunnel through the barrier with phase coherent. If there is not magnetic field, the current is divided equally between the two junctions and there is no phase difference across the two junctions. But when the magnetic field is applied, the current in these two junctions are not equal, but the sum remains constant. This kind of relationship gives a periodic dependence of the magnitude of the magnetic field. A set of superconducting loops act as detection gradiometer coils, which are accurately balanced and arranged in a configuration that only detects the magnetic flux induced by the magnetization of the sample (expels the uniform field applied to the sample by the superconducting magnet). As the sample moves through the coils, the magnetic moment of the sample induces an electric current in the detection coils. Since the coils, the connecting wires and the SQUID input coil form a closed superconducting loop, this current is not damped so that any change in magnetic flux in the detection coils producing a proportional change in the persistent current in the detection circuit.

2.4.3 Physical property measurement system (PPMS)

The Quantum Design Vibrating Sample Magnetometer (VSM) option for the Physical Property Measurement System (PPMS) family of instruments is a fast and sensitive DC magnetometer. The basic measurement is accomplished by oscillating the sample near a detection (pickup) coil and synchronously detecting the voltage induced. By using a compact gradiometer pickup coil configuration, a relatively large oscillation amplitude (1-3 mm peak) and a frequency of 40 Hz, the system is able to resolve magnetization changes of less than 10^{-6} emu at a data rate of 1 Hz.

The VSM option consists primarily of a VSM linear motor transport (head) for vibrating the sample, a coilset puck for detection, electronics for driving the linear motor transport and detecting the response from the pickup coils, and a copy of the MultiVu software application for automation and control [10].

2.4.3.1 Theory of operation

The basic principle of operation for a vibrating sample magnetometer is that a changing magnetic flux will induce a voltage in a pickup coil. The time-dependent induced voltage is given by the following equation:

$$V_{coil} = \frac{d\Phi}{dt} = \left(\frac{d\Phi}{dz}\right) \left(\frac{dz}{dt}\right) \quad (2.2)$$

In equation (2.2), Φ is the magnetic flux enclosed by the pickup coil, z is the vertical position of the sample with respect to the coil, and t is time. For a sinusoidally oscillating sample position, the voltage is based on the following equation:

$$V_{coil} = 2\pi f C m A \sin(2\pi f t) \quad (2.3)$$

In equation (2.3), C is a coupling constant, m is the DC magnetic moment of the sample, A is the amplitude of oscillation, and f is the frequency of oscillation.

The acquisition of magnetic moment measurements involves measuring the coefficient of the sinusoidal voltage response from the detection coil. Figure 2.7 illustrates how this is done with the VSM option.

The sample is attached to the end of a sample rod that is driven sinusoidal. The center of oscillation is positioned at the vertical center of a gradiometer pickup coil. The precise position and amplitude of oscillation is controlled from the VSM motor module using an optical linear encoder signal readback from the VSM linear motor transport. The voltage

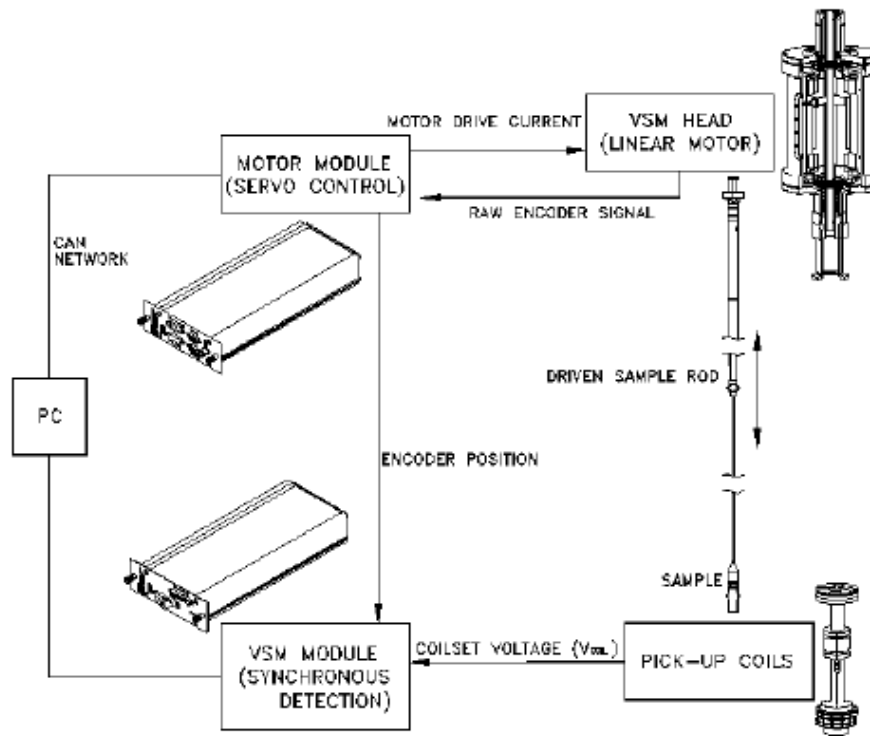


Figure 2.7. Operating principle for the VSM option [10].

induced in the pickup coil is amplified and lock-in detected in the VSM detection module. The VSM detection module uses the position encoder signal as a reference for the synchronous detection. This encoder signal is obtained from the VSM motor module, which interprets the raw encoder signals from the VSM linear motor transport. The VSM detection module detects the in-phase and quadrature-phase signals from the encoder and from the amplified voltage from the pickup coil. These signals are averaged and sent over the CAN bus to the VSM application running on the PC.

2.4.4 Magnetic force microscopy (MFM)

MFM imaging utilizes the Interleave and Lift Mode procedures. In MFM, a tapping cantilever equipped with a special tip is first scanned over the surface of the sample in tapping mode to obtain topographic information. Using Lift Mode as shown in Figure 2.8, the tip is then raised just above the sample surface. Surface topography from the initial scan is added to the lift height to maintain constant separation during the lifted scan. The influence of magnetic force is measured using the principle of force gradient detection. In the absence of magnetic forces, the cantilever has a resonant frequency f_0 . This frequency is shifted by an amount Δf proportional to m_{all} , typically in the range 1-50Hz for cantilevers having a resonant frequency $f_0 \sim 100$ kHz. These frequency shifts can be detected three ways: phase detection, which measures the cantilever's phase of oscillation relative to the piezo drive; amplitude detection, which tracks variations in oscillation amplitude; and frequency modulation, which directly tracks shifts in resonant frequency. Phase detection and frequency modulation produce results that are generally superior to amplitude detection.

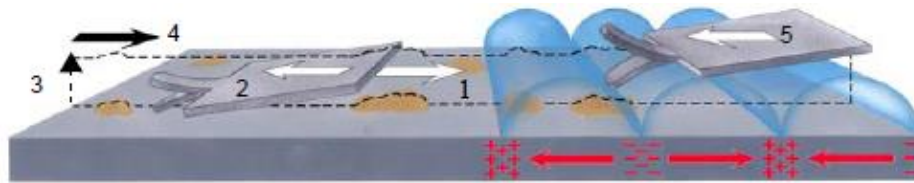


Figure 2.8. MFM Lift Mode principles [11].

1 and 2 - Cantilever traces surface topography on first trace and retrace.

3 - Cantilever ascends to Lift scan Height.

4 and 5 - Lifted cantilever profiles topography while responding to magnetic influences on second trace and retrace.

For MFM procedures, magnetic coated tips are required. Various kinds of MFM probes are available for specific applications. The remainder of this chapter assumes that the reader is familiar with the operation of tapping mode to obtain topographical images of a sample surface and has read the description of Interleave scanning. LiftMode allows the imaging of relatively weak but long-range magnetic interactions while minimizing the influence of topography (Figure 2.8). Measurements are taken in two passes across each scan line; each pass consists of one trace and one retrace. In the first pass, topographical data is taken in tapping mode on one trace and retrace. The tip is then raised to the lift scan height and a second trace and retrace

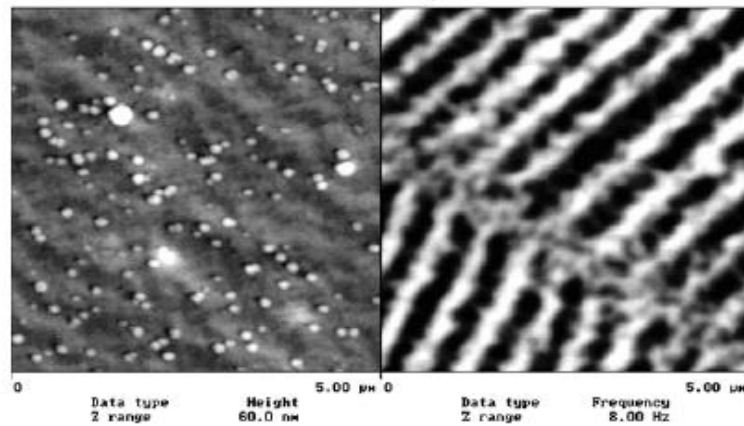


Figure 2.9. Topographic (left) and magnetic force gradient image (right) of metal evaporated tape at 100 nm [11].

performed while maintaining a constant separation between the tip and local surface topography. Magnetic interactions are detected during this second pass. Using LiftMode, topographical features are virtually absent from the MFM image (Figure 2.9).

2.5. TRANSPORT PROPERTIES

2.5.1 Current-voltages characteristic

Conduction mechanism through ferroelectric thin film has been an active area of research over the years. Many mechanisms have been proposed for the conduction in the ferroelectric thin films. In particular, Direct tunneling, Schottky thermionic emission, and Fowler-Nordheim tunneling were considered as possible sources of leakage currents in ferroelectric capacitors [12, 13]. This transport behavior changes dramatically when a film thickness approaches a nanometer scale, making direct tunneling the dominant mechanism of conduction [14]. The current-voltage (I-V), conductance, and resistive properties will be used to verify the quality of a tunnel junction and to prove that tunneling is the main source of the conductance. Dependence with the polarization state of the barrier (electroresistance) and the magnetization aligned in the metallic electrodes (magnetoresistance) in FTJ and MFTJ will be measured. In order to study the charge transport properties through the ultrathin FE and MF layer, tunnel junctions will be fabricated using the LSMO films as the bottom electrode and top electrode will be fabricated by lithography technique [15]. Photolithography, also termed optical lithography or UV lithography, is a process used in microfabrication to pattern parts of a thin film or the bulk of a substrate. It uses light to transfer a geometric pattern from a photomask to a light-sensitive chemical "photoresist", or simply "resist," on the substrate. A series of chemical treatments then either engraves the exposure pattern into, or enables deposition of a new material in the desired pattern upon, the material underneath the photo resist.

REFERENCES

1. <http://superconductivity.et.anl.gov/Techniques/PLD.html>
2. D. B. Chrisey and G. K. Hubler Editors, Pulsed Laser Deposition of Thin Films. John Wiley & Sons, New York, 1994
3. <http://www.csam.montclair.edu/earth/eesweb/gorring/geos443/443notes/xray.html>
4. Veeco - diMultiMode V- SPM Instruction Manual (004-995-000) (004-995-100).
5. RT6000 HVS Radiant Manual, Radiant technologies Inc. New Mexico, 1994.
6. Veeco - Piezoresponse Atomic Force Microscopy-Using a NanoScope V Controller- User Guide-013-444-000.
7. A. Gruverman, O. Auciello and H. Tokumoto, "Imaging and control of domain structures in ferroelectric thin films via scanning force microscopy," *Annu. Rev. Mater. Sci.* **28**:101-123 (1998).
8. www.el.utwente.nl/tdm/istg/research/vsm/vsm.htm
9. Ran, Shannon K'doah (2004).
10. Vibrating Sample Magnetometer (VSM) Option User's Manual Part Number 1096-100, B0.
11. Veeco - diMultiMode V- SPM Instruction Manual (004-995-000) (004-995-100)- Chapter 12 Magnetic Force (MFM) Imaging.
12. M. Dawber, K. M. Rabe, and J. F. Scott, *Rev. Mod. Phys.* **77**, 1083 (2005).
13. J. F. Scott, *J. Phys. Condens. Matter.* **18**, R361 (2006).
14. T. Tybell, C. H. Ahn, J.-M. Triscone. *Appl. Phys. Lett.* **75**, 856 (1999).
15. K. Bouzehouane, S. Fusil, M. Bibes, J. Carrey, T. Blon, M. Le D, P. Seneor, V. Cros, and L. Vila. *Nano Lett.* **3**, 1599 (2003).

CHAPTER 3

THICKNESS DEPENDENT FUNCTIONAL PROPERTIES OF MULTIFERROIC HETEROSTRUCTURES

3.1. INTRODUCTION

Recent advances in thin film technologies make it possible to fabricate multiferroic heterostructures at nanoscale by artificial designing. Multiferroic heterostructures thin films of ferromagnetic and ferroelectric materials have attracted particular interest for their properties [1-4] which provide a unique opportunity to exploit several functionalities which could yield a new device concept, such as magneto-electric nonvolatile memory elements (NVRAM) and ferroelectric/multiferroic tunnel junctions (FTJ and MFTJ). A typical magnetic tunnel junction (MTJ) consists of two metallic ferromagnetic layers separated by an ultrathin insulating oxide layer. Recently a great interest has emerged for the study of tunnel junction (TJ) structure using polar barrier (i.e. ferroelectric/multiferroic) due to the possibility that these structures can produce a four-state system. Some heterostructures studied using ultrathin polar barrier (thickness less than 5 nm), are: $\text{BaTiO}_3(\text{BTO})/\text{La}_{0.67}\text{Sr}_{0.33}\text{MnO}_3(\text{LSMO})$ [5], $\text{Co/PbZr}_{0.2}\text{Ti}_{0.8}\text{O}_3/\text{La}_{0.7}\text{Sr}_{0.3}\text{MnO}_3$ [6], $\text{LSMO}/\text{Ba}_{0.95}\text{Sr}_{0.05}\text{TiO}_3/\text{LSMO}$ [7], BTO/LSMO [8], $\text{BaTiO}_3/\text{SrRuO}_3$ (SRO) [9]. A considerable number of studies has been done on the thickness effect on ferroelectric properties in thin films, but not much attention has been placed on the effect of the polar layer (ferroelectric or multiferroic) on the ferromagnetic metallic bottom electrode (such as, LSMO or SRO) and the importance of interface effect between polar layer and metallic electrode as the thickness of the polar layer is decreased.

In MFTJ and FTJ devices one of the more popular electrodes used is $\text{La}_{1-x}\text{Sr}_x\text{MnO}_3$ manganite perovskite. This compound can be ferromagnetic insulator (FI) or ferromagnetic metal (FM) at room temperature, depending upon the concentration x . FM $\text{La}_{0.67}\text{Sr}_{0.33}\text{MnO}_3$ is well studied due to its unusual electronic structure and the strong interplay between magnetic ordering and charge transport properties leading to colossal magnetoresistance. Since the ferromagnetic properties in LSMO are mainly due to the double exchange interaction between Mn^{+3} and Mn^{+4} mediated via oxygen, the electrical and magnetic properties of the manganites are mainly determined by the Mn valence, which is described as a mixture of Mn^{3+} and Mn^{4+} , correlated with the ratio between trivalent (La^{+3}) and divalent (Sr^{+2}) cations as well as the oxygen (non) stoichiometry [10-14]. Due to the above mentioned facts the magnetic properties of LSMO thin films are very susceptible to the processing conditions and the interface effects [15].

Tunneling magnetoresistance properties are highly dependent of the interface with the electrodes, interface effects have been reported to play an important role in the properties of materials having thickness less than 100 nm [16-19]. Blom et al. [16] have reported a change in transport properties due to the metal-ferroelectric (M-FE) interface in semiconducting $\text{La}_{0.5}\text{Sr}_{0.5}\text{CoO}_3/\text{PbTiO}_3/\text{Au}$ (LSCO/PT/Au) structures. LSCO/PT/Au structures showed a difference of two orders of magnitude in the current through the ferroelectric PT film between LSMO-bottom and Au-top electrode at a bias of 1 V due to the polarization dependent internal electric field. This change was attributed to the variation in the width of Scottky barrier, which is reduced/increased when the polarization in the space charge region at the diode is parallel/antiparallel to the internal electric field. Later Jiang et al. [17] proposed that $\text{SrRuO}_3/\text{BiFeO}_3/\text{Pt}$ (SRO/BFO/Pt)

structures can function as a resistive memory where the conductivity can be modulated by BFO ferroelectricity. Scherwitzl et al. [18] also showed electric field control of the metal-insulator transition in NbNiO_3 nickelates.

Jiang et al. [19] reported drastic changes in transport and magnetic properties of ultra-thin $\text{La}_{0.8}\text{Sr}_{0.2}\text{MnO}_3$ (LSMO) layers capped with ferroelectric $\text{PbZr}_{0.2}\text{Ti}_{0.8}\text{O}_3$ (PZT). They attributed the modified properties to the modulation of charge carriers by the ferroelectric field effect at the interface; this effect increased both magnetization and phase transition temperature while decreasing the resistivity in PZT/LSMO bilayer structures compared with the pure LSMO films.

Additional studies have been done related to the effect of metal top electrode (cap) on LSMO. Plecenik et al. [20] studied the interface effect of LaMnO_3 with Al, In, Au, and Pb. Presence of anomaly peak in resistance vs. temperature was attributed to the formation of a depletion layer due to the migration of oxygen from LaMnO_3 to the metal with a subsequent change in the $\text{Mn}^{3+}/\text{Mn}^{4+}$ ratio and these results were confirmed by x-ray photoelectron spectroscopy (XPS) [20]. It was also observed that capping LSMO thin films with Au has sizable effects on the manganite Curie temperature and saturation magnetization [15, 21]. Liu et al. reported that the Au-capping layers on thinner (3 - 4 nm) Fe_3O_4 films significantly increase the uniaxial magnetic anisotropy originating from the magnetoelastic interactions due to the lattice mismatch at the Au/ Fe_3O_4 interface [22]. The effect of $\text{YBa}_2\text{Cu}_3\text{O}_{7-\delta}$ cap layers on the magnetic and electronic properties of LSMO have also been studied [23, 24]. $\text{PbZr}_x\text{Ti}_{1-x}\text{O}_3$ (PZT) thin and ultrathin films have been promising candidates for FeRAM and FTJ applications, due to its high remnant

polarization (P_r) and low coercive field (E_c) [25] and presence of a stable polarization in ultrathin (~ 4 nm) epitaxial film [26].

3.2. EXPERIMENTAL DETAILS

3.2.1 Growth of PZT and LSMO bilayer thin films by pulsed laser deposition.

$\text{PbZr}_{0.52}\text{Ti}_{0.48}\text{O}_3/\text{La}_{0.67}\text{Sr}_{0.33}\text{MnO}_3$ (PZT/LSMO) bilayer thin films with different thicknesses of PZT were fabricated by pulsed laser deposition (PLD) employing a KrF excimer laser ($\lambda=248$ nm) on $(\text{LaAlO}_3)_{0.3}(\text{Sr}_2\text{AlTaO}_6)_{0.7}$ (LSAT) (001)-oriented substrates (Figure 3.1 (a)). The PZT and LSMO were grown at 600 °C and 700 °C respectively under an oxygen pressure of 80 mTorr, using a laser energy density of 1-2 J/cm² and deposition frequency of 5 Hz, followed by annealing at 700 °C for 30 min in oxygen at a pressure of 320 Torr. Finally, the films were cooled down to room temperature at a slow rate. The thickness of LSMO was ~ 60 nm for all bilayers, while the thicknesses of the PZT thin films varied: 100, 50, 25, and 10 nm for each bilayer structure. These bilayer films will be identified in the manuscript and figures as P100, P50, P25 and P10 respectively. Films were deposited from ceramic targets of LSMO and PZT (with 20 % excess of Pb) which were synthesized at 930 °C and 1250 °C, respectively by solid state reaction.

3.2.2 Structural, ferroelectric, and magnetic experimental details.

The crystal structure was characterized using X-ray diffraction (XRD) technique with a $\text{CuK}\alpha$ radiation, a step size 0.02° and scanning speed of 1.5 °/min. XRD patterns were recorded over the angular range 20°-60° (2θ) with wavelength of $\lambda = 1.5405$ Å.

Atomic force microscopy (Veeco-AFM-contact mode) was used to examine the morphology and the surface roughness of the films. The film thickness was determined using an X-P-200 profilometer. The electrical measurements were carried out a metal-insulator-metal (MIM) configuration with Pt top electrode (square of side 100 μm) deposited by dc sputtering through a shadow mask. The capacitance and loss spectra were measured in the temperature range of 100 $^{\circ}\text{C}$ to 640 $^{\circ}\text{C}$ for frequencies between 100 Hz to 1 MHz by using a programmable temperature controller (MMR K-20) and an impedance analyzer (HP 4294A). Ferroelectric hysteresis loops were measured using a hysteresis loop tester (Radiant Technologies RT6000 HVS). The magnetic measurements were performed using a vibrating-sample magnetometer (VSM-lakeshore 736) at room temperature. The magnetization (M) versus temperature (T) and magnetization (M) versus magnetic field (H) measurements were performed using Quantum Design MPMS XL-7 SQUID magnetometer. For M versus T data, the samples were cooled from 300 K to lowest temperature 2 K in presence of zero-field and then the magnetic field of 500 Oe was applied and M versus T data was recorded while heating the sample from 2 K to 350 K. This is denoted as ZFC data. After the sample reached 350 K, the sample was again cooled in the same applied field to the lowest temperature. Again the M versus T data was recorded during heating the sample in the same applied field from 2 K to 350 K. This is denoted as FC data. M-H loops at 300 K and 5 K were measured in magnetic field range ($-50 \text{ kOe} \leq H \leq 50 \text{ kOe}$). For M-H loop at 5 K, sample was cooled in zero-field from 300 K down to 5 K and the measurements were made at 5 K for the complete loop.

3.3. STRUCTURAL CHARACTERIZATION

Figure 3.1 (b) shows the x-ray diffraction (XRD) patterns of the five different PZT/LSMO highly oriented bilayer films for different PZT layer thicknesses deposited on the LSMO. In all heterostructures only the (00 l) reflections corresponding to the LSAT substrate, PZT and LSMO layers were present in θ -2 θ scan in the range of 20°-60°, without appearance of any additional peak or intermediate phase. These observations suggest that individual PZT and LSMO phases were retained in the bilayer structures. A close view of the (001) and (002) reflections are presented in Figure 3.1 (c) and (d) respectively. As the thickness of PZT increase from 10 nm to 100 nm, the peaks at ~22° and ~45° are observed to change as follows: i) gradually strengthened ii) narrowing, and iii) slight shift to higher angles. The possible reasons behind these effects are the different strains experienced due to lattice mismatch between LSMO/LSAT and PZT and due to the improvement of crystallinity with increasing PZT thickness; although, the thermal expansion coefficient values of LSAT ($10 \times 10^{-6} \text{ }^\circ\text{C}^{-1}$), LSMO ($12 \times 10^{-6} \text{ }^\circ\text{C}^{-1}$) and PZT ($11 \times 10^{-6} \text{ }^\circ\text{C}^{-1}$) [27] are very close to each other. Bulk LSAT and LSMO have a cubic perovskite structure with lattice parameter of $a_{\text{LSAT}} = 3.868 \text{ \AA}$ $a_{\text{LSMO}} = 3.871 \text{ \AA}$ respectively, while PZT has a tetragonal perovskite structure with $a_{\text{PZT}} = 4.036 \text{ \AA}$ and $c_{\text{PZT}} = 4.146 \text{ \AA}$. Hence, LSMO on LSAT and PZT on LSMO experience an in-plane strain of -0.078% and -4.26% respectively. Due to the high compressive stress experienced for PZT, it is expected to decrease/increase the in or out of plane lattice parameter respectively; however, the strain effect decreases with increase in film thickness. Kim et al. [27] have observed a pronounced change in lattice constant with the increase in PZT thickness at the micron-level. For film with 10 nm thickness, a broad

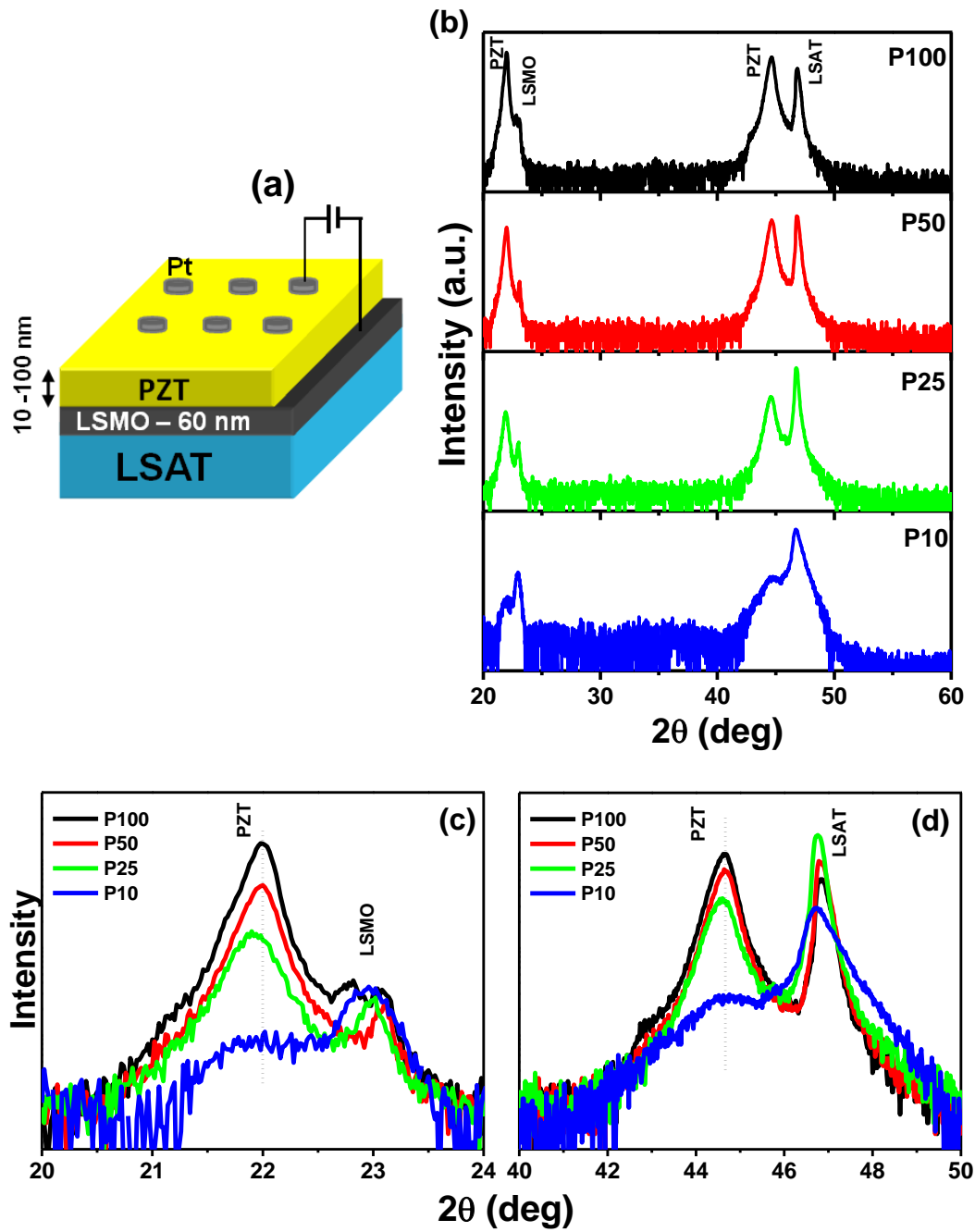


Figure 3.1. (a) A sketch of the PZT thin films sandwiched between Pt top and LSMO bottom electrodes, (b) θ - 2θ diffractograms for PZT films grown on LSMO(60 nm) coated LSAT (001) substrate for thicknesses ranging from 10 nm to 100 nm, (c) and (d) show a close view of (001) and (002) XRD reflections respectively.

peak was observed that may be due to non-uniform distribution of the strain and possible presence of different kind of dislocations [18].

Figure 3.2 shows the topography images obtained in a contact mode on a $3 \times 3 \mu\text{m}^2$ area of the top surface of PZT/LSMO/LSAT heterostructures. The thickness of the PZT layer was varied from ~ 100 nm (P100) to ~ 10 nm (P10), while the thickness of LSMO was keep constant (~ 60 nm) in all structures. We have kept the z-scale of all images at constant height ~ 30 nm to compare among

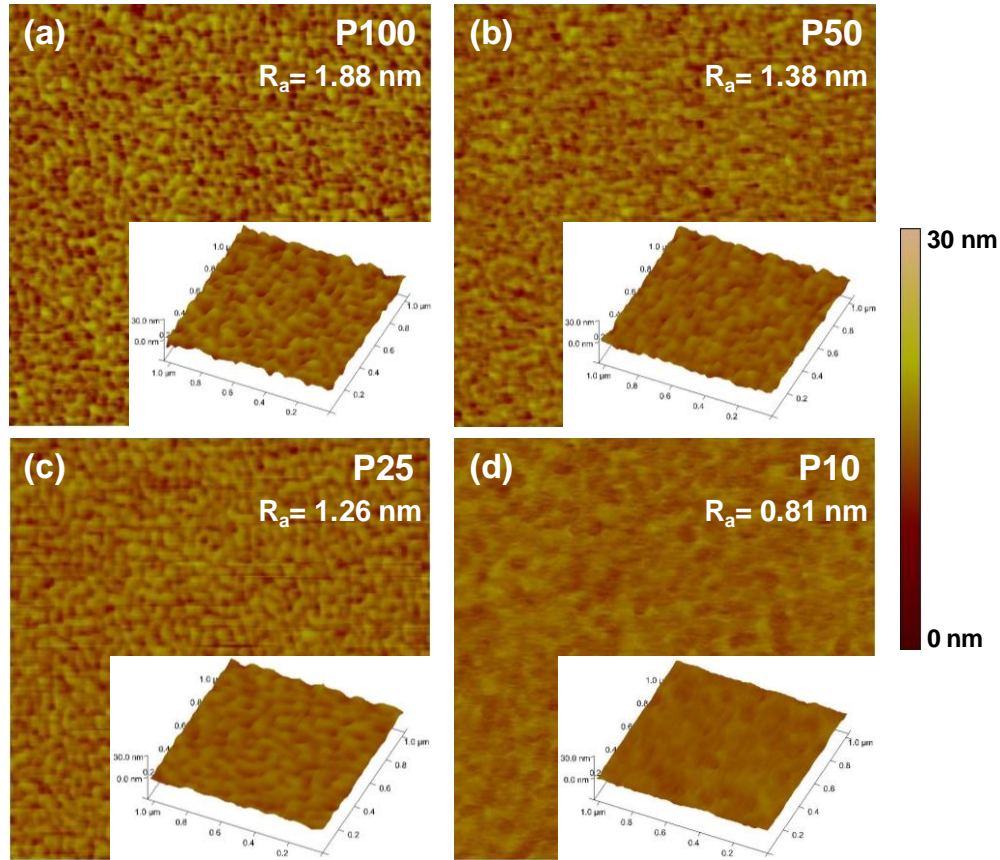


Figure 3.2. Atomic force microscopy (AFM) topography images, of $3 \mu\text{m} \times 3 \mu\text{m} \times 30$ nm Z-scale of PZT films with thickness: a) 100 nm, b) 50 nm, c) 25 nm, and d) 10 nm, deposited on LSMO(60 nm)/LSAT. Insets show the 3D topography images area of $1 \mu\text{m} \times 1 \mu\text{m} \times 30$ nm Z-scale respectively.

them. It is clearly seen that the surface morphology of all structures is free of microcracks, pores, or holes. These observations suggest that PZT films are densely packed, smooth, and have uniform grain-size distributions. An evolution was observed in the grain size with the variation of PZT film thickness from 10 nm to 100 nm: high grain density was observed in Figure 3.2 (a)-(c) for PZT thickness from 100 nm to 25 nm; however, a notable reduction of the grains density was observed in Figure 3.2(d) for 10 nm film. The grain size, average (R_a), and root-mean-square (R_{rms}) surface roughness values obtained from AFM image for each sample have been summarized in Table 3.1. Insets in Figure 3.2 show the three-dimensional (3D) AFM images on a $1 \times 1 \mu\text{m}^2$ area and 30 nm in z-scale for all structures, they show the morphologies of the P100, P50 and P25 samples do not vary significantly with the film thickness except for an increase in the height and size of the grains. Average surface roughnesses (R_a) were very low for all structures, less than 2 nm. A slight variation in the (R_a) from 1.26 nm (P25) to 1.88 nm (P100) was observed due to the increase in PZT thickness, $R_a = 0.81$ nm was obtained for P10, similar behavior was observed in R_{rms} values. 3D AFM images show a clear evolution of the height of the grains. Round grains were observed for thinner films

Table 3.1. Grain size, average (R_a) and root mean square (R_{rms}) surface roughness obtained from atomic force microscope images for different thickness of the PZT layer deposited on deposited on LSMO(60 nm)/LSAT .

PZT film Thickness (nm)	Grain size (nm)	R_a (nm)	R_{rms} (nm)
100	94	1.88	2.39
50	81	1.38	1.76
25	73	1.26	1.49
10	52	0.81	0.99

(P10, P25), while a more hillocks-like shapes were obtained for thicker films (P50, P100). The mean in-plane diameter of the grains increased with film thickness from 52

nm (P10) to 94 nm (P100) (Table 3.1). The change in grain size with thickness may be due to following: i) small grains can coalesce into the larger grains as the thickness of the PZT increases, and ii) high stress developed in the film due to the lattice mismatch between film and substrate [28-30]. Fu et al. [31] have reported that the stress was increased from 1.3 to 2.6 GPa when the film thickness decreased from 400 to 50 nm on PbTiO₃ thin film deposited on Pt/Ti/SiO₂/Si, this effect was more marked in case of thickness below 200 nm. An increase in the compressive stress was observed in our system from the XRD data. In the next section we will discuss the effect of the grain size and film thickness on the electrical and ferroelectrical properties of the PZT film.

3.4. DIELECTRIC CHARACTERIZATION

3.4.1 Dielectric properties

Pt/PZT/LSMO thin film capacitors have been prepared in an MIM sandwich structure, and the dielectric properties were measured at a 100 mV oscillator level. Figure 3.3 (a)-(b) illustrate the frequency dependence of dielectric permittivity (real (ϵ') and imaginary (ϵ'')) for different PZT/LSMO bilayer structures at room temperature. The ϵ' and ϵ'' responses for all films have similar characteristics: i) weak frequency dependence below 10⁵ Hz; ii) relatively high ϵ' and low ϵ'' values below 10⁵ Hz; and iii) large ϵ'' dispersion above 10⁵ Hz accompanied by a significant reduction in ϵ' value. There are several factors responsible for the dielectric dispersion: 1) the extrinsic sources can be attributed to the additional capacitance arising from the grain boundary and interfaces

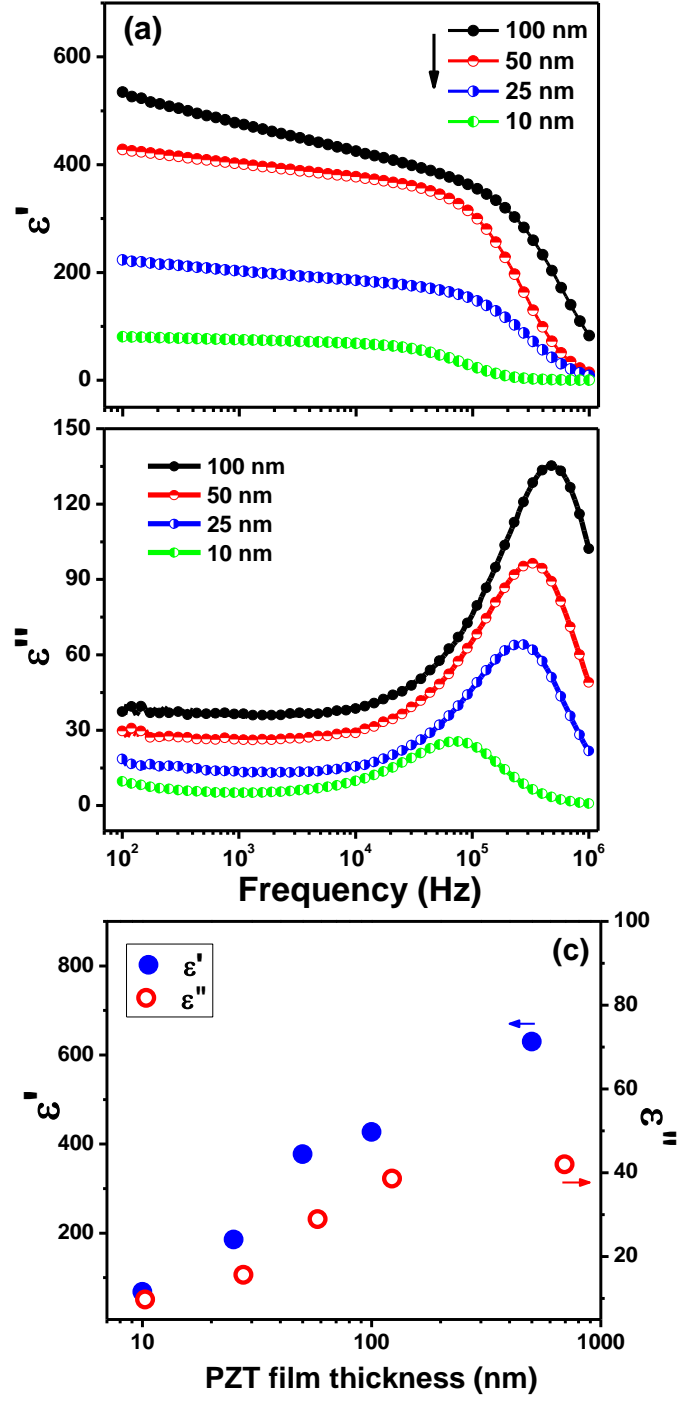


Figure 3.3. Frequency dependence of the (a) real part (ϵ') (b) imaginary part (ϵ'') of dielectric permittivity and (c) thickness dependence of ϵ' for PZT/LSMO bilayer structures with different thickness of PZT.

between layers as a consequence of the contribution of two different materials (ferroelectric-PZT and ferromagnetic-LSMO). 2) As reported by Majumdar et al. [32] the dielectric and conductive properties of LSMO are highly dependent on the strain and grain boundary configuration of the LSMO film. The ϵ' vs. frequency measurements of pure LSMO films show a similar trend compared with PZT/LSMO bilayer films; they exhibit large dielectric dispersion at higher frequencies that is more pronounced in LSMO films which have higher grain boundary population [32]. The frequency dispersion observed in PZT/LSMO bilayers can be due to the LSMO dielectric response. Figure 3.3(c) shows the evolution of the real and imaginary permittivity measured at 10 kHz as functions of PZT film thickness. The ϵ' (ϵ'') values increase from 68 (9.75) to 463 (39) when the PZT thickness increases from 10 nm to 100 nm. This increase in ϵ' and ϵ'' with thickness can be due to the dependence of the intrinsic (lattice contributions) and extrinsic contributions (domain wall motion) to the dielectric properties in the ferroelectric thin films [28, 33]; however, the saturated dielectric constant values have been reported for PZT thin films at certain thickness, typically 0.3-0.6 μm [28, 34, 35]. Perez de la Cruz et al. [33] pointed-out that the film orientation, grain size and mechanical stress from substrate clamping can be the parameters that modified the dielectric intrinsic properties, while extrinsic properties can be associate with the existence of the interfacial layer between ferroelectric films and bottom electrode. Fujisawa et al. [29, 34] observed an increase in the grain size from 60 nm to 400 nm when the thickness varied from 70 nm to 600 nm; however, grain size effects on dielectric properties were observed for PZT having thickness below 200 nm. Since the maximum PZT thickness in our system is 100 nm, grain size and mechanical stress

between LSMO/LSAT and PZT can be the intrinsic effects responsible for the variation of dielectric properties. Another source that can contribute in the variation observed in ϵ' and ϵ'' is the interfacial layer mentioned above, which act as a pinning center affecting the domain wall mobility; however, this effect is minor when the thickness of ferroelectric film increases.

3.4.2 Dielectric permittivity properties

Figure 3.4 (a) shows the temperature-dependent dielectric permittivity of the real and imaginary part (inset in each figure) of PZT for different film thickness. It shows the following features: i) notable frequency dispersion (however this effect decreases with decrease in PZT thickness); ii) a reduction of dielectric permittivity values with increasing frequency; iii) an anomaly in the range of 350-500 K. As we have discussed before, the i) and ii) can be attributed to extrinsic source like grain boundary and interfacial layers between PZT and LSMO which can generate additional capacitance. The anomaly mentioned in point iii) can be related to the ferromagnetic-metal (FM) to paramagnetic-insulator (PI) transition ($T_{\text{FM-PI}}$) of the LSMO. Ovysyannikov et al. [36] have reported the $T_{\text{FM-PI}}$ (Curie temperature) value of LSMO thin films grown on LSAT substrate is ~ 336 K, although the dielectric anomaly observed in PZT/LSMO structures is narrower when the thickness of PZT layer decreases. Dussan et al. [37] have reported similar temperature dependent dielectric behavior in PZT (550 nm)/LSMO (200 nm) heterostructures; however, this anomaly for thick PZT layer are weak in the 1 kHz to 50 kHz frequency range, we observed this anomaly is more significant in this frequency range when the thickness of PZT is reduced to 100 to 10 nm. Temperature-dependent

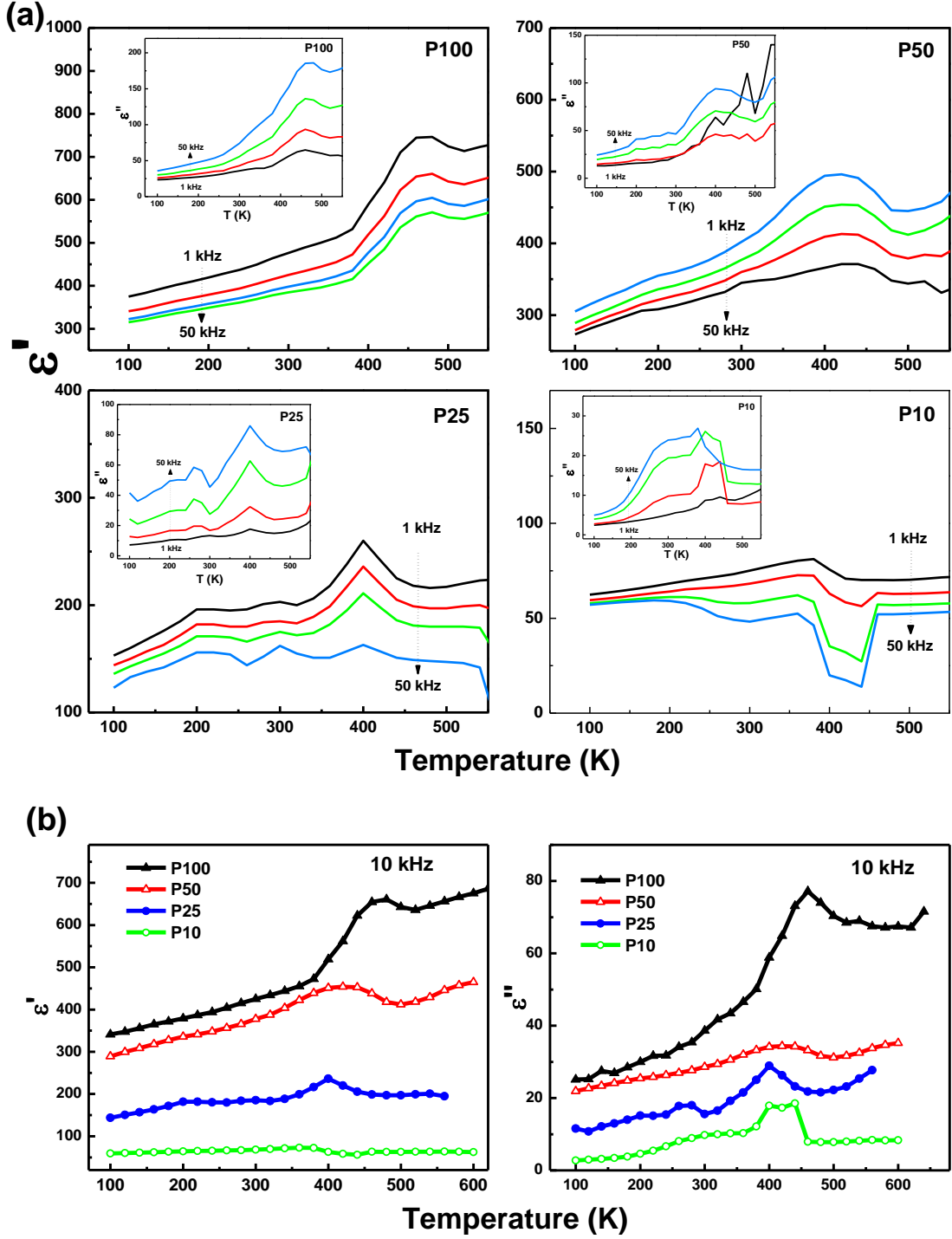


Figure 3.4. (a) Temperature dependence relative permittivity complex plane plot (ϵ'' vs. ϵ') for PZT/LSMO/LSAT structures for different thickness of PZT film. (b) Comparison of ϵ'' vs. ϵ' plots for different thickness of PZT at various temperatures.

resistivity ($\rho(T)$) measurement of the LSMO on different substrates including LSAT [36] shows a similar trend to the temperature-dependent dielectric properties of PZT/LSMO heterostructures as the LSMO, which also forms the bottom electrode the resistivity or conductivity behavior of LSMO can influence the behavior of dielectric PZT layer. Strbik et al. [38] propose that resistivity $\rho(T)$ for LSMO for $T \leq 220$ K, follows a $\sim T^2$ dependence, whereas for $220 \text{ K} \leq T \leq 355 \text{ K}$, it follows a power-series equation $\rho = \rho_0 + \rho_2 T^2 + \rho_N(T-T_0)^N$ with $4.5 \leq N \leq 5$. Electron-magnon and electron-phonon interactions were assigned as responsible for this rapid increase in resistivity. In the temperature range $335 \text{ K} \leq T \leq 420 \text{ K}$ LSMO undergoes a $T_{\text{FM-PI}}$ transition; in this temperature range the scattering is stronger via polaron conductivity and $\rho(T)$ does not follow polynomial power law formula. For $T \geq 420 \text{ K}$ the resistivity is described by small polaron hopping theory ($\rho = \rho_h T \exp(E_h/K_B T)$), where E_h is the hopping energy; K_B the Boltzmann constant; and ρ_h the resistivity coefficient. Figure 3.4(b) shows the temperature dependent dielectric permittivity (ϵ' and ϵ'') of PZT/LSMO structures for different thickness of PZT. We observed an increase in temperature of the dielectric peak when the thickness of PZT increases from 10 nm P(10) to 100 nm (P100). This effect will be discussed in the next section in the light of changes in LSMO magnetization with the variation of PZT layer thickness.

3.4.3 Dielectric Spectroscopy

Figure 3.5(a) shows the Cole-Cole plot over frequency range from 100 Hz to 1 MHz for various PZT thicknesses (10 nm to 100 nm) at selected temperatures. The pattern of the permittivity spectra is characterized by the presence of one semicircle arc at

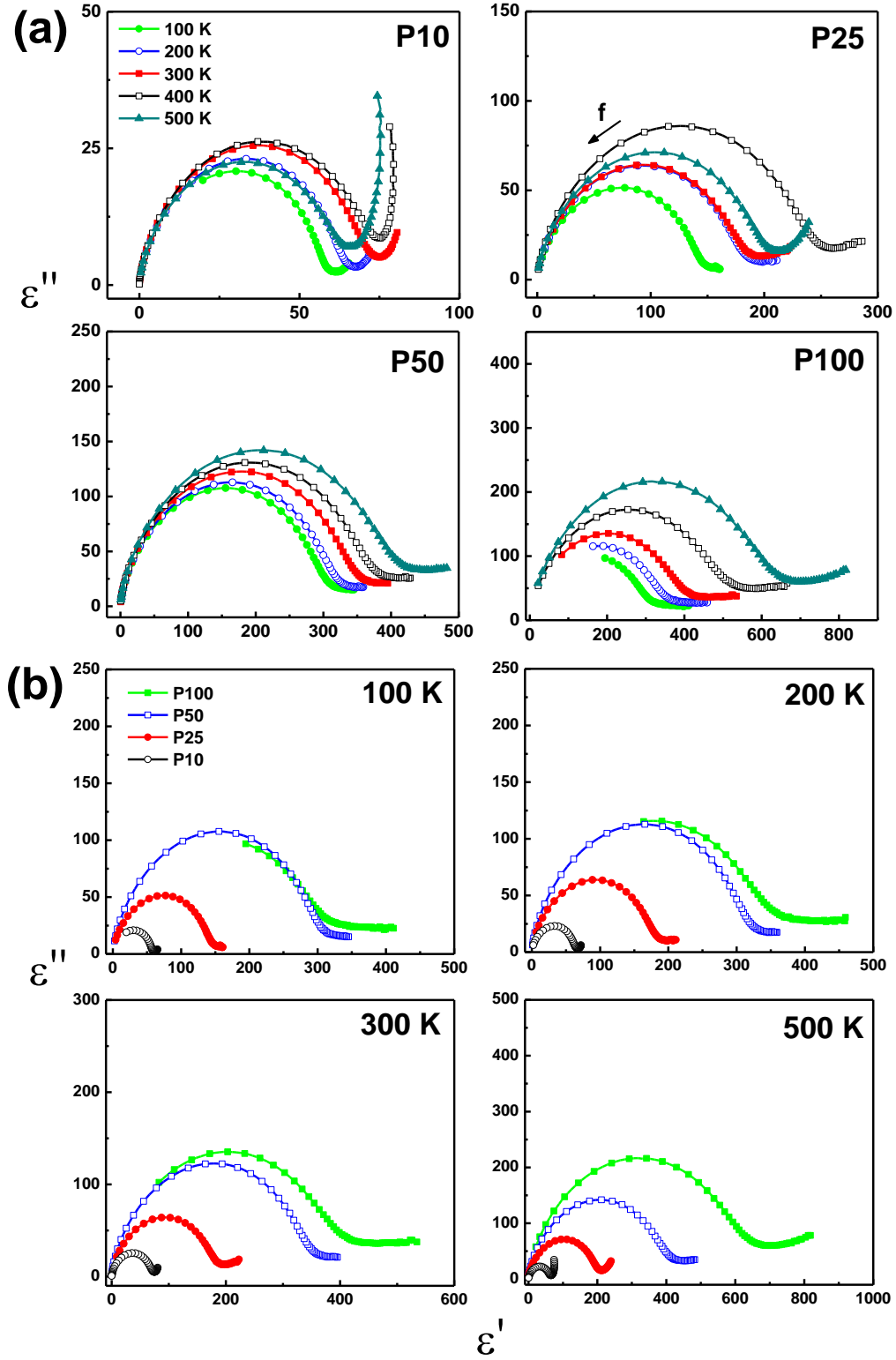


Figure 3.5. Temperature dependent (a) real and (b) imaginary dielectric permittivity for PZT/LSMO/LSAT structures for different thickness of PZT film.

high frequencies ($> 1-10$ kHz), which indicates almost bulk permittivity contribution below 400 K. A signature of other semicircles is present above 400 K and at low frequencies ($<1-10$ kHz); however, this effect is more clearly seen when thickness of PZT is reduced. A rapid increase of ϵ'' was observed above 300 K and about 1-5 kHz for sample P10, an effect that may be due to extrinsic sources such as interface effects between dielectric layer and electrode. The ϵ' radius of the semicircular arc shows significant variation with temperature for thickness of PZT higher than 25 nm, but much less variation was observed for 10 nm PZT sample. Since the intercept of the semicircular arc gives an estimation of sample resistance, this indicates for ultrathin films the resistance changes only slightly with temperature. The radius of Cole-Cole plots decreases when the temperature increases from 400 K to 500 K for thinner films (P10 and P25), but not in thicker film (P50 and P100). A possible reason is the effect of ferromagnetic-metal to paramagnetic-insulator transition in LSMO is more marked when the thickness of PZT is ultrathin. For comparison, Figure 3.5(b) presents the ϵ' vs. ϵ'' response of the PZT/LSMO structures with different PZT thicknesses for 100 K, 200 K, 300 K and 500 K. At low temperatures no significant difference was observed for thicker samples (P50, P100). With increasing of temperature the bulk permittivity contribution (ϵ' radius, when $\epsilon'' = 0$) in Cole-Cole plot increases with PZT: at 500 K a ϵ' radius was 65, 208, 429, and 670 for P10, P25, P50 and P100 respectively. Also at low frequency, the evolution of second arc is more significant for thinner samples compared with thicker PZT films.

3.5. FERROELECTRIC PROPERTIES

Figure 3.6(a) shows the evolution of the polarization versus electric field (P-E) hysteresis loops for different applied voltage at room temperature for P25 film. A well-defined loop was observed with an increase in remnant polarization (P_r) and coercive field (E_c) with increasing of voltage. A saturated loop was obtained at an applied voltage above 4 V (1600 kV/cm). Figure 3.6(b) presents P-E hysteresis loops at 300 K for different thickness of PZT (P10, P25, P50, P100) using Pt top electrodes. It was observed that with increase in the PZT thickness that: i) an improvement occurs in symmetry and saturation of the P-E loop; ii) a slightly reduction in P_r value was observed for thicker PZT films (> 25 nm) while an appreciable P_r reduction was obtained for PZT film with thickness of 10 nm; iii) a reduction in the P-E loop gap; iv) a reduction in the coercive field, i.e. $\sim 170, 390, 420$ and 1300 kV/cm for P100, P50, P25 and P10, respectively. The higher P_r values in P100, P50 and P25 could be attributed to the larger tetragonal distortion and the in-plane epitaxial strain of the PZT unit cell, as observed from the XRD. Previous works for both polycrystalline and epitaxial PZT films [37, 39-41] reported P_r values vary from 15 to $54 \mu\text{C}/\text{cm}^2$ for PLD grown PZT films with one of the highest P_r values reported as $\sim 70 \mu\text{C}/\text{cm}^2$ for PLD-grown PZT films, but requiring ex-situ post annealing at 750°C in air by rapid thermal annealing (RTA) techniques [42].

The values of P_r and E_c of the thin film structures were in the range of 24 - $42 \mu\text{C}/\text{cm}^2$ and 169 - 1945 kV/cm under a maximum applied voltage of 5 V. The drastic decrease of P_r and increase of E_c when the thickness of PZT is reduced to few nm level (10 nm) can be explained by the effect of the passive layer (also called low dielectric or dead layer) originating at the ferroelectric-electrode interface [43, 44]. A decrease in P_r

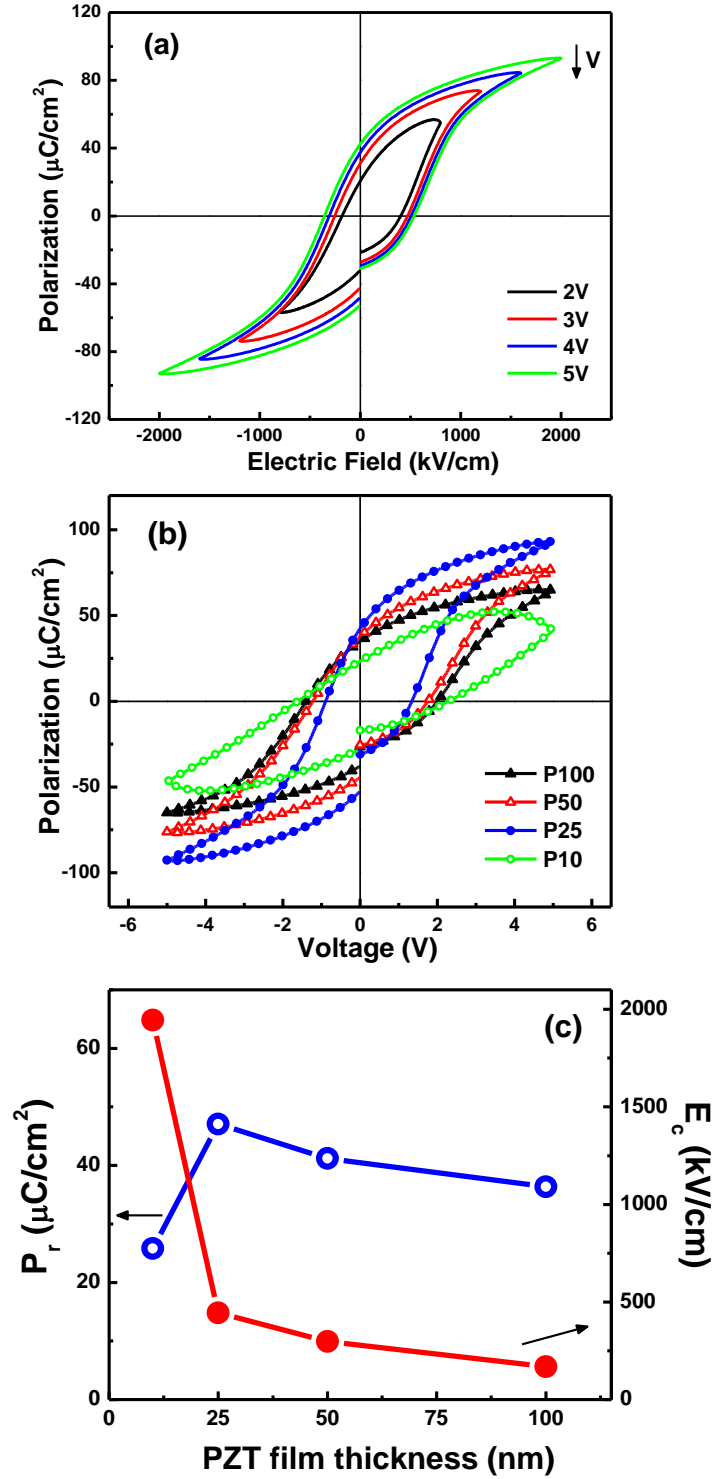


Figure 3.6. Room temperature ferroelectric hysteresis loops for: (a) P25 heterostructure thin film at different voltages at 2 kHz. (b) PZT/LSMO/LSAT structures for different thickness of PZT film (from 100 nm to 10 nm) at 5 V and 2 kHz. (c) PZT film thickness dependence of the remanent polarization (P_r) and electric coercive field (E_c).

and increase in E_c has been observed by other research when the thickness of PZT ranging between 100 nm to 4 μm [28, 33, 45]. As the thickness of PZT layer decreases at this very thin level, the role of the passive layer is more important: due to the drop of the potential across of the passive layer, a higher voltage is needed across the capacitor to switch bare ferroelectric layers. For this reason, it is expecting E_c increase, when the thickness of the ferroelectric layer increases, the effect of a passive layer is diminished, with an enhancement in both domains wall mobility and switching with the respective reduction of the E_c value [28].

The relation between the relative dielectric constant and the PZT film thickness could be explained by a model which introduces a low dielectric constant thin layer in series with a normal PZT layer [45]. The importance of the low dielectric constant layer in ultrathin ferroelectric films is also supported by dielectric data in which an increase of the ϵ'' radius at $\epsilon'' = 0$ in Cole-Cole plot (Figure 4(a)) is increasing with PZT thickness. The intercept of the semicircular arc with the real axis gives an estimation of sample resistance. Another factor which contributes to the electrical properties with different film thickness is the degree of crystallinity of PZT which is intensified with the increase in film thickness, as can be seen in XRD results (Figure 3.1 (b), (c) and (d)). The dipole moment in each domain increases because of the high crystallinity in the PZT thick film, leading to the enhancement of domain switching and resulting in higher polarization [46, 47].

3.6. MAGNETIC PROPERTIES

The magnetization versus magnetic field (M-H) hysteresis loops of PZT/LSMO hetero-structures at 300 K show ferromagnetic behavior in all samples. Since the

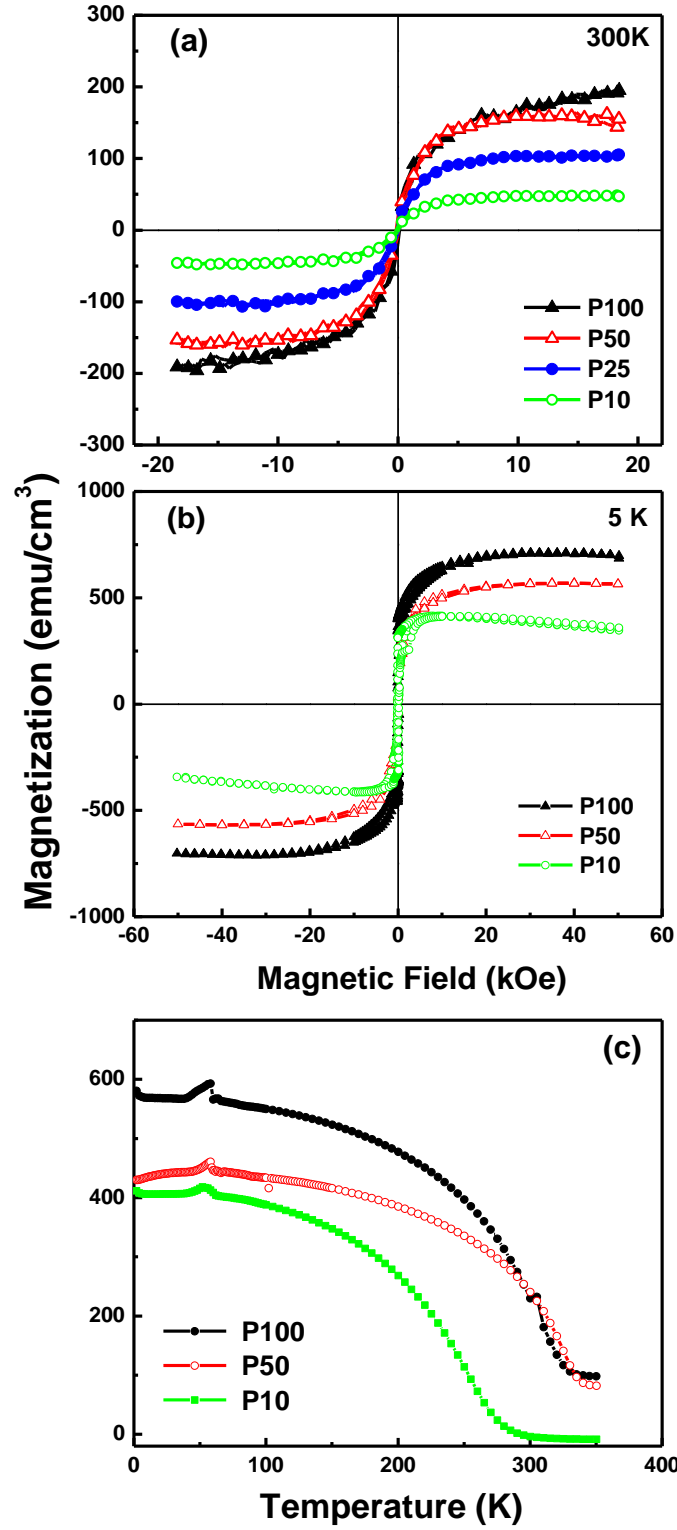


Figure 3.7. Ferromagnetic hysteresis loop at (a) 300 K, (b) 5 K and temperature dependent magnetization for PZT/LSMO/LSAT structures for different thickness of PZT film (from 100 nm to 10 nm).

thickness of LSMO layer was kept constant in all the films, the magnetization values were only normalized to the volume of the LSMO layer assuming no magnetic contribution from the PZT layer. Appreciable decrease of saturated magnetization (M_s) was observed with decrease of PZT layer thickness (Figure 7 (a) and (b)). The average M_s values were 195, 160, 106 and 50 emu/cm^3 for 100, 50, 25, and 10 nm, respectively at room temperature, similar behavior was observed in M-H curves measured at low temperature 5 K. Curie temperature $T_c \sim 335$ K was observed for the thicker samples P100 and P50, whereas, a significant decrease of T_c value ($T_c \sim 290$) was obtained for thinner sample (P10) (Magnetization versus temperature (M-T) curves). Similar trend of T_c was observed in the temperature-dependent dielectric anomaly (see Figure 4(b)). An Analogous behavior was observed by Jiang et al. [19] in ultrathin LSMO films capping with $\text{Pb}(\text{Zr}_{0.2}\text{Ti}_{0.8})\text{O}_3$ ferroelectric layer. They found an increase in both T_c (from 200 K to 250 K), and M_s (from 2.06 to 3.71 μ_B/Mn), and a decrease in resistivity of about four order of magnitude, compared with pure LSMO thin film. However, a weak effect on LSMO properties was observed when the capping layer is a non-ferroelectric material such as SrTiO_3 and LaAlO_3 . They attributed this effect due to PZT/LSMO interface effect: i) ferroelectric polarization of PZT increases the hole density at the interface changing the conductivity of LSMO layer, ii) the hole accumulation enhance the population/size of the FM- phase domains. The observed decreased of the T_c value with reduction of PZT thickness support the idea of decrease of FM phase domains at the PZT/LSMO interface in heterostructures with thinner ferroelectric layers. Similar behavior was also observed by Sim et al. [48] in bilayer multiferroic CoFe_2O_4 (CFO) /PZT thin films.

REFERENCES

1. K. Dörr and C. Thiele, *Phys. Status Solidi B*. **243**, 21 (2006).
2. R. Ramesh and N. A. Spaldin, *Nat. Mater.* **6**, 21 (2007).
3. W. Eerenstein, N. D. Mathur, and J. F. Scott, *Nature (London)* **442**, 759(2006).
4. M. Bibes and A. Barthélémy, *Nature Mater.* **7**, 425 (2008).
5. G. Kim, D. Mazumdar and A. Gupta, *Appl. Phys. Lett.* **102**, 052908 (2013).
6. D. Pantel, S. Goetze, D. Hesse and M. Alexe, *Nature Materials* **11**, 289 (2012)
7. Y. W. Yin, M. Raju, W. J. Hu, X. J. Weng, X. G. Li, and Q. Li, *J. Appl. Phys.* **109**, 07D915 (2011).
8. V. Garcia, M. Bibes, L. Bocher, S. Valencia, F. Kronast, A. Crassous, X. Moya, S. Enouz-Vedrenne, A. Gloter, D. Imhoff, C. Deranlot, N. D. Mathur, S. Fusil, K. Bouzehouane, A. Barthélémy, *Science* **327**, 1106 (2010).
9. A. Gruverman, D. Wu, H. Lu, Y. Wang, H. W. Jang, C. M. Folkman, M. Ye. Zhuravlev, D. Felker, M. Rzechowski, C.-B. Eom, and E. Y. Tsybal, *Nano Lett.* **9**, 3539 (2009).
10. Zener C, *Phys. Rev.* **81**, 440 (1951).
11. J. Heremans, *J. Phys. D.* **26**, 1149 (1993).
12. S. Jin, M. McCormack, T. H. Tiefel, and R. Ramesh, *J. Appl. Phys.* **76**, 6929 (1994).
13. J. Fontcuberta, B. Martinez, A. Seffer, S. Pinol, J. L. Garcia-Munoz, and X. Obaradors, *Phys. Rev. Lett.* **76**, 1122 (1996).
14. J.-Q. Wang, R. C. Barker, G.-J. Cui, T. Tamagawa, and B. L. Halperm, *Appl. Phys. Lett.* **71**, 3418 (1997).
15. S. Brivio, M. Cantoni, D. Petti, A. Cattoni, R. Bertacco, M. Finazzi, F. Ciccacci, A. Sidorenko, G. Allodi, M. Ghidini, R. de Renzi, *Mater. Sci. and Eng. B.* **144**, 93 (2007).
16. P. W. M. Blom, R. M. Wolf, J. F. M. Cillessen, and M. P. C. M. Krijn, *Phys. Rev. Lett.* **73**, 2107 (1994).
17. A. Q. Jiang, C. Wang, K. J. Jin, X. B. Liu, J. F. Scott, Ch. S. Hwang, T. A. Tang, H. B. Lu, and G. Z. Yang, *Adv. Mater.* **23**, 1277 (2011).

18. R. Scherwitzl, P. Zubko, I. Gutierrez Lezama, Sh. Ono, A. F. Morpurgo, G. Catalan, and J.M. Triscone, *Adv. Mater.* **22**, 5517 (2010).
19. L. Jiang, W. S. Choi, H. Jeon, T. Egami, and H. N. Lee, *Appl. Phys. Lett.* **101**, 042902 (2012).
20. A. Plecenik, K. Fröhlich, J. P. Espinós, J. P. Holgado, A. Halabica, M. Pripko, and A. Gilabert, *Appl. Phys. Lett.* **81**, 859 (2002).
21. R. Bertacco, S. Brivio, M. Cantoni, A. Cattoni, D. Pett, M. Finazzi, F. Ciccacci, A. A. Sidorenko, M. Ghidini, G. Allodi, and R. De Renzi, *Appl. Phys. Lett.* **91**, 102506 (2007).
22. E. Liu, J.Z. Zhang, W. Zhang, PK.J. Wong, L.Y.Lv, Y. Zhai, J. Wu, Y.B. Xu, *J. Appl. Phys.* **109**, 07C121 (2011).
23. S. Stadler, Y. U. Idzerda, Z. Chen, S. B. Ogale, and T. Venkatesan, *J. Appl. Phys.* **87**, 6767 (2000).
24. S. Ki and J. Dho, *J. Korean Phys. Soc.* **57**, 1879 (2010).
25. E. Sawaguchi, *J. Phys. Soc. Jpn.* **8**, 615 (1953).
26. T. Tybell, C. H. Ahn, J.-M. Triscone, *Appl. Phys. Lett.* **75**, 856 (1999).
27. D. M. Kim, C. B. Eom, V. Nagarajan, J. Ouyang, R. Ramesh, V. Vaithyanathan, and D. G. Schlom, *Appl. Phys. Lett.* **88**, 142904 (2006).
28. T. Haccart, E. Cattán, D. Remiens, Semiconductor Physics, *Semicond. Phys. Quantum Electron.* **5** (1) 78 (2002).
29. H. Fujisawa, S. Nakashima, K. Kaibara, M. Shimizu and H. Niu, *Jpn. J. Appl. Phys.* **38** 5392 (1999).
30. H. Okino, T. Nishikawa, M. Shimizu, T. Horiuchi and K. Matsushige, *Jpn. J. Appl. Phys.* **38** 5388 (1999).
31. D. Fu, T. Ogawa, H. Suzuki, and K. Ishikawa, *Appl. Phys. Lett.* **77**, 1532 (2000).
32. S. Majumdar, H. Huhtinen, P. Paturi, H. S. Majumdar, *J. Mater. Science* **48**, 2115 (2013).
33. J. Pérez de la Cruz, E. Joanni, P. M. Vilarinho, and A. L. Kholkin, *J. Appl. Phys.* **108**, 114106 (2010).
34. H. Fijisawa, S. Nakashima, M. Shimizu and H. Niu, Proc. Od the 11th Int. Symp. On Applicattions of Ferroelectrics (ISAF), 77 (1998)

35. C-R Cho, W-J Lee, B-G Yu, and B-W Kim, *J. Appl. Phys.* **86**, 2700 (1999).
36. G. A. Ovsyannikov, A. M. Petrzhik, I. V. Borisenko, A. A. Klimov, Yu. A. Ignatov, V. V. Demidov, and S. A. Nikitov, *J. Exp. Theor. Phys.* **108**, 48 (2009).
37. S. Dussan, A. Kumar, J. F. Scott, and R. S. Katiyar, *Appl. Phys. Lett.* **96**, 072904 (2010).
38. V. Štrbík and Š. Chromik, *Journal of Electrical Engineering*, **63**, 270 (2012).
39. C. A. F. Vaz, Y. Segal, J. Hoffman, F. J. Walker, and C. H. Ahn, *J. Vac. Sci. Technol. B.* **28**(4), C5A6 (2010).
40. Z. J. Wang, H. Usuki, T. Kumagai, and H. Kokawa, *J. Sol-Gel Sci. Technol.* **42**, 375 (2007).
41. J. Schwarzkopf and R. Foranari, *Prog. Cryst. Growth Charact. Mater.* **52**, 159 (2006).
42. W. Wu, K. H. Wong, C. L. Choy, and Y. H. Zhang, *Appl. Phys. Lett.* **77**, 3441 (2000).
43. A. K. Tagantsev, M. Landivar, E. Colla, and N. Setter, *J. Appl. Phys.* **78**, 2623 (1995).
44. Alexander K. Tagantsev, L. Eric. Cross, Jan Fousek, Publisher Springer New York (2010). DOI10.1007/978-1-4419-1417-0, ISBN 978-1-4419-1416-3
45. L. Ran, J. Gen-Shan, L. Bin, Z. Quan-Liang, Z. De-Qing, Y. Jie, C. Mao-Sheng, *Chin. Phys. Lett.* **29**, 058101 (2012).
46. J. K. Yang, W. S. Kim, and H. H. Park, *Appl. Surf. Sci.* **169-170**, 544 (2001).
47. C. A. Randall, N. Kim, J. P. Kucera, W. Cao, and T. R. Shrout, *J. Am. Ceram. Soc.* **81**, 677 (1998).
48. C. H. Sim, A. Z. Z. Pan, and J. Wang, *J. Appl. Phys.* **103**, 124109 (2008).

CHAPTER 4

FERROELECTRIC TUNNEL JUNCTION

4.1. INTRODUCTION

Typical ferroelectric tunnel junctions (FTJs) consist of a few unit cells of a ferroelectric (polar) material sandwiched between two electrodes where interplay of ferroelectricity and electron tunneling occurs [1-6]. This is possible since ferroelectricity can be retained in perovskite oxides films with thickness of the order of a few nanometers. Realization of this idea is a task with many obstacles, because it requires fabrication of ultrathin films retaining pronounced ferroelectric properties at a thickness of only a few unit cells, however recent progress in epitaxy of complex oxides [7,8], ultrathin films of ferroelectric polymers [9], advancement in nanoscale characterization techniques, and theoretical advances have made the realization of FTJs possible. For these reasons many different experimental and theoretical [10-12] studies have been reported in the past decade.

A ferroelectric polarization in a tunnel barrier leads to a change in resistance of the junction, a phenomenon known as the tunneling electroresistance (TER) effect, associated with polarization switching of the ferroelectric barrier layer [6,10]. The TER is of purely electronic origin and involves changes in the density of states at the interfaces (barrier/electrode) following polarization reversal and a resulting asymmetric potential

profile across the FTJs [4,5,13]. FTJs have attracted interest both for the basic physics which is involved in controlling their properties and for their potential applications in nanoelectronics and data storage [14-17]. In the last few years a significant number of works have been reported TER effects in FTJs based on different polar systems, such as $\text{Pb}(\text{Zr,Ti})\text{O}_3$ [18-20], BaTiO_3 [21-24], BiFeO_3 [25], and $(\text{Ba,Sr})\text{TiO}_3$ [26]. Maksymovych et al [18]. have reported a highly reproducible control of local electron transport in thick PZT (30 nm) via its spontaneous polarization at low temperature. Electrons were injected from the tip of an atomic force microscope into a ferroelectric PZT thin film in the regime of high field-assisted electron tunneling (Fowler-Nordheim tunneling). The tunneling current showed a pronounced hysteresis with abrupt switching events that coincided, within experimental resolution, with the local switching of ferroelectric polarization. The huge spontaneous polarization of the PZT film resulted in 100-fold amplification of the tunneling current upon ferroelectric switching. The magnitude of the result was subjected to electrostatic control via ferroelectric switching. Pantel et al [19]. also showed that ferroelectric polarization direction and resistance state are correlated in epitaxial ferroelectric $\text{Pb}(\text{Zr}_{0.2}\text{Ti}_{0.8})\text{O}_3$ nanoscale capacitors. These nanoscale capacitors showed a high resistance ratio, up to 1500:1, as well as high switching current densities of about 10 A/cm^2 , sufficient for resistive readout. Recently Chen et al [20]. showed that the preferential orientation of polarization in as-grown PZT ultrathin layers can be manipulated by choosing an appropriate type of bottom electrode material, i.e. PZT films deposited on SrRuO_3 or $(\text{La,Sr})\text{CoO}_3$ electrodes exhibit preferential upward or downward polarization.

4.2. EXPERIMENTAL DETAILS

4.2.1 PZT and LSMO bilayer ultrathin films grown by pulsed laser deposition.

The oxide PZT/LSMO heterostructure films were synthesized on $(\text{LaAlO}_3)_{0.3}(\text{Sr}_2\text{AlTaO}_6)_{0.7}$ (LSAT) (001)-oriented substrates, using a multi-target pulsed laser deposition (PLD) system equipped with a KrF excimer laser ($\lambda=248$ nm). The PZT and LSMO were grown at 600 °C and 700 °C respectively, under an oxygen pressure of ~80 mTorr, using a laser energy density of ~1-2 J/cm² and deposition frequency of 1 Hz, followed by annealing at 700 °C for 30 min in oxygen at a pressure of ~320 Torr. The films were cooled down to room temperature at a rate of 5°/min. The thickness of the PZT was controlled to 7, 5, or 3 nm for each heterostructure films, whereas the thickness of the LSMO layer was kept constant (~30 nm) in all films. The thickness of the films was precisely maintained by controlling the number of laser shots. These heterostructure films will be identified in the manuscript and figures as P7, P5, and P3 for 7-, 5-, and 3-nm thickness. An in-situ reflection high-energy electron diffraction (RHEED) system operating at 21 keV beam energy, 1.4 A filament current and with an incident angle of 1° to 4° was employed to monitor the growth of the heterostructure films.

4.2.2 Structural, ferroelectric, and transport experimental details.

The crystal structure of the films was characterized using X-ray diffraction (XRD) techniques (Rigaku Ultima III) with $\text{CuK}\alpha$ radiation with wavelength $\lambda = 1.5405$ Å, a step size of 0.02° and scanning speed of 1°/min. XRD patterns were recorded over the angular range $2\theta = 20^\circ$ -60°.

A multimode Nanoscope V (Veeco Instruments) was used to examine the morphology of the ultrathin films (atomic force microscopy, contact-mode AFM) and nanoscale ferroelectric properties of the PZT layers (piezoresponse force microscopy - PFM). For AFM measurements a commercial silicon nitride tip was used with back side coating (top Au/bottom Cr); whereas for PFM a phosphorous-tipped doped-Si coated with Co/Cr was used. The driving voltage was applied either on the PZT surface or on the top electrode. The electrical measurements were carried out in metal-insulator-metal (MIM) configuration with Pt top electrode. The Pt electrodes were deposited by DC sputtering on top of the heterostructure films. The junctions were patterned into a cross-strip geometry using photolithography. The junction areas were $\sim 16 \mu\text{m}^2$ and $64 \mu\text{m}^2$. The transport measurements were made with a Keithley 2400 multimeter with four-point geometry at temperatures of 80 K and 297 K. The capacitance versus voltage was measured using an SI 1260 Impedance/Gain-phase Analyzer.

4.3. STRUCTURAL CHARACTERIZATION

Figure 4.1(a) shows the XRD patterns of the three different PZT/LSMO heterostructures. In all heterostructures only the $(00l)$ ($l = 1$ and/or 2) reflections corresponding to the LSAT substrate, PZT and LSMO layers are present in the range of 20° - 60° . These observations suggest that individual PZT and LSMO phases were retained in the heterostructure films. Bulk LSAT and LSMO have a cubic perovskite structure with lattice parameter of $a_{\text{LSAT}} = 3.868 \text{ \AA}$ and $a_{\text{LSMO}} = 3.871 \text{ \AA}$ respectively, while PZT has a tetragonal perovskite structure with $a_{\text{PZT}} = 4.036 \text{ \AA}$ and $c_{\text{PZT}} = 4.146 \text{ \AA}$.

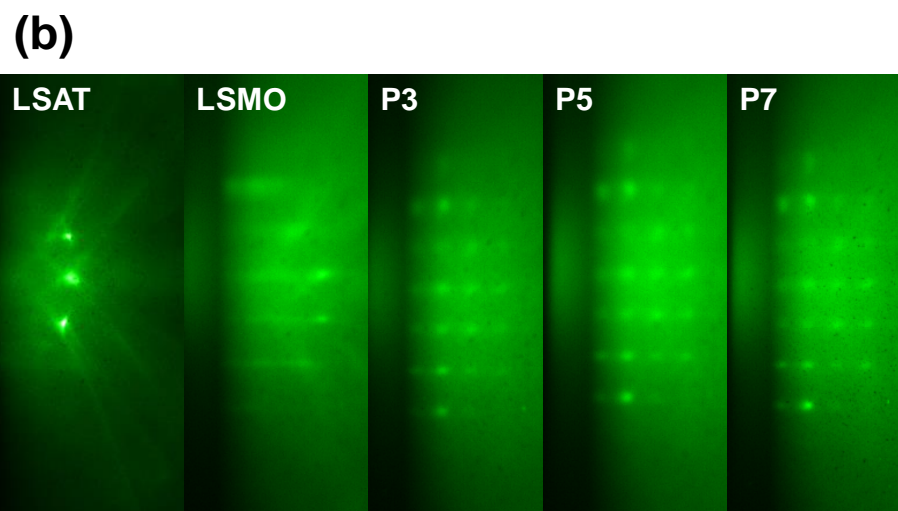
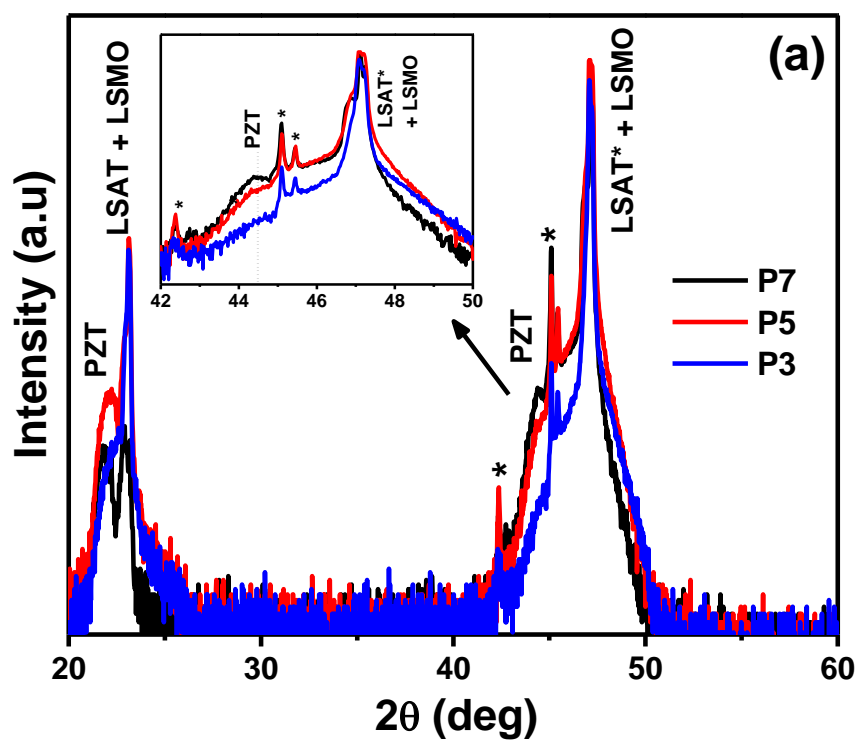


Figure 4.1. (a) XRD patterns for PZT ultra-thin films grown on LSMO (30 nm) coated LSAT (001) substrate for thickness from 3 nm (P3) to 7 nm (P7). (b) RHEED patterns of LSAT (001) substrate before deposition; and after deposition of: 30 nm of LSMO film, 3 nm (P3), 5 nm (P5) and 7 nm (P7) of ultrathin films of PZT.

Hence, LSMO on LSAT and PZT on LSMO experience an in-plane strain of -0.078% and -4.26% respectively. Due to the high compressive stress experienced by PZT, it is expected to decrease (increase) the in-plane (out-of-plane) lattice parameter. This effect is more pronounced for very thin films [27], a systematic decrease of the 2θ position from $\sim 44.65^\circ$ to $\sim 44.56^\circ$ for the (002) PZT peak was observed when the thickness was decreased from 100 nm to 10 nm [28]. Although weak PZT peaks were obtained for ultrathin films in the present study (Figure 4.1(a)), a similar decrease in 2θ was observed when the PZT thickness decreased from ~ 7 to 3 nm (see the dashed line in the inset of Figure 4.1(a)). The systematic shift of 2θ to lower angles with decrease of PZT thickness (100 nm to 3 nm) can be attributed to the different strain experienced for PZT films when its thickness decreases. The surface crystallinity of the substrates before growth and the LSMO bottom layer and ultrathin PZT films of different thicknesses were monitored by in-situ high-pressure reflection high energy electron diffraction (RHEED); and the corresponding patterns are shown in Figure 4.1(b). In case of LSAT substrates a series of clear bright diffraction spots lying on the Laue zone and Kikuchi lines can be identified, which are the signatures of well-crystallized material, smooth and atomically flat surfaces [29,30]. RHEED patterns after deposition of ~ 30 nm of LSMO show a streak-like pattern indicating a flat sample surface, with a slight increase of the roughness as compared with spectra of pure LSAT substrates. RHEED patterns of P3, P5 and P7 samples containing ~ 3 , 5, and 7 nm thick PZT layers grown on LSMO/LSAT substrates show streak-like diffraction spots indicating highly oriented monocrystalline growth, suggesting that the surface of ultrathin films became rather rougher compared with the surface of the LSMO layer.

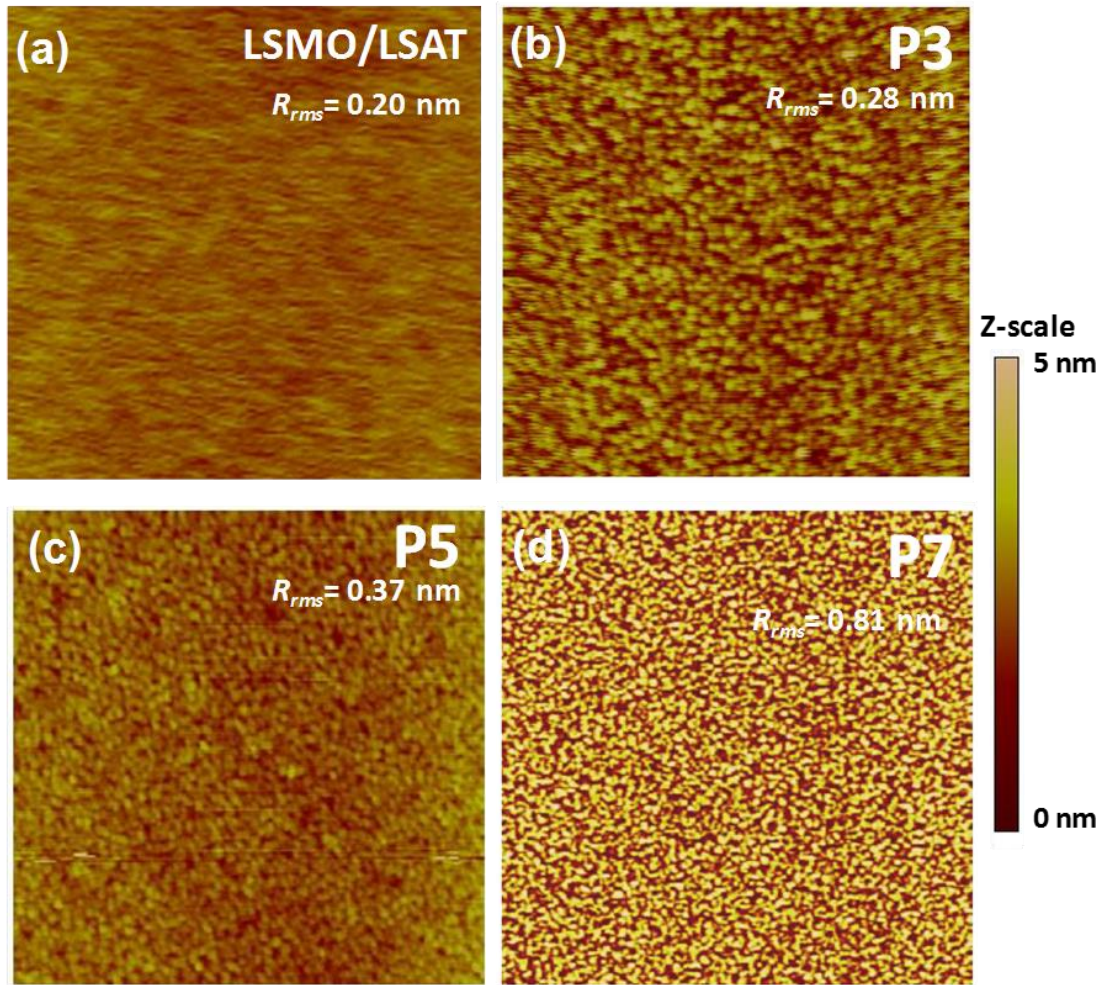


Figure 4.2. Atomic force microscopy (AFM) surface topography images, of $3 \times 3 \mu\text{m}^2$ having 5 nm in Z-scale of (a) LSMO/LSAT, PZT ultra-thin films with thickness: (b) 7 nm- P7, (c) 5 nm- P5, and (d) 3 nm- P3, deposited on LSMO(30 nm)/LSAT.

Figure 4.2(a) shows the surface morphology of bottom LSMO layer of thickness ~ 30 nm grown on an LSAT substrate. In a contact mode with scan size of $3 \times 3 \mu\text{m}^2$, it presents a flat surface without granular structure, with average (R_a), and a root-mean-square (R_{rms}) surface roughness of ~ 0.17 nm and 0.20 nm respectively. Figures 4.2(b)-(d) illustrate the morphology of the ultrathin PZT films of different thickness deposited on LSMO/LSAT substrates. The z-scale of all images was kept at constant height ~ 5 nm to facilitate comparisons among them. It is clearly seen that the surface morphology of all structures

displays a smooth and very homogeneous surface, free of microcracks, pores or holes. The R_a and R_{rms} values obtained from AFM image for PZT/LSMO samples were observed to decrease with the thickness of the PZT films (e.g. R_{rms}/R_a of 0.81/0.78 nm, 0.37/0.30 nm and 0.28/0.24 were obtained for P7, P5 and P3 respectively). The smooth surface and low roughness characteristics of the PZT ultrathin films make them suitable for FTJ applications.

4.4. FERROELECTRIC PROPERTIES

PZT ultrathin PFM measurements produced small out-of-plane vibrations that were transmitted to the piezoelectric material by an oscillating voltage applied to a conducting tip. These oscillations were identified using a lock-in amplifier, and the phase and amplitude of the signals were directly associated to the piezoelectric response of the PZT thin film kept under the tip. Figure 4.3(a) shows diagrams of the domain pattern of three different ultrathin PZT films deposited on ferromagnetic semi-metallic LSMO electrodes. A clear ferroelectric response was obtained in all ultrathin PZT films by using PFM. The polar switching was performed by scanning at a probe bias of +3 V over a 4 μm^2 area in a reversed bias -3 V scanned area, leading to the contrast change in the middle of the 1 μm^2 (bias voltage \sim -3 V) scanned area, as shown in Figure 4.3(a) for different thickness of PZT. It can also be seen from PFM images that a clear contrast in the signal is observed even for PZT films with \sim 3 nm thicknesses; however it is also observed that the signal weakens with decreasing film thickness from 7 nm to 3 nm, and this indicates that the ferroelectric character tends to diminish with decreasing film thickness. The PFM images show that the out-of-plane component of the polarization can be switched between two stable states. The polarization switching is further confirmed by

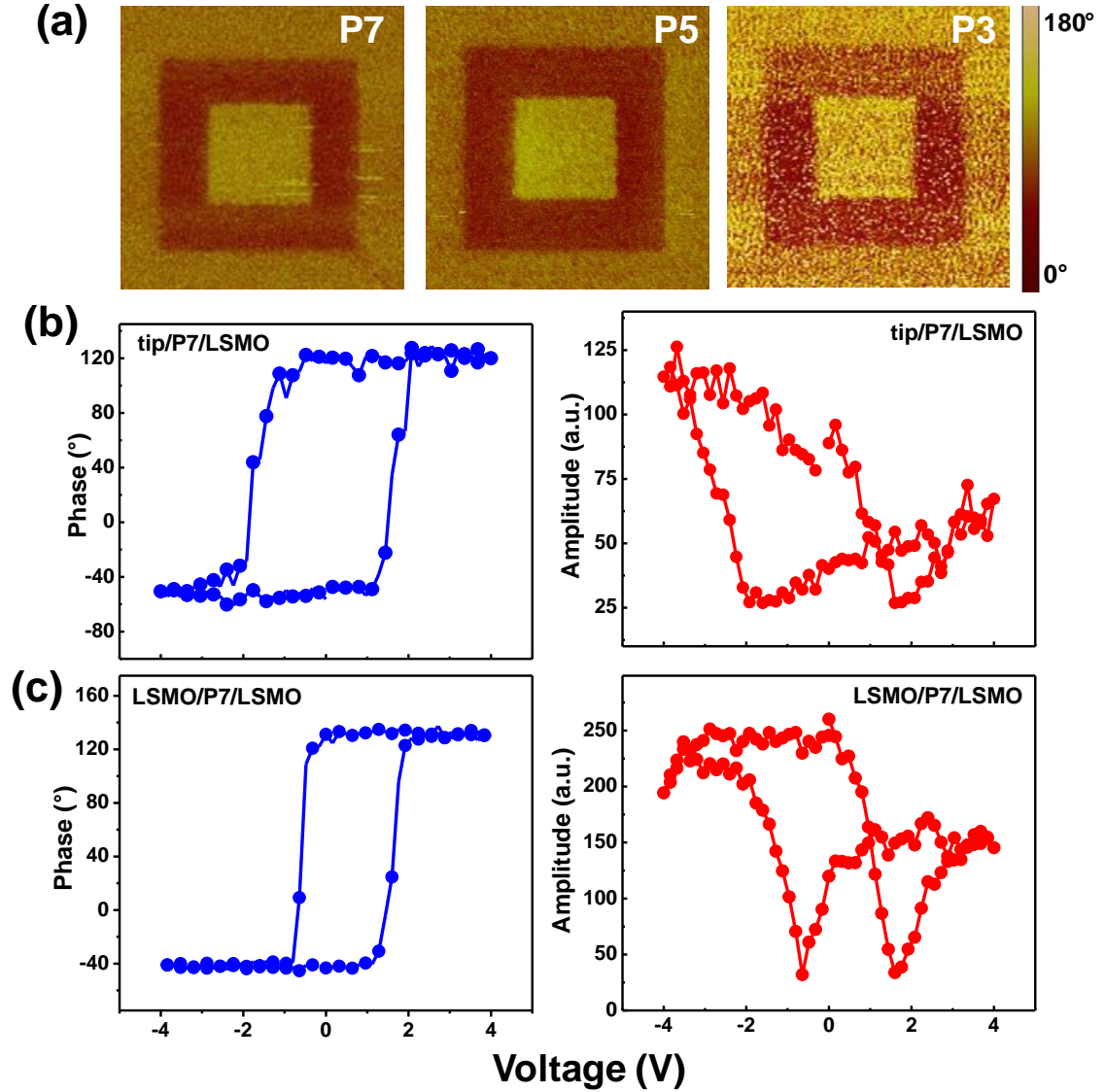


Figure 4.3. Piezoresponse force microscopy (PFM) measurements shows: (a) Polarization switching images for P7, P5, and P3 ultra-thin films. PFM phase and amplitude hysteresis loops measured in two configurations (b) Tip/P7/LSMO and (c) LSMO/P7/LSMO, where P7 represent 7 nm thick of PZT barrier.

the phase hysteresis loops in Figures 4.3(b) and (c) for two different configurations. In Figure 4.3(b) the PFM measurement for tip/P7/LSMO configuration show well-defined phase hysteresis and amplitude butterfly loops, showing that the film possesses ferroelectric character. The PFM phase changes by 180° at the coercive voltages (V_c) of -1.9 and 1.8 V; similar results were also obtained for LSMO/P7/LSMO (Figure 4.3(c))

with coercive voltages of -0.6 and 1.6 V. Similar values of V_c were reported by Pantel et al [19]. in Au/Cu/PZT/LSMO with a PZT barrier of 9 nm and by others in PbTiO₃ ultrathin ferroelectric films [31]. The hysteresis and butterfly loops in Figure 4.3(b) when the PFM tip was directly in contact with the film surface are almost symmetrical, in agreement with some reports [6,32]. On the other hand, in Figure 4.3(c) the PFM loops are asymmetrical, as observed by other authors [16,19,33]. The asymmetry behavior in the PFM hysteresis loop may arise due to following two reasons: i) different kinds of bottom and top electrodes and ii) large internal bias field in ultrathin PZT film. The former can be attributed to the difference in work function at the two film-electrode interfaces, while the latter involves a built-in electric field in the PZT. This electric field could be due to enhanced interdiffusion of chemical species at the interfaces during annealing, resulting in high enough defect dipole accumulation at the interface to polarize thin PZT layer in the vicinity of the electrodes. The self-polarized layer might lead to asymmetrical hysteresis loop. In addition Wu et al [34]. reported that oxygen-loss is associated with internal stress at the PZT/LSMO interface may be another reason responsible for the large internal electric field in epitaxial PZT films [28].

4.5. TRANSPORT PROPERTIES

Figure 4.4 show experimental conductance-voltage curves (open circles in Figure 4.4) for two different barrier thicknesses of PZT (5 and 7 nm) and at two different temperatures (80K and 297 K). The differential conductance $G(V) = dI/dV$ show a parabolic dependence on bias voltage, as can be seen in the normalized conductance $G(V)/G(0)$, where $G(0)$ is the conductance at zero bias (equation 4.1). The parabolic

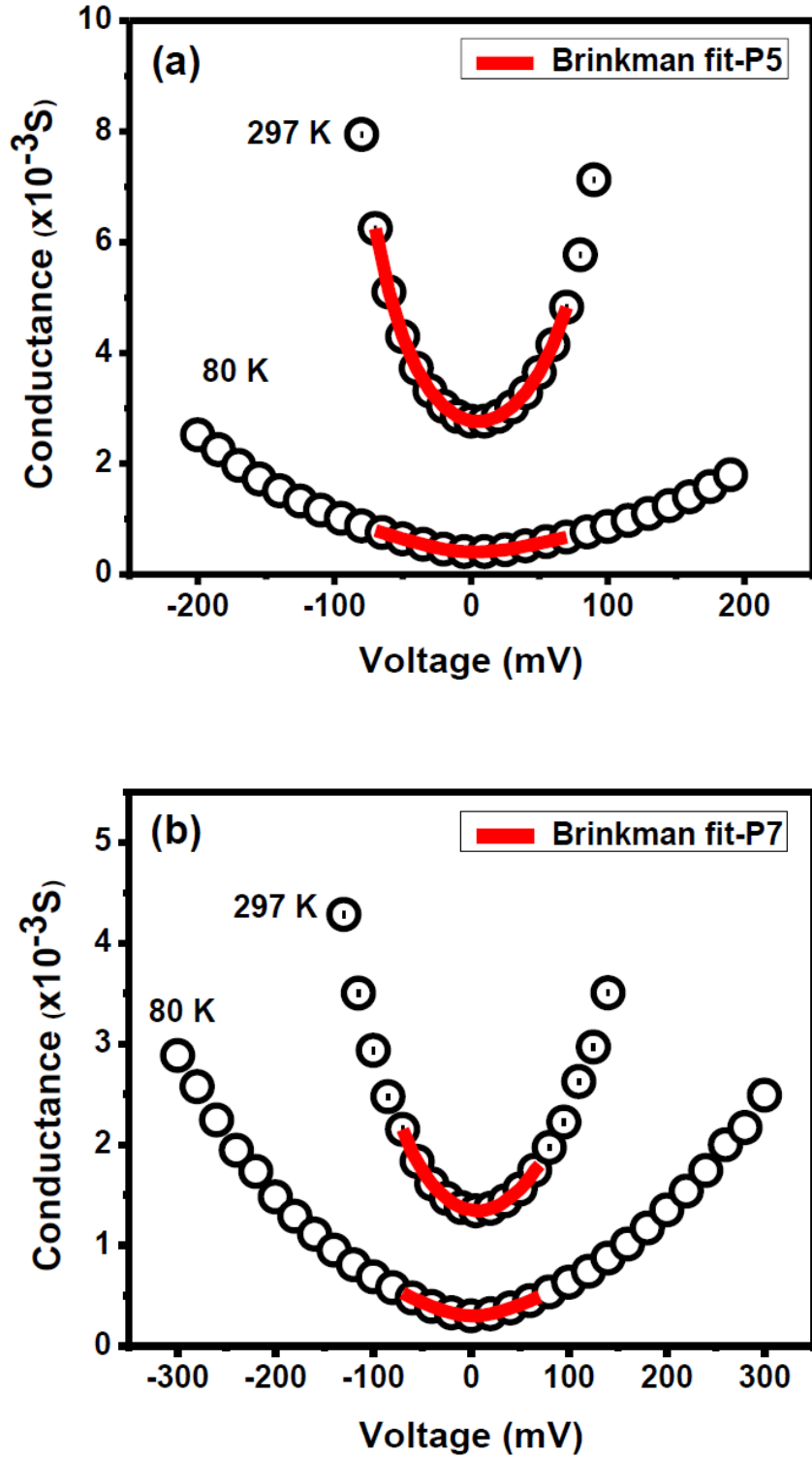


Figure 4.4. Brinkman's model fitting of the low-resistance conductance-voltage curves for: (a) 5 nm and (b) 7 nm thick of $\text{PbZr}_{0.52}\text{Ti}_{0.48}\text{O}_3$ ultrathin films at two different temperatures (80 K and 297K).

behavior of the dynamic conductance is indicative of electron tunneling through an insulating barrier. The observed $G(V)$ characteristic was fitted with Brinkman's model [35].

$$\frac{G(V)}{G(0)} = 1 - \left(\frac{A_0 \Delta\varphi}{16\bar{\varphi}^{\frac{3}{2}}} \right) eV + \left(\frac{9}{128} \frac{A_0^2}{\bar{\varphi}} \right) (eV)^2, \quad (4.1)$$

to obtain following parameters: barrier thickness (d), average barrier height ($\bar{\varphi}$) and the asymmetry in the barrier ($\Delta\varphi$) for the curves with the barrier polarized up or down.

According to the Brinkman model, the expression for conductivity has an error margin around 10% when the barrier thickness is greater than 10 Å and when $\Delta\varphi/\bar{\varphi}$ is less than one. In equation 4.1 we can define $\Delta\varphi = \varphi_2 - \varphi_1$ as the difference of the work functions

of the electrodes with respect to the insulator's conduction band, the average barrier

height $\bar{\varphi} = (\varphi_1 + \varphi_2)/2$, $A_0 = 4(2m)^{1/2}d/3\hbar$ and

$G(0) = (3.16 \times 10^{10} \bar{\varphi}^{1/2}/d) \exp(-1.025 d \bar{\varphi}^{1/2})$. For numerical parameters given above the barrier height ($\bar{\varphi}$) and ($\Delta\varphi$) are given in eV and the barrier thickness (d) in Å.

Our experimental data, taken at low-resistance-state were fitted using the Brinkman model, and the solid line in Figure 4.4 represents equation 4.1. From Figure 4.4 good agreement of the conductance curve with Brinkman's model implies that electron tunneling governs the transport process in these structures. A list of parameters obtained from fitting this model is in table 4.1. The barrier heights at the two interfaces (LSMO/PZT and PZT/Pt) of both structures and at two temperatures are in agreement with the values obtained by others, which range from 0.5 to 1.2 eV [2,33,36-38]. The different barrier heights at the PZT/electrode interfaces presumably result in asymmetric

I(V) curves and a shift of the minimum value of conductance from zero voltage for both 5 and 7 nm PZT barriers.

Table 4.1. The experimental barrier thickness (d_{exp}) and barrier thickness (d), average barrier height ($\bar{\varphi}$) and asymmetry in the barrier height ($\Delta\varphi$) obtained using Brinkman model in the low resistance state (LRS).

State	Temperature (K)	d_{exp} (nm)	d (nm)	$\bar{\varphi}$ (eV)	$\Delta\varphi$ (eV)	φ_1 (eV)	φ_2 (eV)
LRS	80	5	4.5	0.37	0.23	0.25	0.48
LRS	297	5	4.4	0.33	0.28	0.19	0.47
LRS	80	7	4.3	0.40	0.11	0.35	0.46
LRS	297	7	3.7	0.50	0.33	0.33	0.66

For the 5-nm PZT barrier in Figure 4a the value of the barrier thickness shown in table 1 is close to the expected value with approximately 10% difference for two temperatures (80 and 270 K); however, for 7 nm PZT barrier in Figure 4b the difference is approximately 40% for both temperatures (80 and 270 K). These discrepancies in the values of barrier thickness could be due to the following reasons: (i) Brinkman's model shown by equation 4.1 is derived at 0 K, and at such low temperatures the G(V) characteristic can be explained by almost purely tunnel conduction; however, at elevated temperatures, as reported by Oliver et al [39], voltage dependent hopping conductance is also present, which grows proportionally with increasing barrier thickness. Hence, finite temperatures and thicker barriers height may play a crucial role as follows: (i) higher degree of errors at elevated temperatures and bias field; (ii) inter-diffusion at the interface of hetero-structures during growth process; and (iii) finite roughness at the interfaces (LSMO/PZT and PZT/Pt), resulting in hot spots; and finally, (iv) pin holes in the junction.

4.6. CAPACITANCE VOLTAGE CHARACTERISTICS

In order to check the ferroelectric nature of the PZT ultrathin films, we measured DC voltage dependence of the capacitance $C(V)$ measurements. Figures 4.5(a) and (b) show $C(V)$ response of Pt/PZT/LSMO FTJ with PZT barrier of thickness ~ 7 nm and junction area of $16 \mu\text{m}^2$. These measurements were carried out at room temperature where 10 mV AC voltages was applied at 1 kHz frequency, while the DC voltage was swept from positive to negative bias and vice versa. In accordance with PFM measurements, a noticeable signature of two different states was visible in $C(V)$ when the DC voltage applied to the junction was ± 2 V (Figure 4.5(a)), corresponding to a contrast observed between two distinct regions of opposite polarization in PFM measurements (not shown). A clear butterfly loop was observed at applied voltage of ± 3 V, (Figure 4.5(b)) in agreement with the PFM results shown in Figure 4.3(a). The hysteric behavior of the $C(V)$ characteristics can be easily understood in terms of ferroelectric polarization-induced depletion in the LSMO film. Indeed, while the FE polarization rotation has little effect on Pt electrode due to its extremely short screening length (Fermi-Thomas length of < 0.1 nm) and can be omitted, LSMO has a lower carrier concentration and it is affected by induced interface charges. When polarization is pointing toward the interface, the positive electric charges at the PZT/LSMO boundary push the holes, which are the majority current carriers, away from the interface. This carrier depletion effectively increases the thickness of the insulating area and decreases the capacitance. In contrast, when the polarization points away from the interface, negative charges effectively retain carriers at the interface, keeping capacitance at its high value. This argument is further supported by the analysis of the resistive component of the measured impedance, as shown in Figure 4.5(c). The

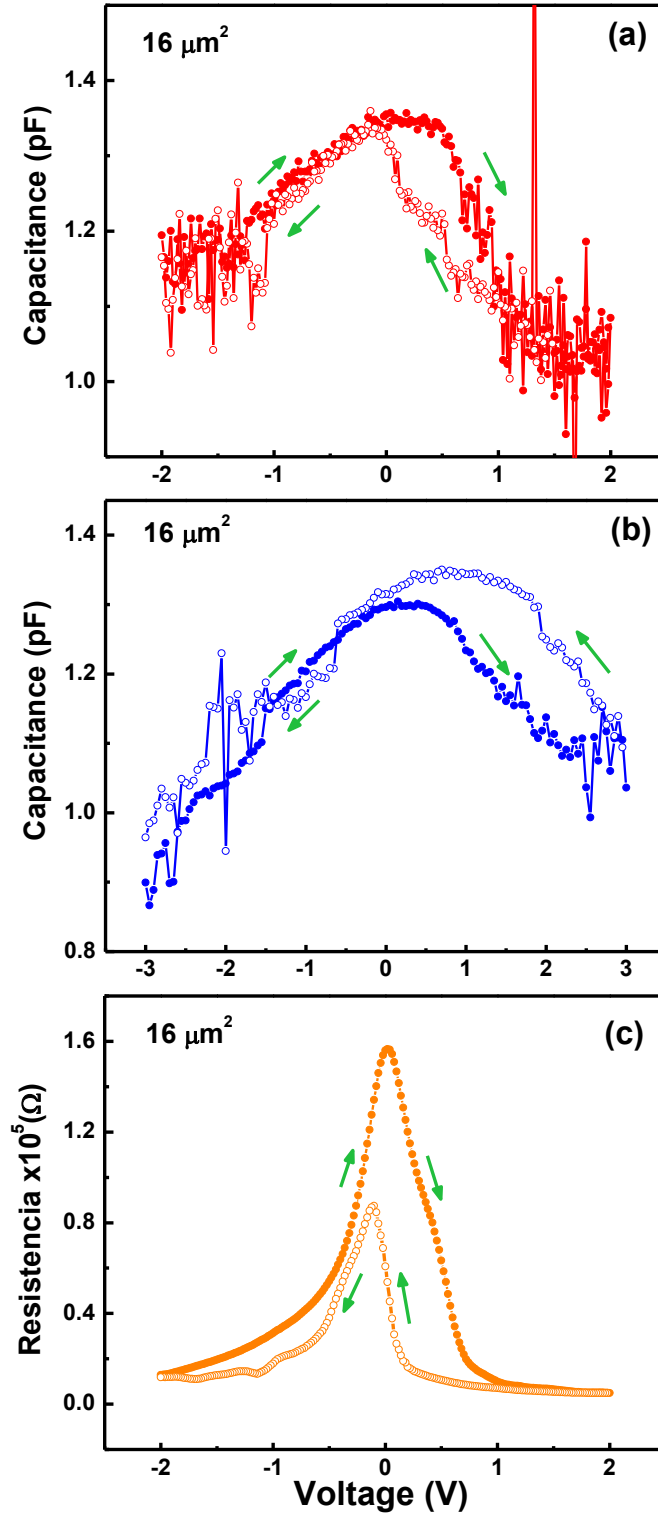


Figure 4.5. Evolution of the capacitance-voltage curve for Pt/P5/LSMO junction at different applied DC voltage (a) 2 V and (b) 3 V. (c) The resistance vs voltage curve exhibited resistance switching properties for the junction.

formation of the depletion area significantly increases the tunneling barrier width and consequently the resistance.

4.7. TRANSPORT PROPERTIES UNDER A MAGNETIC FIELD

Figure 4.6(a) shows the current density versus voltage $J(V)$ curve of a Pt/PZT/LSMO configuration with PZT barrier of ~ 7 nm thick and a junction area of $64 \mu\text{m}^2$. The applied DC voltage was swept from negative to positive bias (-2.7 V to 0 V to $+2.7$ V) and back again ($+2.7$ V to 0 V to -2.7 V) (see arrows in Figure 4.6 and its inset). The $J(V)$ curve clearly shows the resistance switching at voltages ~ -2.0 V and 2.2 V, which are very close to the switching voltage obtained from phase and amplitude PFM measurements. In order to make clear the effect of electrode area on transport properties, the left side inset of Figure 4.6 shows the $J(V)$ curve with a smaller junction area of $4 \mu\text{m}^2$; in this case sharp resistance switching at about -1.7 V and $+2.3$ V was observed, similar to values obtained for $64 \mu\text{m}^2$ junction, indicating homogeneous transport and similar ferroelectric properties of the barrier layer for different sizes of the junction area [19]. In order to verify that the resistance switching observed in $J(V)$ measurements is due to ferroelectric switching in the barrier layer, the $J(V)$ curves were recorded at different DC applied voltages from ± 1.1 V to ± 1.5 , smaller than coercive field. In each case nonlinear $J(V)$ characteristics were observed, indicating tunneling mechanism but without any indication of resistance switching up to bias voltage of ~ 1.5 V. The resistance switching began to appear when the bias voltage was increased to ~ 2.5 V – 3.0 V. These results are in agreement with the PFM measurements in which no polarization

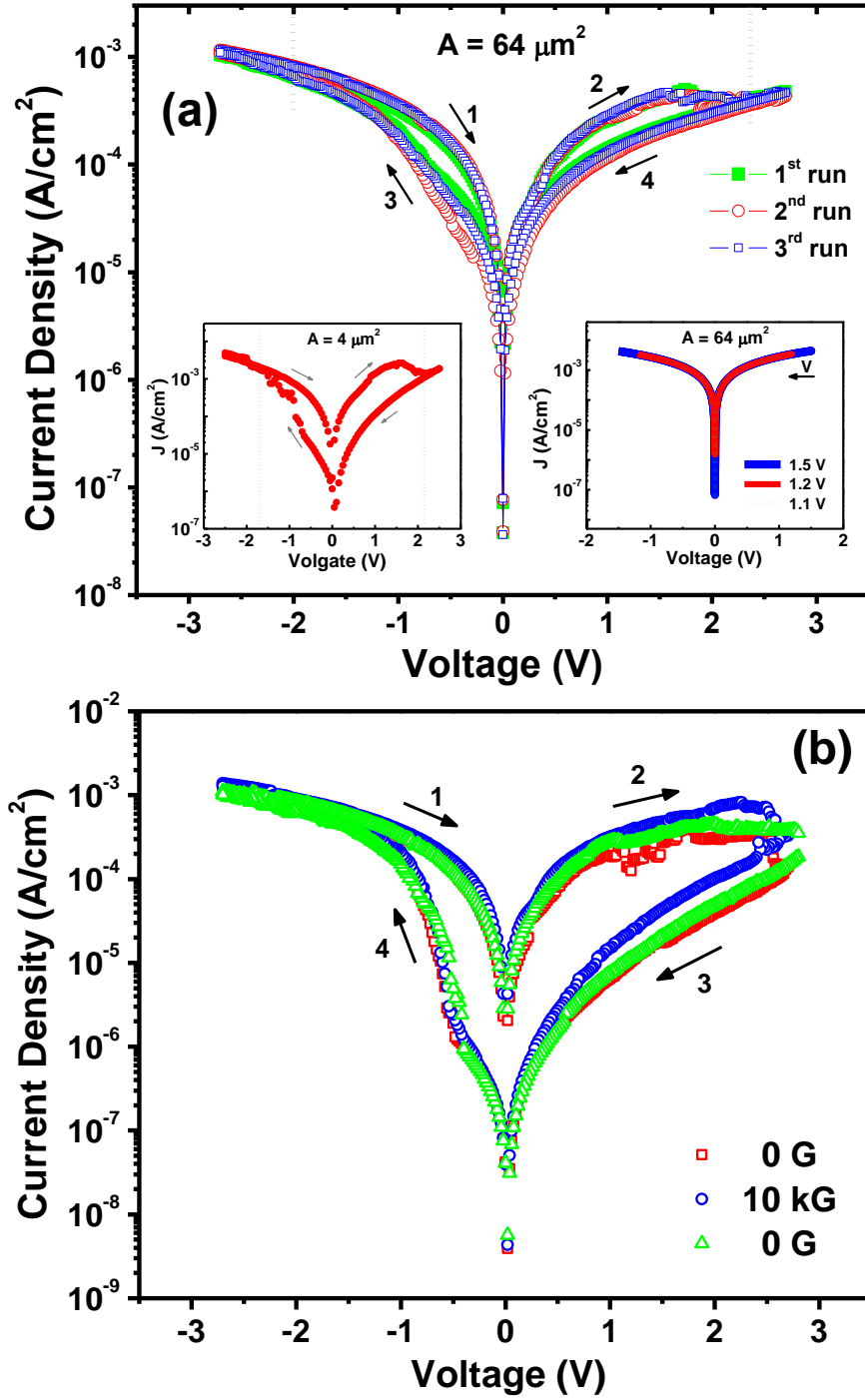


Figure 4.6. (a) Current density versus voltage $J(V)$ curves of the sample P7 showing highly reproducible resistance switching at +2.7 V for a junction area of $64 \mu\text{m}^2$. Left side inset show $J(V)$ loop for the same sample with a junction area of $4 \mu\text{m}^2$. Right side inset present the $J(V)$ curve for sweep voltages from ± 1.1 V to ± 1.5 V. (b) $J(V)$ switching curves of another junction from the same P7 sample showing the effect of an applied 10 kG magnetic field.

switching was observed below 2.0-2.5 V. However, the ratio between the low resistance state (LRS) and the high resistance state (HRS) in case of $64 \mu\text{m}^2$ junctions (HRS/LRS) was between ~ 2 -4, whereas, it was 26:1 for $4 \mu\text{m}^2$. It has been shown by different researchers that this ratio depends strongly on the pinned polarization state at the interface of the electrodes, defects in the ferroelectric barrier, interface quality across the sample, small variations in the PZT thickness through the film, formation of conducting paths due to hot spots or pinholes; and all these factors might induce differences in the switching behavior among different junctions, even in the same film [16,17,33,40-43]. In order to check the reproducibility of the resistance switching, a DC electric field was swept three consecutive times from -2.7 V to 0 V to +2.7 V, and back again, and a well-defined hysteresis in $J(V)$ characteristics was observed in all runs (see 1st, 2nd, 3rd runs in Figure 4.6a) with almost equal values in the current density. From Figures 4.6(a) and (b) we observed a notable asymmetric shape of the $J(V)$ curve in the negative and positive voltage range; this behavior arises from different barrier heights at the electrode/ferroelectric interfaces due to dissimilar top (Pt) and bottom (LSMO) electrodes [2,4,5,13,40].

Figure 4.6(b) shows the effect of magnetic field along the in-plane direction; it was observed when 10 kG was applied to the junction during $J(V)$ measurements, the resistance is decreased only in the positive voltage range (controlled by the LSMO electrode), while no significant change was observed in the negative voltage range (controlled by the Pt electrode). This is reasonable considering that LSMO becomes more metallic in its ferromagnetic state. For this junction the resistance switching between LRS and HRS became sharper, and the HRS/LRS ratio values at zero bias was between ~ 60

(without magnetic field at 0 G) and 110 (with magnetic field at 10 kG); the maximum value of HRS/LRS ratio was obtained in presence of a magnetic field. Sun et al [44] reported a similar result and a qualitative model suggesting that the PZT polarization pins magnetic energy levels. It is worth mentioning that the switching behavior was observed in most of the $J(V)$ curves measured for different junctions in P5 and P7 samples. This behavior is probably due to ferroelectric nature of PZT; however, a significant variation in HRS/LRS ratio at zero bias (HRS/LRS from 2-100) was observed.

REFERENCES

1. Esaki L, Laibowitz R B and Stiles P J, *IBM Tech. Discl. Bull.* **13**, 2161 (1971).
2. Rodriguez Contreras J, Kohlstedt H, Poppe U, Waser R, Buchal C and Pertsev N A, *Appl. Phys. Lett.* **83** 4595-97 (2003).
3. Zhuravlev M Y, Sabirianov R F, Jaswal S S and Tsymbal E Y, *Phys. Rev. Lett.* **94** 246802 (2005).
4. Tsymbal E Y and Kohlstedt H, *Science* **313** 181-83 (2006).
5. Kohlstedt H, Pertsev N A, Rodriguez Contreras J and Waser R, *Phys. Rev. B* **72** 125341 (2005).
6. Gruverman A, Wu D, Lu H, Wang Y, Jang H W, Folkman C M, Zhuravlev M Ye, Felker D, Etom C B and Tsymbal E Y, *Nano Lett.* **9** 3539-43 (2009).
7. Tybell T, Ahn C H, Triscone J M, *Appl. Phys. Lett.* **75**, 856-58 (1999).
8. Fong D D, Stephenson G B, Streiffer S K, Eastman J A, Auciello O, Fuoss P H and Thompson C, *Science* **304** 1650-53 (2004).
9. Bune A V, Fridkin V M, Ducharme S, Blinov L M, Palto S P, Sorokin A V, Yudin S G and Zlatkin A, *Nature* **391** 874-77 (1998).
10. Garcia V, Fusil S, Bouzehouane K, Enouz-Vedrenne S, Mathur N D, Barthelemy A and Bibes M, *Nature* **460** 81-84 (2009).
11. Junquera J and Ghosez P, *Nature* **422** 506-09 (2003).
12. Sai N, Kolpak A M and Rappe A M, *Phys. Rev. B* **72** 020101 (2005).
13. Zhuravlev M Y, Sabirianov R F, Jaswal S S and Tsymbal E Y 2009 Giant Electroresistance in Ferroelectric Tunnel Junctions Erratum: *Phys. Rev. Lett.* **102** 169901
14. Ionescu A M, *Nat. Nanotechnol.* **7** 83-85 (2012).
15. Scott J F, *Science* **315** 954-59 (2007).
16. Pantel D, Lu H D, Goetze S, Werner P, Kim D J, Gruverman A, Hesse D and Alexe M, *Appl. Phys. Lett.* **100** 232902 (2012).
17. Tsymbal E Y, Gruverman A, Garcia V, Bibes M and Barthélémy A, *Mater. Res. Soc. Bull.* **37** 138-43 (2012).

18. Maksymovych P, Jesse S, Yu P, Ramesh R, Baddorf A and Kalinin S, *Science* **324** 1421-25 (2009).
19. Pantel D, Goetze S, Hesse D and Alexe M, *ACS Nano* **5** 6032-38 (2011).
20. Chen J, Lu H, Liu H-J, Chu Y-H, Dunn S, Ostrikov K, Gruverman A and Valanoor N, *Appl. Phys. Lett.* **102** 182904 (2013).
21. Zenkevich A, Minnekaev M, Matveyev Y, Lebedinskii Y, Bulakh K, Chouprik A, Baturin A, Maksimova K, Thiess S and Drube W, *Appl. Phys. Lett.* **102** 062907 (2013).
22. Gao X S, Liu J M, Au K and Dai J Y, *Appl. Phys. Lett.* **101** 142905 (2012).
23. Chanthbouala A, Crassous A, Garcia V, Bouzehouane K, Fusil S, Moya X, Allibe J, Dlubak B, Grollier J, Xavier S, Deranlot C, Moshar A, Proksch R, Mathur N, Bibes M and Barthélémy A, *junctions Nat. Nanotechnol.* **7** 101-04 (2012).
24. Kim D J, Lu H, Ryu S, Bark C W, Eom C B, Tsymbal E Y and Gruverman A, *Nano Lett.* **12** 5697-02 (2012).
25. Yamada H, Garcia V, Fusil S, Boyn S, Marinova M, Gloter A, Xavier S, Grollier J, Jacquet E, Carrétéro C, Deranlot C, Bibes M and Barthélémy A, *ACS Nano* **7** 5385-90 (2013).
26. Yin Y W, Raju M, Hu W J, Weng X J, Zou K, Zhu J, Li X G, Zhang Z D and Li Q, *Front. Phys.* **7** 380-85 (2012).
27. Kim D M, Eom C B, Nagarajan V, Ouyang J, Ramesh R, Vaithyanathan V and Schlom D G, *Appl. Phys. Lett.* **88** 142904 (2006).
28. Barrionuevo D, Ortega N, Kumar A, Chatterjee R, Scott J F and Katiyar R S, *J. Appl. Phys.* **114** 234103 (2013).
29. Ingle N J C, Yuskauskas A, Wicks R, Paul M and Leung S, *J. Phys. D: Appl. Phys.* **43** 133001 (2010).
30. Dussan S, Kumar A, Scott J F and Katiyar R S, *AIP Advances* **2** 032136 (2012).
31. Crassous A, Garcia V, Bouzehouane, S. Fusil, A.H. G. Vlooswijk, G. Rispens, B. Noheda, M. Bibes, A. Barthelemy, *Appl. Phys. Lett.* **96** 042901 (2010).
32. Kim G, Mazumdar D and Gupta A, *Appl. Phys. Lett.* **102** 052908 (2013).
33. Pantel D, Goetze S, Hesse D and Alexe M, *Nature Materials* **11** 289-93 (2012).
34. Wu W, Wong K H, Pang G K H and Choy C L, *Appl. Phys. Lett.* **86** 072904 (2005).

35. Brinkman W F, Dynes R C and Rowell J M, *J. Appl. Phys.* **41** 1915-21 (1970).
36. Sudhama C, Campbell A C, Maniar P D, Jones R E, Moazzami R, Mogab C J and Lee J C, *J. Appl. Phys.* **75** 1014 (1994).
37. Pintilie L, Boerasu I, Gomes M J M, Zhao T, Ramesh R and Alexe M, *J. Appl. Phys.* **98** 124103 (2005).
38. Pintilie L, Vrejoiu I, Hesse D, LeRhun G and Alexe M, *Phys. Rev. B.* **75** 104103 (2007).
39. Oliver B and Nowak J, *J. Appl. Phys.* **95** 546-50 (2004).
40. J. Contreras Rodriguez, (2004). Ferroelectric Tunnel Junctions. University of Cologne (Germany).
41. Lai Y R, Yu K F, Lin Y H, Wu J Ch and Lin J J, *AIP Advances* **2** 032155 (2012).
42. Wicks S, Anbusathiah V and Nagarajan V, *Nanotechnology* **18** 465502 (2007).
43. Pertsev N A, Petraru A, Kohlstedt H, Waser R, Bdikin I K, Kiselev D and Kholkin A L, *Nanotechnology* **19** 375703 (2008).
44. Sun D, Fang M, Xu X, Jiang L, Guo H, Wang Y, Yang W, Yin L, Snijders P C, Ward T Z, Gai Z, Zhang X G, Lee H N, Shen J, *Nat. Commun.* **5**, 4396 (2014).

CHAPTER 5

FERROELECTRIC CAPPED MAGNETIZATION IN TUNNEL JUNCTIONS

5.1. INTRODUCTION

Highly polar ferroelectric thin (< 8 nm) films capable of tunneling charge carriers sandwiched between two metal/ferromagnetic-metal electrodes (MIM structure) produce ferroelectric tunnel junctions (FTJ) [1-3]. Advancements in thin-film growth technologies make it possible to fabricate epitaxial, defect-free, relaxed or strained polar thin films suitable for tunneling devices. FTJs have been a fascinating area of research due to their potential applications as multi-state nonvolatile memory elements with fast write and read logic bits, low power consumption, and small heat dissipation [4]. In addition to using normal metal electrodes in FTJs, scientists are also working with ferromagnetic metal electrodes to make ferroelectric (FE)-ferromagnetic (FM) multiferroic heterostructures that provide an extra degree of freedom to manipulate the logic states. These multiferroic heterostructures provide extra logic states but at the cost of more complex densities of states for charge carriers crossing the junctions. compared to normal metal electrodes; hence a careful study across the FE/electrode interface is needed [5, 6]. One should understand the major problems across the interfaces of the FTJs. These are as follows: (i) less than 3-nm thickness of ferroelectric capping shows poor ferroelectricity for direct transport measurements, using photolithography or electron beam lithography and device areas of a few microns; (ii) quantum tunneling effects diminish greatly for films thicker than 8 nm. Hence to maintain both good ferroelectricity and strong tunneling effects in heterostructures, a thickness window d exists only for $3 \text{ nm} < d < 8$

nm. The present study therefore deals with polar PZT (5 nm and 7 nm) capping on 30 nm thick LSMO films [7, 8].

Several experimental and theoretical research works on FTJ have been demonstrated based on ferroelectric polar barriers such as $\text{Pb}(\text{Zr,Ti})\text{O}_3$ [9-11], BaTiO_3 [12, 13], $(\text{Ba,Sr})\text{TiO}_3$ [14], and polyvinylidene fluoride (PVDF) (70%)–trifluoroethylene (TrFE) (30%) [15]. In these devices polarization reversal provides distinct and significantly different resistive states due to tunnel magnetoresistance (TMR) and tunnel electroresistance (TER). Among ferroelectrics, PZT has a track record of good ferroelectricity down to 2.4 nm and it is popular among researchers for investigation of ultra-thin films [16]. Among strongly correlated materials, strontium-doped lanthanum manganite (LSMO) has shown colossal magneto-resistance phenomena under application of small external magnetic fields. Exchange among the various valence states of Mn-cations leads to complex magnetization properties and transport behavior of LSMO, modulated by external hole/electron doping and electric/magnetic field application [9]. PZT, LSMO, and their heterostructures are of special interest due to rich basic physics and technological applications. There are several reports on the XPS analysis of PZT and LSMO thin films which deal with the compositional analysis of both systems and the valence states of each individual element. A few X-ray photoelectron spectroscopy (XPS) reports are also available in the literature on PZT/LSMO heterostructures; however, a thick layer of PZT restricts the investigation of their chemical and valence states to those near the top surface of the LSMO bottom layer [17, 18]. Note that XPS is surface-sensitive and investigates only a few nanometers below the surface.

Preziosi et al. [10] have carefully demonstrated the transport properties of LSMO (5 nm) under two different polar states of PZT, which revealed that ferroelectric polarization significantly changes the interfacial magnetic anisotropy and affects the spin-orbit coupling. Leufke et al. [11] have shown significant modification of magnetization of LSMO (7.2 nm) thin films with thick polar PZT (90 nm) layers. Switching of ferroelectric polarization towards the LSMO surface (downward) significantly increased the magnetization below the Curie temperature ($T_c \sim 247$ K for 8-nm LSMO film). In this situation holes accumulate at the LSMO interface, which significantly increases the magnetization; and opposite n-type state occurs for upward direction of polarization. As expected, this situation reverses above T_c , which qualitatively differs only in the sign of the modulation.

The presence of ferroelectric and magnetic dead layers is well known in the literature; their thicknesses were found to be 2-5 nm in manganite compounds and 1-2 nm in ferroelectric perovskites. The dead-layer effect is also crucial in the magnetic and polarization properties of FTJs and in magnetic tunnel junction (MTJ) devices which deal with ultra-thin films [19]. In most investigations the active layers of heterostructures are much thicker than the dead layers; only a few reports on multiferroic heterostructure field-effect devices even mention the existence of dead layers. Brivio et al. [20] report the absence of any electric field effect on magnetic modulation of 3-nm LSMO thin films when it was bottom-gated with non-polar SrTiO_3 (STO) thin films, however the effect was significant when applied from the top side. They proposed that this effect was due the presence of a dead layer at the bottom STO/LSMO interface. Molegraaf et al. [21] illustrate a shift of nearly 20 K in the Curie temperature and a 20 % change in magnetic

modulation for STO/LSMO/PZT heterostructures and a change in sign of modulation near 150 K.

Magnetic control of ferroelectric polarization and perturbation of the first unit cell of LSMO under applied electric field, probed by magnetic second-harmonic generation, were shown on PZT/LSMO heterostructures [22, 23]. We have recently demonstrated the tunneling electroresistance (TER) with large resistance ratios (up to 100:1) in heterostructures mainly depends on the active device area [24]. The effect of magnetic fields on TER was also observed and was much greater with applied in-plane magnetic field. Here we report that the capping of polar ferroelectric PZT on LSMO significantly modulates the magnetization of LSMO. The magnetic properties of manganites strongly depend on the Mn valences and the Mn-O-Mn bond angle. XPS studies have been carried out to understand the underlying physics responsible for magnetic modulation.

5.2. EXPERIMENTAL DETAILS

5.2.1 PZT/LSMO ultrathin films grown by pulsed laser deposition.

The PZT/LSMO heterostructure films were grown on $(\text{LaAlO}_3)_{0.3}(\text{Sr}_2\text{AlTaO}_6)_{0.7}$ (LSAT) (001)-oriented substrates, using a pulsed laser deposition (PLD) system. The PZT and LSMO were grown at 600 °C and 700 °C respectively, under an oxygen pressure of ~80 mTorr, using a KrF excimer laser ($\lambda = 248$ nm) with energy density of $\sim 1\text{--}2$ J cm⁻² and deposition frequency of 1 Hz, followed by annealing at 700 °C for 30 min in oxygen at a pressure of ~320 Torr.

5.2.2 Structural, XPS, and magnetic experimental details.

The crystal structure of the films was characterized using x-ray diffraction (XRD) technique. A multimode Nanoscope V (Veeco Instruments) was used to examine the morphology and piezoelectric properties using a conducting tip. The details of the electrical characterization results are described elsewhere [24]. The X-ray photoelectron spectroscopy (XPS) studies were carried out on clean surfaces of heterostructures with a commercial VG ESCALAB 220I-XL imaging system. The XPS spectra were obtained using an Al K_{α} radiation source at 1486.6 eV. The energy spectra of the emitted electrons were analyzed by a hemispherical mirror analyzer with an energy resolution of 0.5 eV. The data were collected in binding-energy mode and calibrated with the standard 285 eV of C 1s binding energy. The magnetic properties were measured using the physical property measurement system (PPMS; Quantum design). The magnetization versus temperature (M-T) measurements were carried out in field-cooled (FC) mode where the samples were first cooled to 10 K under 100 and 1000 Oe magnetic fields, then warmed to 300 K to obtain the FC data. After the M-T measurements were made, hysteresis curves were measured at 50 K under applied fields up to 1 T.

5.3. STRUCTURAL CHARACTERIZATION

Systematic XRD studies have been performed on PZT/LSMO/LSAT heterostructures from 100 nm to down 3 nm PZT with constant LSMO thickness [24, 25]. It was found that 2θ shifted to lower angles with decrease in film thickness. Figure 5.1 shows the weak XRD patterns of both PZT 5 nm and 7 nm samples, oriented along (001/002) planes. The lattice parameters of bulk LSAT, LSMO and tetragonal PZT are

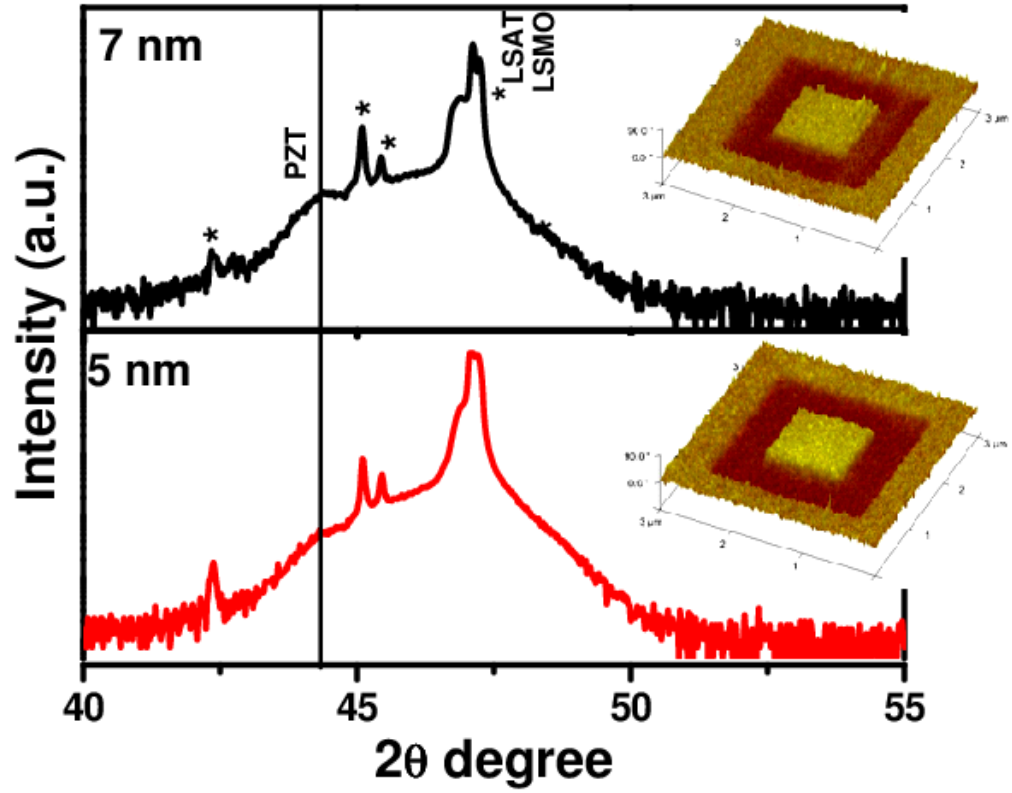


Figure 5.1. The XRD patterns of PZT (5 nm and 7 nm)/LSMO/LSAT heterostructures oriented along the (001/002) plane. Inset illustrates their 3D PFM images under (+/- 3V).

$a_{\text{LSAT}}=3.868 \text{ \AA}$, $a_{\text{LSMO}}=3.871 \text{ \AA}$, and ($a_{\text{PZT}}=4.036 \text{ \AA}$, $c_{\text{PZT}}=4.146 \text{ \AA}$), respectively. These observations suggest a large in-plane compressive strain (-4.26 %) developed in PZT, especially in ultra-thin films, during the growth process, as can be seen in XRD patterns (2θ for PZT $\sim 44.56^\circ$ and LSMO/LSAT $\sim 47.16^\circ$).

5.4. FERROELECTRIC PROPERTIES

The inset of Figure 5.1 illustrates a three-dimensional (3D) image ($3 \times 3 \mu\text{m}^2$) of the polarization switching for both PZT films using PFM with ± 3 V bias voltages. A distinct change in the contrast of poled PZT film surfaces can be seen with positive and negative E-field poling. The PFM scan was first performed over a $2 \times 2 \mu\text{m}^2$ area with +3 V tip bias, later at the center over $1 \times 1 \mu\text{m}^2$ with -3 V tip bias, and finally over the $3 \times 3 \mu\text{m}^2$ area without any tip voltage. The contrast of the -3 V tip bias poling area well matched with the contrast of the area without any poling. These observations imply that as-grown samples are self-poled towards the surface of LSMO with switchable polarization.

5.5. MAGNETIC PROPERTIES

Figure 2(a) and (b) show the magnetic moments of PZT (5 and 7 nm) /LSMO (30 nm) /LSAT heterostructures recorded over 25 to 300 K under 100 Oe and 1000 Oe magnetic fields, below and above the coercive field. Magnetic versus Temperature (M-T) responses show similar trends using 100 and 1000 Oe fields with greater saturation for 1000 Oe. The magnitude of the magnetic moment of 7-nm PZT- capped LSMO is almost 100% higher than that for 5-nm ferroelectric capping; note that the magnetic properties of these films come from similar LSMO dimensions $0.5 \text{ cm} \times 0.5 \text{ cm} \times 30 \text{ nm}$. The magnetic phase transition of LSMO for 5-nm ferroelectric capping was 275 (± 5 K), calculated using Arrott's method [26], far lower than that of the 7-nm PZT-capped LSMO film. The Curie temperature for the 7-nm PZT-capped LSMO was found to be

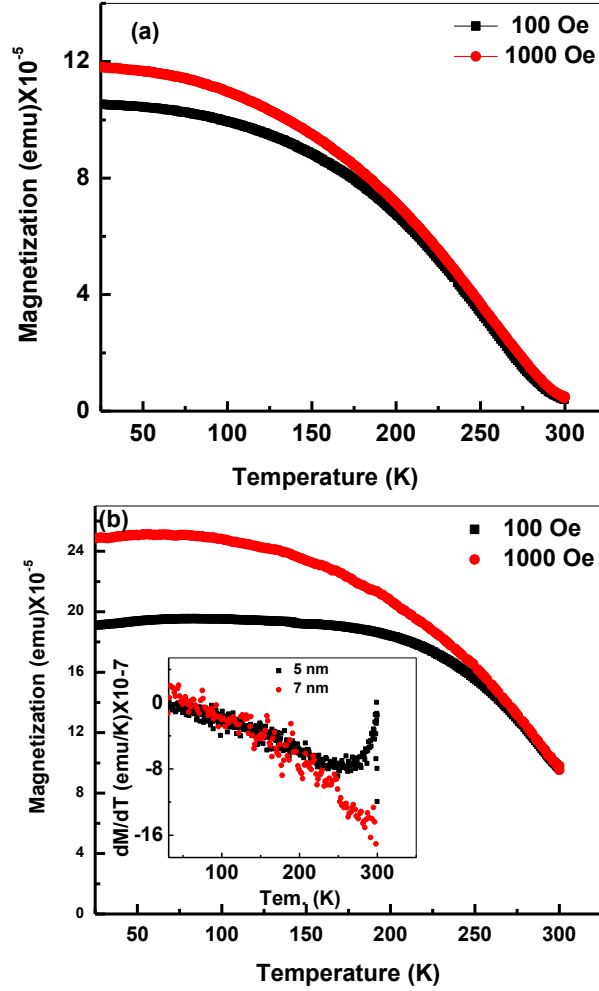


Figure 5.2. M-T graphs of PZT/LSMO(30 nm)/LSAT heterostructures; (a) 5-nm PZT capping; (b) 7-nm PZT capping [at 100 and 1000 Oe magnetic field]. The inset of Fig. 2 (b) shows dM/dT as function of temperature at 1000 Oe field.

beyond the experimental limits. Temperature-dependent differential magnetization (inset Figure 5.2(b)) exhibited a kink for the 5-nm PZT-capped film; however, it was absent for 7-nm capped LSMO.

Figure 5.3 illustrates the comparative magnetic versus magnetic field (M-H) curve of both samples at 50 K, which indicates almost twice the remanent magnetization for the 7-nm capped PZT/LSMO compared to that of the 5-nm PZT; however, the coercive field in both cases was the same. The inset of Figure 5.3 shows the large diamagnetic effect of

the substrate for high probe field that is subtracted for M-H presentation. The first quadrant of the M-H curves indicates that the 5-nm PZT-capped LSMO was almost self-aligned; however, the 7-nm PZT-capped LSMO was less aligned and saturated for higher applied magnetic field.

To explain the magnetic anomaly, we have thoroughly investigated the chemical and compositional behavior of the PZT surfaces and the PZT/LSMO interfaces. It was difficult to probe

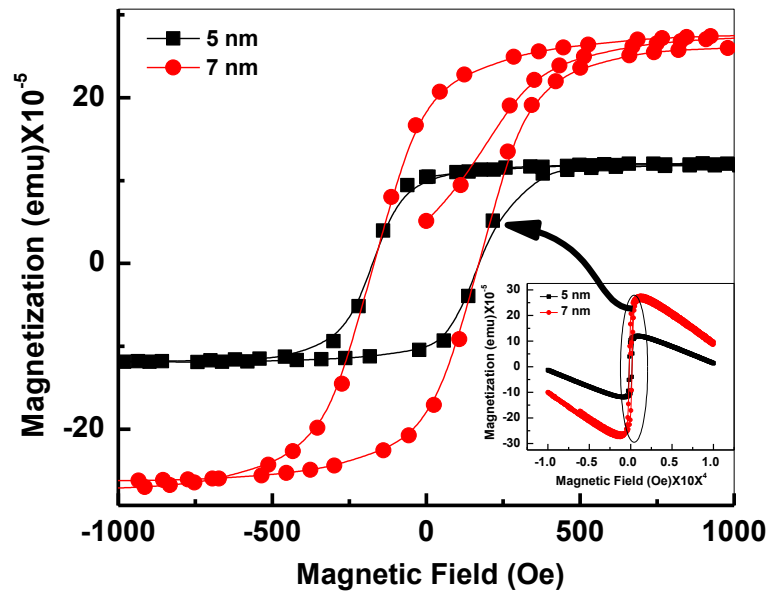


Figure 5.3. M-H graphs of PZT (5 nm and 7 nm)/LSMO(30 nm)/LSAT heterostructures at 50 K; inset shows applied field dependence up to 1.0 T.

the different elements of LSMO, since it is 5 and 7 nm underneath the PZT surface. However, core-level XPS spectra provide qualitative information for possible enhancement in magnetization.

5.5. X-RAY PHOTOELECTRON SPECTROSCOPY (XPS)

Figure 5.4 (a) and (b) show the core-level XPS spectra of Pb 4p_{3/2} and Mn 2p_{3/2} to gain insight into possible changes in oxidation states of Mn and changes in the spin-orbit coupling. It was difficult to deconvolute all the peaks, since Pb 4p peaks and Mn 2p peaks are both within the same 641-647 eV range of binding energy (B.E). The Pb 4p peaks dominate the Mn 2p peaks; however, using XPSPEAK41 online software with proper background corrections and normalized peaks intensity and based on the literature reports, [17, 18, 27] we were able to fit the raw data with the known Pb and Mn peaks. Carefully fitted graphs indicate that the Mn³⁺ states are significantly enhanced for 7-nm PZT-capped LSMO films. This enhancement in Mn³⁺ states may be due to the comparatively large hole doping by the self-poled 7-nm PZT film. To further support this, Mn 3s core-level spectra (free from overlapping of Pb spectra) were fitted for the pure Mn 3s (83.7 eV) peak and the exchange-splitting (ES) shoulder at 88.6 eV which is produced by spin-orbit coupling (SOC) supported exchange. A significant enhancement in the normalized intensity of this SOC supported ES shoulder can be seen in Figure 4(c,d). Qualitative analysis of Mn 2p (3+) and Mn 3s peaks indicate that Mn³⁺ and SOC are playing significant roles in the improvement of the 7-nm PZT-capped LSMO films.

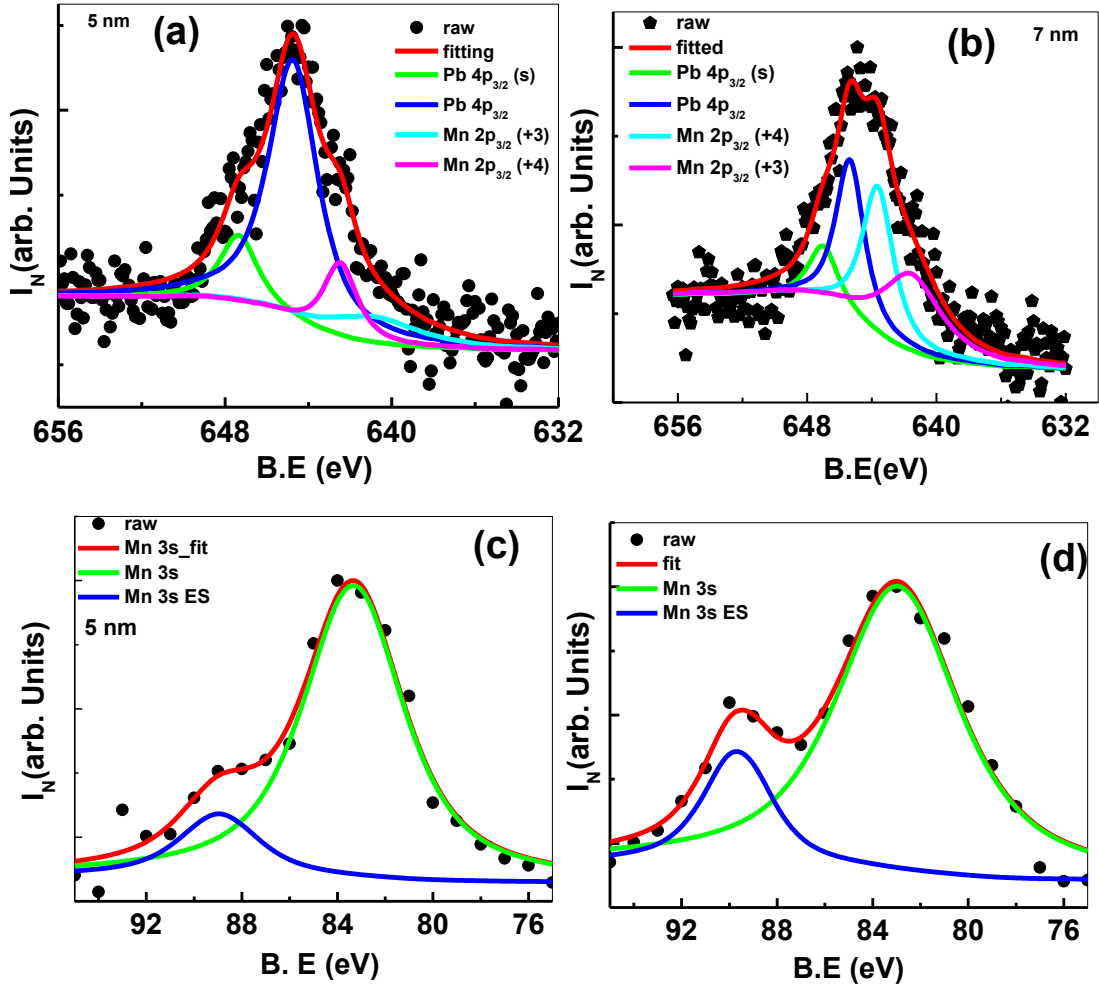


Figure 5.4. (a-d) The core-level XPS spectra of Pb 4p_{3/2}, Mn 2p_{3/2}, and Mn 3s peaks: (a) Pb 4p_{3/2}, Mn 2p_{3/2} for 5-nm PZT capping; (b) Pb 4p_{3/2}, Mn 2p_{3/2} for 7-nm PZT capping; (c) Mn 3s for 5-nm PZT capping; and (d) Mn 3s for 7-nm PZT capping.

Figure 5.5 (a) and (b) show the Ti 2p XPS core-level spectra of 5-nm and 7-nm PZT-capped LSMO films, respectively. The spectra were normalized to verify Ti valences: the two peaks observed are ascribed to Ti 2p_{3/2} and Ti 2p_{1/2} spin-orbit components [28]. Raw data as well as fitted data don't reveal any shoulder on the higher B.E of Ti 2p_{3/2} peak, which rules out any trace of T³⁺-ions responsible for magnetism. XPS spectra of Ti 2p_{3/2} peaks

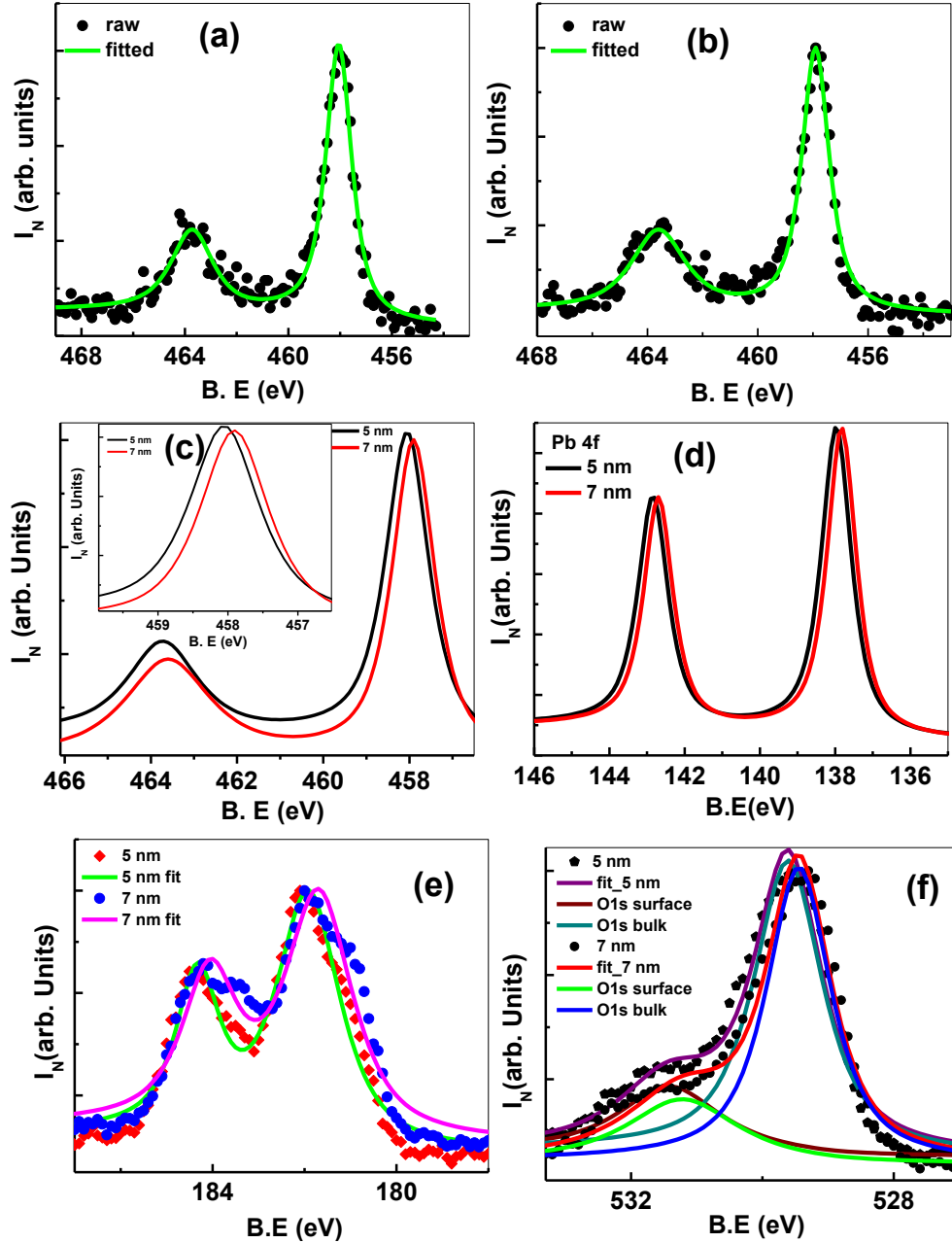


Figure 5.5. (a-f) Show the core level XPS spectra of: (a) Ti 2p_{3/2} , Ti 2p_{1/2}, for 5-nm PZT capping; (b) Ti 2p_{3/2} , Ti 2p_{1/2}, for 7-nm PZT capping; (c) comparative Ti 2p peaks; (d) comparative Pb 4f peaks; (e) Zr 3d peaks; and (f) O1s peaks for both 5- and 7-nm PZT capping.

demonstrate (Figure 5.5(c)) a shift of nearly 0.25 eV in B.E to the low energy side for 7-nm PZT-capped LSMO, which indicates relaxation in the in-plane compressive strain

with increase in polar capping thickness. XPS spectra for Pb 4f states show almost negligible change in shape and broadening with increased thickness of capping layer; however, a 0.1-eV shift in peak position towards the lower B.E side was observed for 7-nm PZT capping (Figure 5.5(d)). An interesting feature was observed in Zr 3d XPS spectra (Figure 5.5(e)). Most of the features were similar to other reported data for PZT XPS spectra, but 7-nm PZT capping showed a sharp kink (~ 183.5 eV) near the lower binding energy of Zr 3d_{1/2} spin-orbit components. This kink suggests that SOC significantly modifies the d-orbital of the Zr atom sitting at the center of the oxygen octahedra. Asymmetry in Zr 3d_{1/2} and Zr 3d_{3/2} peaks provide large uncertainties in the fitting of raw data. Figure 5.5 (f) shows the O 1s surface and bulk XPS spectra. It would be unwise to discriminate the contribution of O 1s from PZT and LSMO; in general, both systems show indistinguishable XPS peaks. The only distinction in O1s XPS spectra is the shift to the lower B.E side and less contribution of surface oxygen (normalized relative intensity compensating for smaller area) with 7-nm PZT capping on LSMO films. The analysis of XPS spectra implies the presence of less in-plane compressive strain in the 7-nm PZT-capped LSMO films. Mn 3s and Mn 2p_{3/2} (3+) spectra indicate a strong SOC and excess presence of Mn³⁺ cations for thicker polar capping.

REFERENCES

1. L. Esaki, R. B. Laibowitz, and P. J. Stiles, *IBM Tech. Discl. Bull.* **13**, 2161 (1971).
2. E. Y. Tsymbal and H. Kohlstedt, *Science* **313**, 181 (2006).
3. M. Ye. Zhuravlev, R. F. Sabirianov, S. S. Jaswal, and E. Y. Tsymbal, *Phys. Rev. Lett.* **94**, 246802 (2005).
4. J. R. Contreras, H. Kohlstedt, U. Poppe, R. Waser, C. Buchal, and N. A. Pertsev, *Appl. Phys. Lett.* **83**, 4595 (2003).
5. J. P. Velez, J. M. López-Encarnación, J. D. Burton, and E. Y. Tsymbal, *Phys. Rev. B* **85**, 125103, (2012).
6. V. Garcia, S. Fusil, K. Bouzehouane, S. Enouz-Vedrenne, N. D. Mathur, A. Barthelemy, and M. Bibes, *Nature* **460**, 81 (2009).
7. G. Catalan, H. Béa, S. Fusil, M. Bibes, P. Paruch, A. Barthélémy, and J. F. Scott, *Phys. Rev. Lett.* **100**, 027602 (2008).
8. M. Dawber, K. M. Rabe, and J. F. Scott, *Rev. Mod. Phys.* **77**, 1083 (2005).
9. D. Pantel, H. Lu, S. Goetze, P. Werner, D. J. Kim, A. Gruverman, D. Hesse, and M. Alexe, *Appl. Phys. Lett.* **100**, 232902 (2012).
10. D. Preziosi, I. Fina, E. Pippel, D. Hesse, X. Marti, F. Bern, M. Ziese, and M. Alexe, *Phys. Rev. B* **90**, 125155 (2014).
11. P. M. Leufke, R. Kruk, R. A. Brand, and Horst Hahn, *Phys. Rev. B* **87**, 094416 (2013).
12. A. Chanthbouala, A. Crassous, V. Garcia, K. Bouzehouane, S. Fusil, X. Moya, J. Allibe, B. Dlubak, J. Grollier, S. Xavier, C. Deranlot, A. Moshar, R. Proksch, N. Mathur, M. Bibes, and A. Barthelemy, *Nat. Nanotechnol.* **7**, 101 (2012).
13. D. J. Kim, H. Lu, S. Ryu, C. W. Bark, C. B. Eom, E. Y. Tsymbal, and A. Gruverman, *Nano Lett.* **12**, 5697 (2012).
14. Y. W. Yin, M. Raju, W. J. Hu, X. J. Weng, K. Zou, J. Zhu, X. G. Li, Z. D. Zhang, and Q. Li., *Front. Phys.* **7**, 380 (2012).
15. H. Qu, W. Yao, T. Garcia, J. Zhang, A. V. Sorokin, S. Ducharme, P. A. Dowben, and V. M. Fridkin, *Appl. Phys. Lett.* **82**, 4322 (2003).

16. A. Lookman, R. M. Bowman, J. M. Gregg, J. Kut, S. Rios, M. Dawber, A. Ruediger, and J. F. Scott, *J. Appl. Phys.* **96**, 555 (2004).
17. N. Wakiya, K. Kuroyanagi, Yi Xuan, K. Shinozaki, and N. Mizutani, *Thin Solid Films* **372**, 156 (2000).
18. V. R. Galakhov, M. Demeter, S. Bartkowski, M. Neumann, N. A. Ovechkina, E. Z. Kurmaev, N. I. Lobachevskaya, Ya. M. Mukovskii, J. Mitchell, and D. L. Ederer, *Phys. Rev. B* **65**, 113102 (2002).
19. C. A. F. Vaz, Y. Segal, J. Hoffman, R. D. Grober, F. J. Walker, and C. H. Ahn, *Appl. Phys. Lett.* **97**, 042506 (2010).
20. S. Brivio, M. Cantoni, D. Petti, and R. Bertacco, *J. Appl. Phys.* **108**, 113906 (2010).
21. H. J. A. Molegraaf, J. Hoffman, C. A. F. Vaz, S. Gariglio, D. vander Marel, C. H. Ahn, and J.-M. Triscone, *Adv. Mater.* **21**, 3470, (2009).
22. S. Dussan, A. Kumar, J. F. Scott, S. Priya, and R. S. Katiyar, *Appl. Phys. Lett.* **97**, 252902 (2010).
23. X. Ma, A. Kumar, S. Dussan, H. Zhai, F. Fang, H B Zhao, J F Scott, R S Katiyar, G Lüpke
Appl. Phys. Lett. **104**, 132905 (2014).
24. D. Barrionuevo, Le Zhang, N. Ortega, A. Sokolov, A. Kumar, P. Misra, J. F. Scott, and R. S. Katiyar, *Nanotechnology* **25**, 495203 (2014).
25. D. Barrionuevo, N. Ortega, A. Kumar, R. Chatterjee, J. F. Scott, and R. S. Katiyar, *J. Appl. Phys.*, **114**, 234103 (2013).
26. A. Arrott, *Phys. Rev.* **108**, 1394 (1957).
27. N. Tayebi, S. Kim, R. J. Chen, Q. Tran, N. Franklin, Y. Nishi, Q. Ma, and V. Rao, *Nano Lett.* **12**, 5455 (2012).
28. H. Lu, T. A. George, Y. Wang, I. Ketsman, J. D. Burton, C.-W. Bark, S. Ryu, D. J. Kim, J. Wang, C. Binek, P. A. Dowben, A. Sokolov, C.-B. Eom, E. Y. Tsymbal, and A. Gruverman, *Appl. Phys. Lett.* **100**, 232904 (2012).

CHAPTER 6

THICKNESS DEPENDENT MULTIFERROIC PROPERTIES OF PZTFT

6.1. INTRODUCTION

In multiferroic materials there coexist at least two different ferroic orders (ferromagnetism, ferroelectricity, ferroelasticity, and ferrotoroidicity), which are often coupled. Multiferroic magnetoelectric materials combine ferromagnetism and ferroelectricity, combining the possibility of controlling polarization (P) with a magnetic field (H) or magnetization (M) with an electric field E [1-14]. The strong coupling between the ferromagnetic and ferroelectric orders is expected to produce new magnetoelectric, magneto-capacitive, and magneto-optic properties. These properties would exploit the best features of ferroelectricity and magnetism, for example with electrical-writing and magnetic-reading in random access memories. This memory device is only one example of the range of potential applications of magnetoelectric technologies that have been proposed; they have also potential application in information storage, spintronics, magnetic field sensing, and transducers. In the field of information storage these materials could bring significant advances in memories, displaying fast and low-power write operation combined with non-destructive reading. Another way to exploit the magnetoelectric multiferroic nature of single-phase materials is to use them as tunnel barriers in multiferroic tunnel junctions. Ultrathin films offer the opportunity of combining the respective advantages of fast low-power electrical write operation and

non-destructive magnetic read operation in ferroelectric random access memories (FeRAMs) and magnetic random access memories (MRAMs), resulting in the realization of four-state logic, as well as the exploitation of magnetoelectric random access memories (MERAMs) which combine the magnetoelectric coupling where the spin is controlled by electric field [15-20]. However, most single-phase multiferroic materials exhibit low Curie temperatures and weak magnetoelectric coupling [21-30]. This makes them limited for practical applications. For these reasons, $\text{Pb}(\text{Zr}_{0.53}\text{Ti}_{0.47})_{0.60}(\text{Fe}_{0.5}\text{Ta}_{0.5})_{0.40}\text{O}_3$ (PZTFT) is a good candidate for many applications, because this material is a single-phase magnetoelectric multiferroic at room temperature [31-37]. Sanchez et al. [28] showed multiferroic properties in a Pt/PZTFT(350 nm)/LSCO/MgO configuration at room temperature. And Evans et al. [30] showed that PZTFT single crystal lamella with a modest magnetic field can induce partially reversible changes in ferroelectric domains. These previous studies were made for thickness above 300 nm. However, for multiferroic tunnel junction (MFTJ) device applications, the multiferroic properties of single-phase multiferroic tunnel barrier must persist below 10 nm, where quantum mechanical tunneling occurs. Recent research has focused on nonvolatile memory devices based on MFTJ with a multiferroic tunnel barrier. The first work with a multiferroic tunnel barrier was reported by Gajek et al. [38] using $\text{La}_{0.1}\text{Bi}_{0.9}\text{MnO}_3$ ultrathin films as tunnel barriers that can operate as a four-resistance-state system. This gave the possibility to encode quaternary information and to read out it non-destructively by a resistance measurement; however, this device required liquid helium to operate, because the four-resistance-state was obtained at low temperature (10 K). For practical applications the devices need to work at room temperature. For this reason, we

propose PZTFT as a multiferroic tunnel barrier in MFTJ. This should be a very promising candidate for next-generation nonvolatile memory devices.

We focused on the effect of thickness of PZTFT on its magnetic, ferroelectric and transport properties.

6.2. EXPERIMENTAL DETAILS

6.2.1 PZTFT and LSMO bilayer thin films grown by pulsed laser deposition.

PZTFT/LSMO heterostructures films were grown on $(\text{LaAlO}_3)_{0.3}(\text{Sr}_2\text{AlTaO}_6)_{0.7}$ (LSAT) (001)-oriented substrates, using pulsed laser deposition (PLD) system, with a KrF excimer laser ($\lambda=248$ nm). The PZTFT and LSMO were grown at 600 °C and 700 °C respectively, under an oxygen pressure of ~150 mTorr, using a laser energy density of ~1-2 J/cm² and deposition frequency of 5 Hz, followed by annealing at 700 °C for 30 min in oxygen at a pressure of ~300 Torr. The films were cooled down to room temperature at a rate of 5 °/min. The thickness of the PZTFT and LSMO were controlled by the number of laser shots. The thicknesses of PZTFT were 80, 50, 20, 7 nm for each heterostructure films, whereas the thickness of the LSMO layer was keep constant (~100 nm) for the range 20-80 nm thin PZTFT films and (~60 nm) for 7-nm ultrathin films of PZTFT.

6.2.2 Structural, ferroelectric, magnetic, and transport experimental details.

The crystal structure of all the films were characterized using x-ray diffraction (XRD) with $\text{CuK}\alpha$ radiation, a step size of 0.02° and scanning speed of 1.5 °/min. XRD patterns were recorded over the angular range 20°-60° (2 θ) with wavelength of $\lambda =$

1.5405 Å. A multimode Nanoscope V (Veeco) was used to examine the morphology of all thin films (atomic force microscopy, contact-mode AFM); and the nanoscale ferroelectric and magnetic properties of the PZTFT layers were done by piezoresponse force microscopy (PFM) and magnetic force microscopy (MFM). For AFM measurements a commercial silicon nitride tip was used with back-side coating (Ti/Au 45 nm); for PFM, an antimony (n)-tipped doped-Si coated with Pt/Ir; and for MFM, antimony (n)-tipped doped-Si coated with Co/Cr were used. The electrical measurements were carried out in a metal-insulator-metal (MIM) configuration with Pt top electrode (square of side 100 μm) deposited by dc sputtering through a shadow mask. The capacitance and loss spectra were measured in the temperature range of 100 °C to 600 °C for frequencies between 100 Hz to 1 MHz by using a programmable temperature controller (MMR K-20) and an impedance analyzer (HP 4294A). Ferroelectric hysteresis loops were measured using a hysteresis loop tester (Radiant Technologies RT6000 HVS). The magnetic measurements (magnetization (M) versus magnetic field (H) and the magnetization (M) versus temperature (T)) were performed using a physical property measurement system (PPMS) (Quantum Design). M - H loops at 300 K and 5 K were measured in magnetic field range ($-10 \text{ kOe} \leq H \leq 10 \text{ kOe}$). For M - H loops at 5 K, the sample was cooled in zero-field from 300 K down to 5 K and the measurements made at 5 K for the complete loop. For M - T data, the samples were cooled from 300 K to lowest temperature 5 K in zero-field, and then a magnetic field of 100 Oe was applied and M - T data recorded while heating the sample from 5 K to 390 K. This is denoted as ZFC data. After the sample reached 390 K, the M - T data were recorded during cool down process in the same applied field to the lowest temperature of 5 K (field-cooled-cooling, FCC). The

transport measurements were made with a Keithley 2400 multimeter at room temperatures.

6.3. STRUCTURAL AND SURFACE MORPHOLOGY CHARACTERIZATION

The XRD patterns of PZTFT/LSMO heterostructures are shown in Figure 6.1. In all heterostructures only the (00 l) ($l = 1$ and/or 2) reflections corresponding to the LSAT substrate, PZTFT, and LSMO layers are present in the range of 20°- 60°. According to these observations

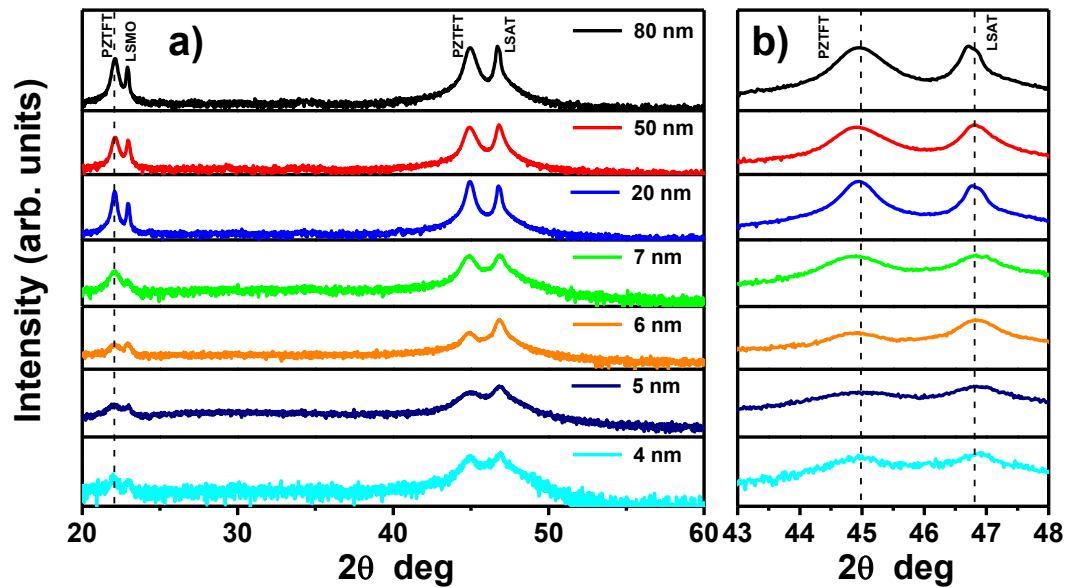


Figure 6.1. (a) XRD patterns for different PZTFT thicknesses grown on LSMO/LSAT show only peaks of these materials without any additional second phase. (b) The effect of thickness on crystallization, possibly due to the quick increase of compressive stresses with a decrease in film thickness due to PZTFT and LSMO lattice mismatch.

the individual PZTFT and LSMO phases are retained in the heterostructure films. Bulk LSAT and LSMO have a cubic perovskite structure with lattice parameter of $a_{\text{LSAT}} = 3.868 \text{ \AA}$ and $a_{\text{LSMO}} = 3.871 \text{ \AA}$ respectively, while PZTFT has an orthorhombic structure with $a_{\text{PZTFT}} = 4.038 \text{ \AA}$, $b_{\text{PZTFT}} = 4.047 \text{ \AA}$, and $c_{\text{PZTFT}} = 4.058 \text{ \AA}$ at room temperature.

Sanchez et al. [34] have reported the phase transitions in ceramic PZTFT using temperature dependent XRD and Raman spectroscopy: cubic $Pm3m$ above 1300 K; tetragonal $P4mm$ in the range 460 K to 1300 K; orthorhombic $Pmm2$ in the range from 250 K to 460 K; and rhombohedral or monoclinic (unknown space group) below 250 K. Additionally, Schiemer et al. [36] have provided a detailed study of three phase transitions in ceramic PZTFT: magnetization increases rapidly below 40 K; a broad peak is seen near 240 K, where a rhombohedral-orthorhombic transformation occurs; and the orthorhombic-tetragonal transition takes place at 475 K. They found these phase transitions using SQUID measurements of magnetization, combined with measurements of electric properties and changes in elastic properties (from resonant ultrasound spectroscopy).

In our data the crystallization of all thin films is drastically reduced with decreasing film thickness. The peaks of the PZTFT thin films ($\sim 22^\circ$ and $\sim 44.9^\circ$) were narrowed with increase in thickness from 4 nm to 80 nm, as shown in Figures 6.1(a) and (b). The effect of thickness on crystallization may be due to the rapid increase of compressive stress (imposed by the LSMO electrode, which has an in-plane lattice parameter smaller than that of PZTFT) with decreasing film thickness; it is expected to decrease/increase the in/out-of-plane lattice parameter, respectively; however, the strain effect decreases with increase in film thickness [39, 40].

Figure 6.2 shows the surface morphology for different thicknesses of PZTFT thin films deposited on LSMO/LSAT substrates. These measurements were made using atomic force microscopy in contact mode with scan size of $3 \times 3 \mu\text{m}^2$. Figure 6.2(a)-(f) shows a flat surface without granular structure with a root-mean-square (R_{rms}) surface roughness

of a) 2.25 nm, b) 1.48 nm, c) 1.24 nm, d) 1.13 nm, e) 0.87 nm and f) 0.54 nm for 80, 50, 20, 7, 5, and 4 nm of PZTFT thickness, respectively. The z-scale for samples were kept to ~20 nm of height to facilitate comparison among them. It is clearly seen that the surface morphology of all structures displays a smooth and very homogeneous surface, free of microcracks, pores or holes. The smooth surface and low roughness characteristics of the PZTFT ultrathin films make them appropriate for multiferroic tunnel junction applications.

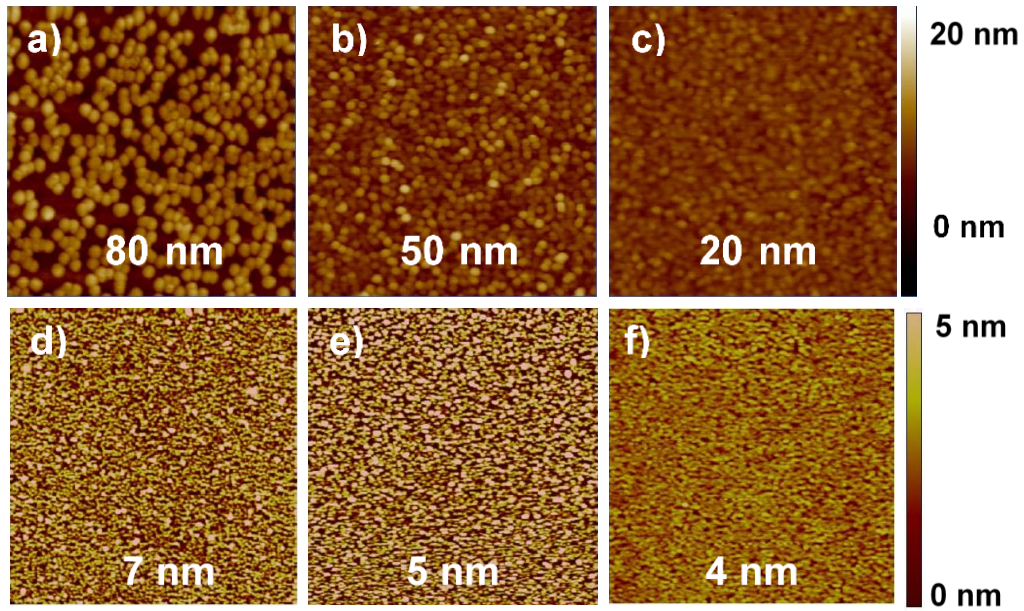


Figure 6.2. Atomic force microscopy surface topography images for different PZTFT thicknesses: (a) 80 nm, (b) 50 nm, (c) 20 nm, (d) 7 nm, (e) 5 nm, and (f) 4 nm. The reduction in roughness with decreasing film thickness may be due to a reduction in grain size.

6.4. DIELECTRIC PROPERTIES

Metal/insulator/metal (MIM) sandwich structures of (Pt/PZTFT/LSMO) were prepared for electrical measurements, and the dielectric properties were measured at 100

mV oscillator level. Figure 6.3 (a)-(b) illustrate the frequency dependence of dielectric constant (ϵ_r) and loss tangent ($\tan \delta$) for different thickness of PZTFT at room temperature. The dielectric constants for all films have the following characteristics: i) weak frequency dependence below 5×10^4 Hz; ii) a significant reduction in dielectric constant values above 5×10^4 Hz; and iii) an enhancement of the dielectric constant values when the thickness of PZTFT thin films was increased. The dielectric constant values increase from 50 to 310 when the PZTFT thickness increases from 20 nm to 80 nm. This evolution has been observed in many ferroelectric thin films [41-43]. There are several factors responsible for the dielectric dispersion: 1) The extrinsic sources can be ascribed to the additional capacitance arising from the grain boundary and interface effects (Pt/PZTFT and PZTFT/LSMO). 2) There are several kinds of polarization (dipole polarization, electronic polarization, etc.) contributing to the dielectric constant of the thin films. In the lower frequency region, the dielectric constant is high since all the defect dipole polarization can follow reversal of the external electric field. With increasing frequency, the polarization cannot follow in phase the reversal of the external electric field, and the polarization slowly diminishes, which contributes to the decrease of dielectric constant [44]. 3) The dielectric and conductive properties of LSMO are highly dependent on the strain and grain boundary configuration of the LSMO film [45]. Measurements of dielectric constant versus frequency for pure LSMO films show a similar trend compared with PZTFT/LSMO bilayer structures; they exhibit large dielectric dispersion at higher frequencies that is more

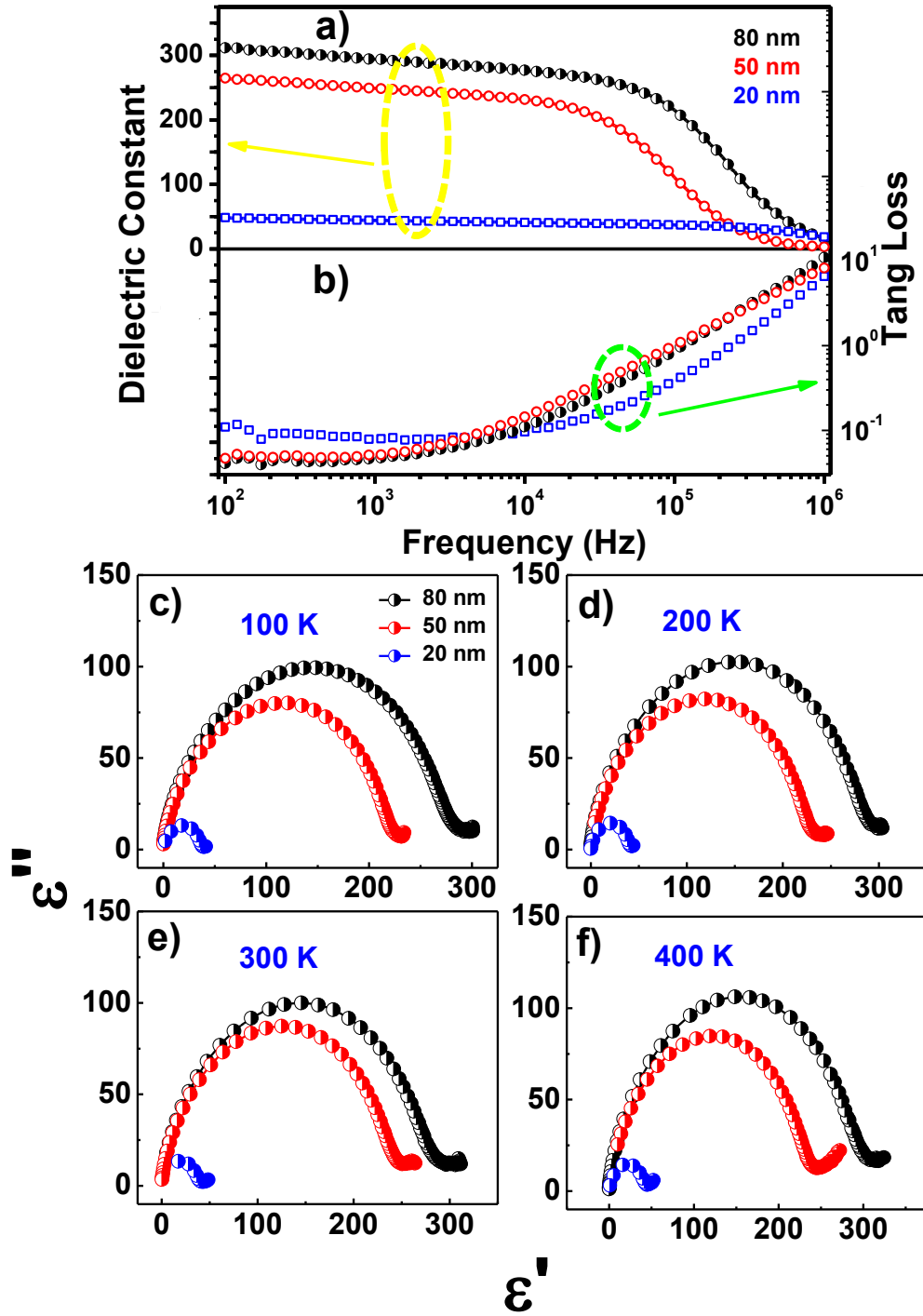


Figure 6.3. (a) The dielectric constant (ϵ_r), and (b) loss tangent ($\tan \delta$) versus frequency for different thicknesses of PZTFT at room temperature. (c), (d), (e) and (f) show Cole-Cole plots of the temperature-dependent dielectric permittivity real (ϵ') and imaginary (ϵ'') parts for different thicknesses. The semicircles imply a single relaxation time.

pronounced in the LSMO films that have larger grain boundary population. The frequency dispersion observed in PZTFT/LSMO bilayer structures can be due to the LSMO dielectric response. 4) This increase in dielectric constant with thickness can be due to the dependence of the intrinsic (lattice contributions) and extrinsic contributions (domain wall motion) to the dielectric properties [46-48]. Similar behavior was observed in the loss tangent for the thin films, which remained almost constant with values of 0.08, 0.06, and 0.05 for 20, 50, and 80 nm PZTFT thickness in the frequency range from 100 Hz to 5×10^4 Hz. When the frequency increases beyond 5×10^4 Hz, the loss tangent increases with frequency could be due to rapid decrease of dielectric loss mechanisms (e.g., electronic and ionic polarization) and conductivity with the increase of frequency. Dielectric constant and loss tangent properties are important for the operation of electronic devices fabricated with any dielectric thin films.

Figures 6.3 (c), (d), (e) and (f) show the Cole-Cole plots of the temperature-dependent dielectric permittivity of the real (ϵ') and imaginary (ϵ'') part of PZTFT for different films thickness (20, 50 and 80 nm). The ϵ' vs. ϵ'' response of the PZTFT/LSMO structures with different PZTFT thicknesses for 100 K, 200 K, 300 K, and 400 K have the following characteristics: i) The ϵ' radius of the semicircular arc shows small variation with temperature for thickness 20, 50 and 80 PZTFT samples; ii) With increasing temperature the bulk permittivity contribution (ϵ' radius, when $\epsilon'' = 0$) in the Cole-Cole plot increases with PZTFT thickness: at 400 K the ϵ' radius was 50, 250, and 310 for 20, 50, and 80 nm, respectively; iii) Since the intercept of the semicircular arc gives an estimation of sample resistance, this indicates that for ultrathin films the resistance changes only slightly with temperature; iv) The ϵ'' values is more significant for (50 and

80 nm of PZTFT thickness) samples compared with 20 nm of PZTFT thin films. These behaviors are due to the thickness of the films, because ϵ' and ϵ'' depend directly on the dielectric constant. Another contribution can be due to the ferromagnetic-metal to paramagnetic-insulator transitions of LSMO. These changes were more marked when the thickness of PZT was ultrathin in PZT/LSMO heterostructures [41].

6.5. FERROELECTRIC PROPERTIES

Figures 6.4 (a), (b) and (c) show the room-temperature ferroelectric polarization versus electric field (P-E) hysteresis loops for different thickness: (a) 80 nm, (b) 50 nm and (c) 20 nm. A clear ferroelectric hysteresis loops were observed in all films, with an increase in remnant polarization (P_r) and coercive field (E_c) with rising voltage. These measurements were made using Pt top electrodes. It was observed that with increase in the PZTFT thickness: i) an improvement occurs in saturation of the P - E loop; ii) an enhancement in P_r values is observed and; iii) a reduction in the coercive field occurs. The values of P_r and E_c were 10, 55, and 65 $\mu\text{C}/\text{cm}^2$ and 670, 640 and 500 kV/cm for 20, 50 and 80 nm of PZTFT thickness under applied electric field of 2000 kV/cm (Figure 6.5(a) and (b)). These values of P_r are in the range of many reported for both polycrystalline and epitaxial pure PZT, with P_r values from 15 to 70 $\mu\text{C}/\text{cm}^2$ grown by PLD [49-52]. The excellent ferroelectric properties of PZTFT were also reported in ceramic and thick films for our group and collaborators [31-37]. An enhancement of the polarization can be attributed to the larger orthorhombic distortion and the in-plane epitaxial strain of the PZTFT unit cell, due to the increased concentration of ferroelectric domains and the

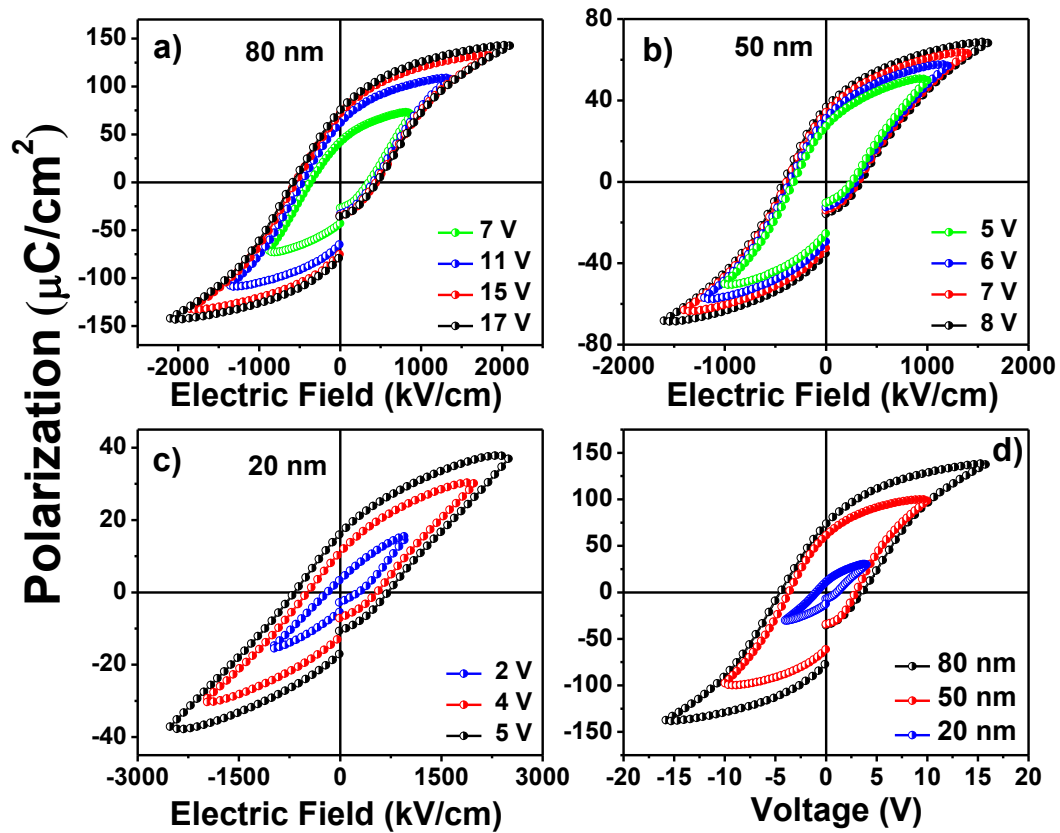


Figure 6.4. The ferroelectric hysteresis loops for different thickness (a) 80 nm, (b) 50 nm and (c) 20 nm PZTFT at room temperature. An increase in remnant polarization and coercive field was observed with increasing voltage. (d) The reduction of the polarization when the thickness of PZTFT is reduced to 20 nm.

distortions in the B-site (e.g. Ti^{4+} , Zr^{4+} , Fe^{3+} , and Ta^{5+}) in the ABO_3 crystal structure. The resultant chemical strain from the structure variation can enhance the polar displacement of Pb^{2+} ions at the A-site, and as a result, increase polarization [53, 54]. The decrease of P_r and increase of E_c when the thickness of PZTFT is reduced to 20 nm can be explained by the effect of the passive layer (also called the low-dielectric or dead-layer) originating at the interfaces between PZTFT and top/bottom electrodes (Pt/PZTFT and PZTFT/LSMO)

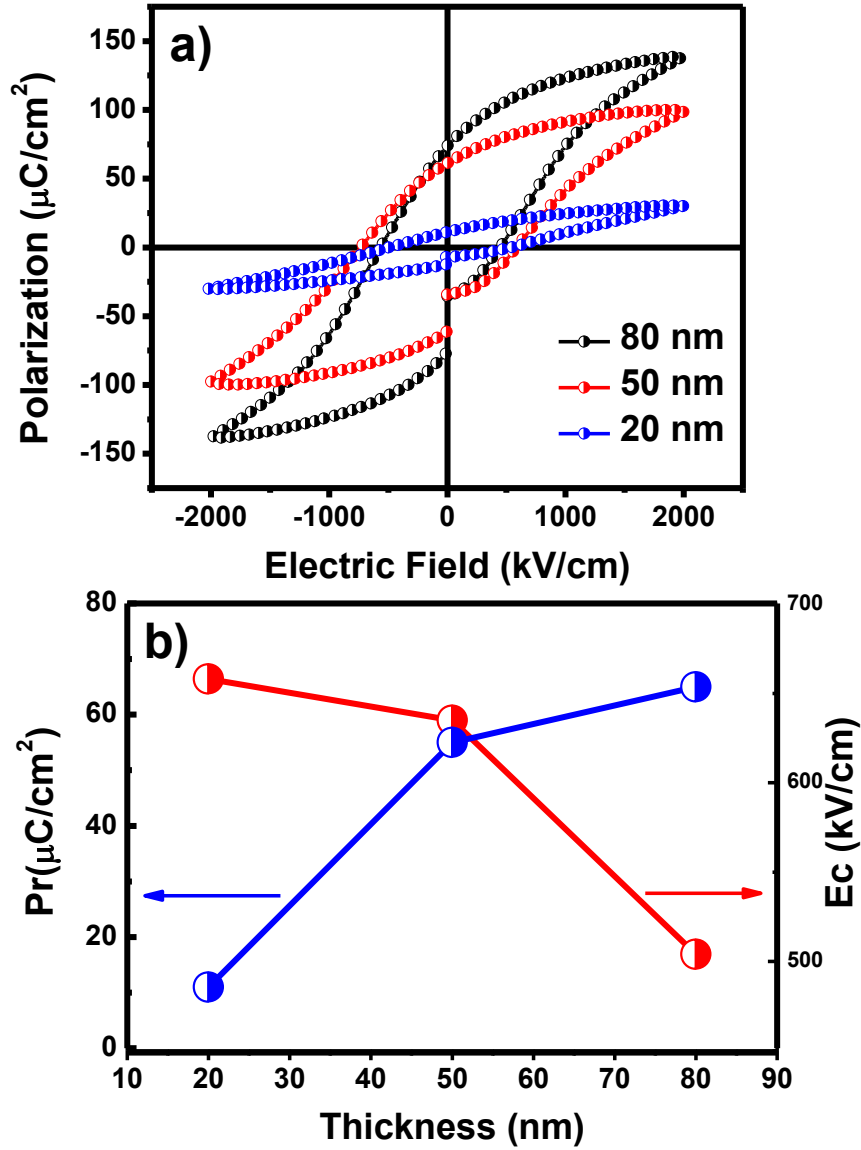


Figure 6.5. Shows the values of remnant polarization and coercive field for different thicknesses of PZTFT. The ferroelectric properties are dependent on the grain size of the films; this behavior has been reported by many researchers.

[55, 56]. A decrease in P_r and increase in E_c has been observed by other researchers for thickness of pure PZT ranging between 100 nm to 4 μm [46, 57, 58]. As the thickness of PZTFT layer decreases at this very thin level, the role of the passive layer is more important: due to the drop of the potential across of the passive layer, a higher voltage is

needed across the capacitor to switch the PZTFT layers. For this reason, one expects E_c to increase. In the other situation when the thickness of the PZTFT layer increases, the effect of a passive layer is diminished, with an enhancement in both domains wall mobility and switching with consequent reduction of the E_c value.

For comparison Figure 6.4(d) shows the hysteresis loops for 20, 50 and 80 nm PZTFT at different voltages. These results show that PZTFT has good ferroelectric properties at room temperature.

6.6. MAGNETIC PROPERTIES

Figure 6.6 (a) and (b) shows the magnetization versus magnetic field (M - H) curves of PZTFT/LSMO hetero-structures for different PZTFT thicknesses: 20, 50, and 80 nm at 5 and 300 K of temperatures, respectively. All samples show a slim, open, and well defined ferromagnetic loops, for the complete range of magnetic fields used (Figure 6.7 (a) and (b)). These samples have different contributions for the magnetism: i) the ferromagnetic LSMO (100 nm) layer that was kept constant in all thin films; ii) the magnetization of PZTFT layers (Figure 6.8(a) and (b)), the magnetic properties of PZTFT in both ceramic and thick films forms, at room temperature were shown by our group and collaborators [31-37]; and iii) the interface effect (changes in the lattice strain, chemical bonding and charge modulation). The magnetization values were normalized to the volume of the LSMO and PZTFT layers. A diminution in remnant magnetization (M_r) was observed with decrease of thickness of PZTFT. The M_r values were 287, 362, and 420 emu/cm³ for

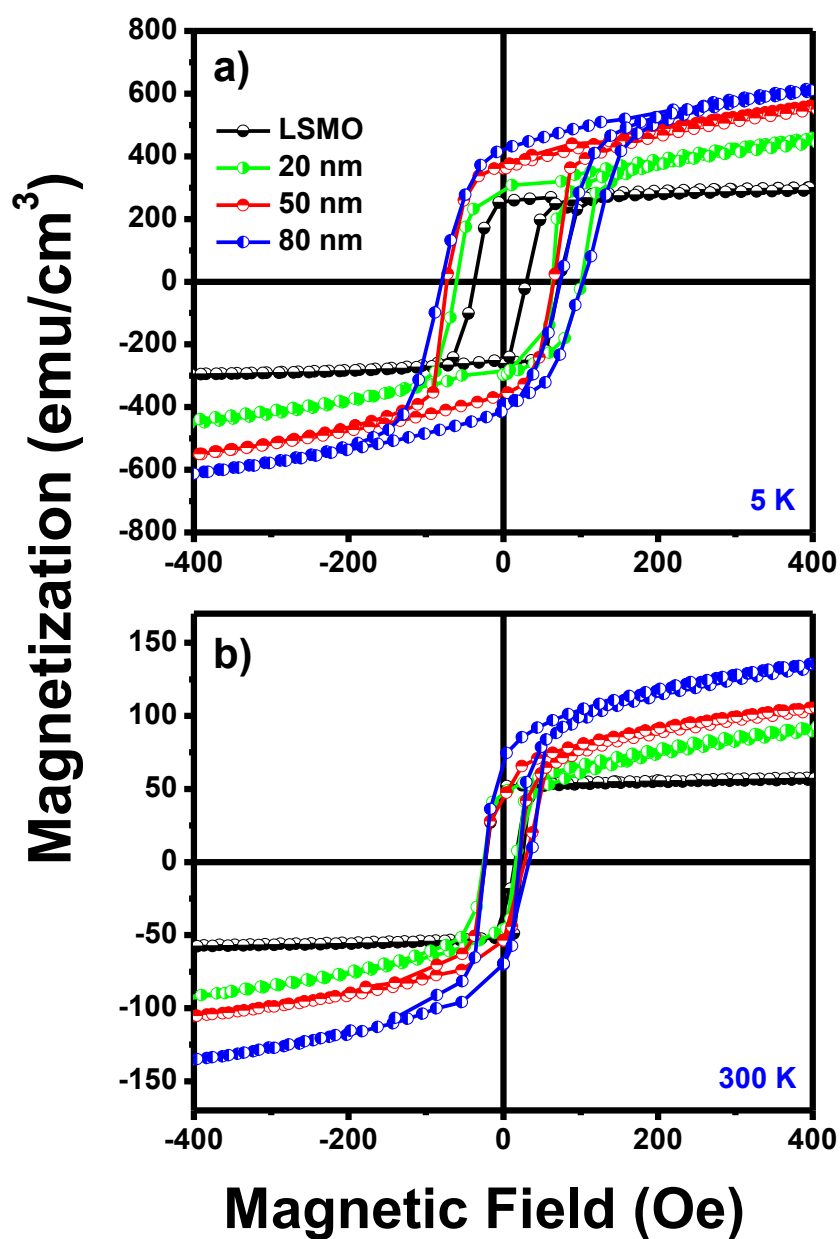


Figure 6.6. The magnetization versus magnetic field for PZTFT/LSMO hetero-structures at (a) 5K and (b) 300 K for different thicknesses of PZTFT. In all samples ferromagnetic behavior and a decrease in saturated magnetization was observed with decreasing PZTFT thickness.

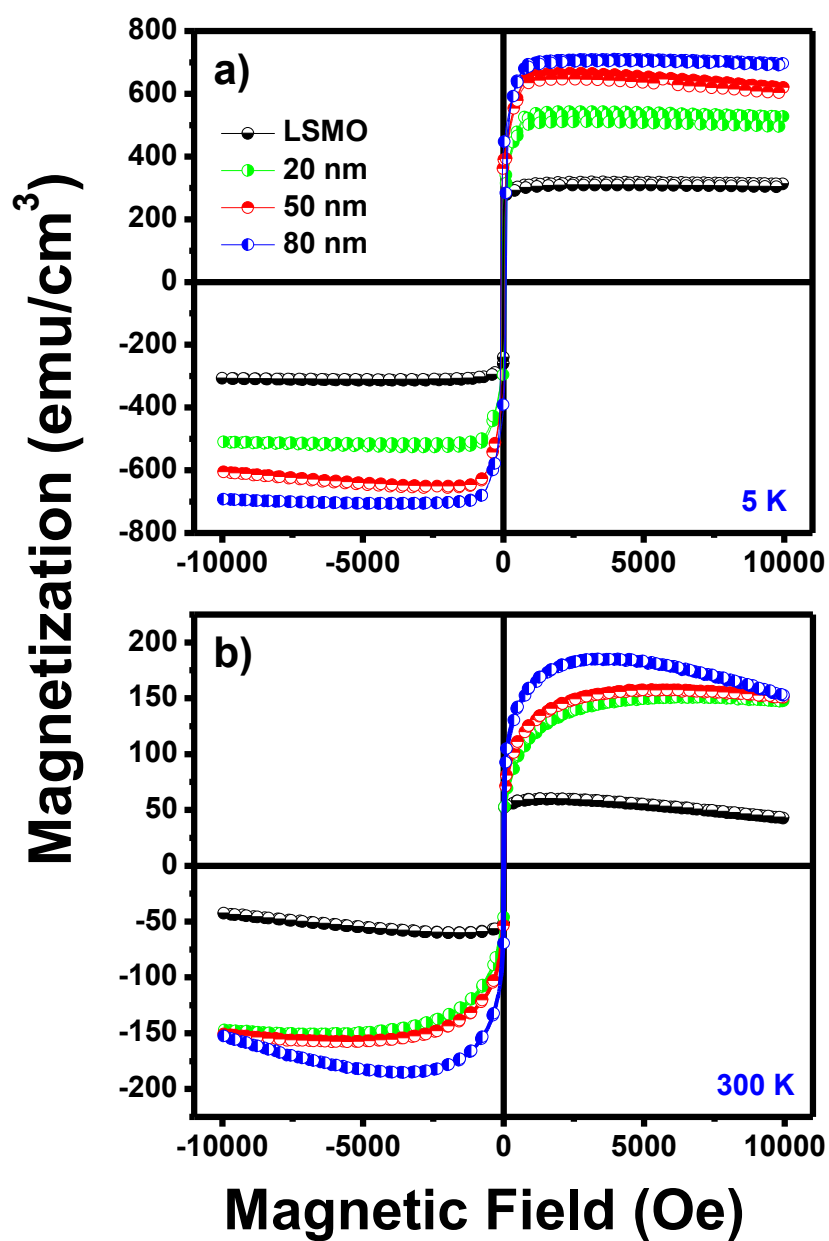


Figure 6.7. Magnetization versus magnetic field for the range (-10 to 10 k Oe); the ferromagnetic properties of the LSMO and PZTFT/LSMO hetero-structures for different thicknesses of PZTFT at (a) 5 K and (b) 300 K.

thickness of PZTFT 20, 50, and 80 nm at 5 K (Figure 6.6(a)), respectively. At 300K (Figure 6.6(b)), the M_r values were 46, 47 and 64 emu/cm³. Also, an enhancement of coercive field (H_C) was obtained when increase the thickness of PZTFT. The H_C values were 74, 78 and 92 Oe for thickness of PZTFT 20, 50, and 80 nm at 5 K (Figure 6.6(a)), respectively. Similar behavior was observed at 300K (Figure 6.6(b)), where the values were 19, 24 and 27 Oe. Sanchez et al. [34] have reported in PZTFT ceramics the ferromagnetic hysteresis loop at room temperature. This material has a good remnant magnetization of 0.024 emu/g. The room temperature magnetization value of 0.4 Bohr magnetons (μ_B) per Fe³⁺ spin, using known density of 7.5 g/cm³ and unit cell volume of 64×10^{-18} cm³, is quite reasonable. This magnetization is equivalent to about 7 % of the maximum saturation value of 5.9 μ_B for all Fe spins aligned at T= 0. The Fe³⁺ ions are known to cluster in pure PbFe_{1/2}Ta_{1/2}O₃, which is responsible for the relatively high magnetic ordering temperature for only 15-20 % Fe-occupation of the B-site in these specimens. The remnant magnetization value of PZTFT is comparable to the known room temperature multiferroics including bismuth ferrite and other lead-based multiferroic relaxors [59-61].

Huijben et al. [62] have studied BFO(25 nm)/LSMO(5 nm) and PbZr_{0.2}Ti_{0.8}O₃ (PZT)/LSMO heterostructures. These heterostructures show an enhancement in coercive field (H_C), compared to the single LSMO layer. It is however important to note that at all temperatures the BFO/LSMO heterostructures show a larger H_C compared to the PZT/LSMO heterostructures, hinting at an additional contribution from magnetic interactions across the interface, as the effective polarization is similar in this direction. Although an exchange bias interaction is observed between LSMO and BFO, it is not

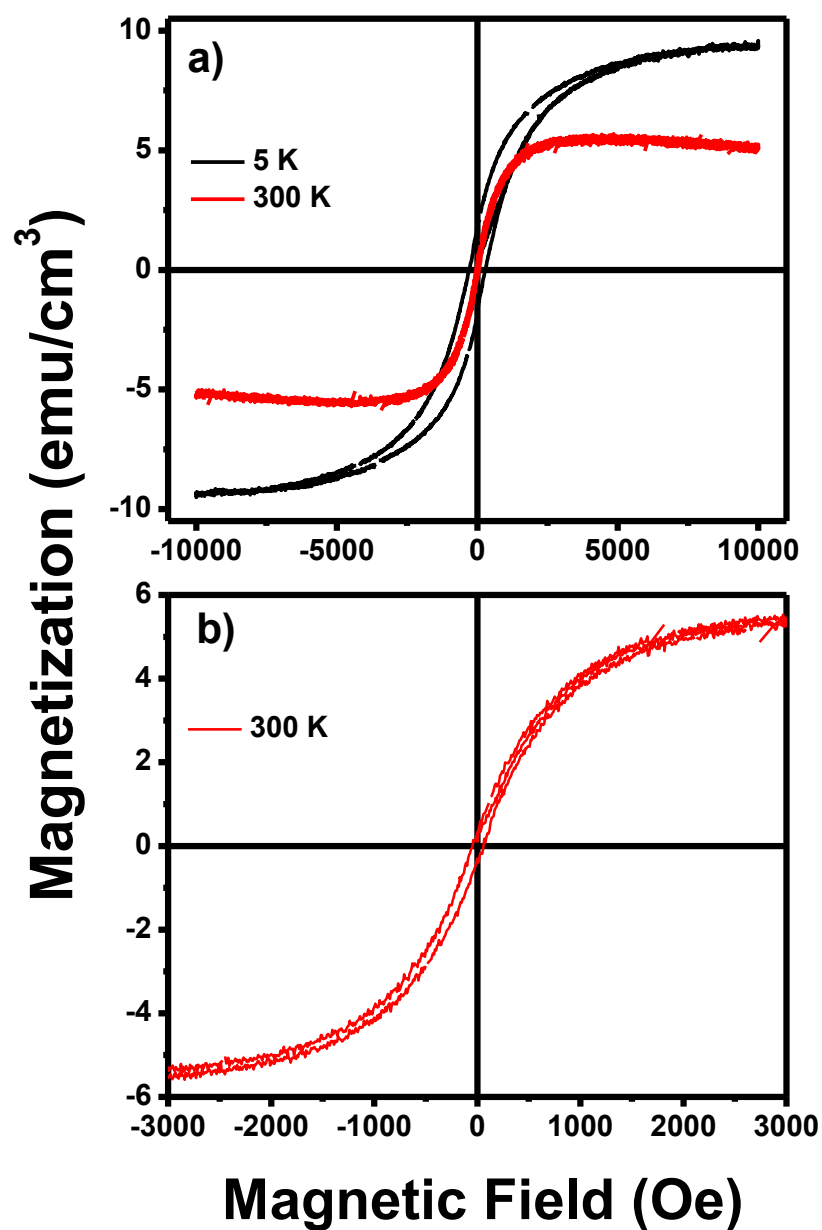


Figure 6.8. Magnetization versus magnetic field for pure PZTFT 300 nm thick at (a) 5 K and 300 K showing the ferromagnetic properties of the PZTFT films; (b) the small hysteresis loop at room temperature.

present in the case of a single LSMO layer or PZT/LSMO heterostructure. The fact that the exchange bias shifts are observed only in heterostructures of the ferromagnet LSMO together with the ferroelectric/antiferromagnetic BFO and not with the ferroelectric PZT points to the integral role that the antiferromagnetic properties of the BFO play in determining the properties of such heterostructures. Similar behavior could be occurring in our PZTFT/LSMO heterostructures, like BFO, PZTFT is a single-phase multiferroic at room temperature. Other contributions to the enhancement of the saturated magnetization with increase in thickness of PZTFT could be attributed to the exchange bias originating from the PZTFT/LSMO heterostructure, which suggests ferromagnetic alignment between the pinned spins of the ferromagnetic LSMO and PZTFT.

The temperature dependence of the magnetization measured under the zero-field-cooled (ZFC) and field-cooled-cooling (FCC) conditions are shown in Figure 6.9(a). The ZFC and FCC curves were measured by warming (5 to 390 K) and cooling (390 to 5 K) the samples at 100 Oe, respectively. An irreversibility clearly appears, as evidenced by the nonzero difference between the FCC and ZFC magnetizations. The FCC and ZFC curves do not vary monotonously; they initially decrease with temperature and increase before reaching the maximum and finally decrease again once the maximum is passed, due to the transition to the paramagnetic phase. This behavior is related to the increase of magnetic domain wall mobility at low magnetic fields upon heating, thus leading to an increase in the ZFC magnetization activated by the thermal process.

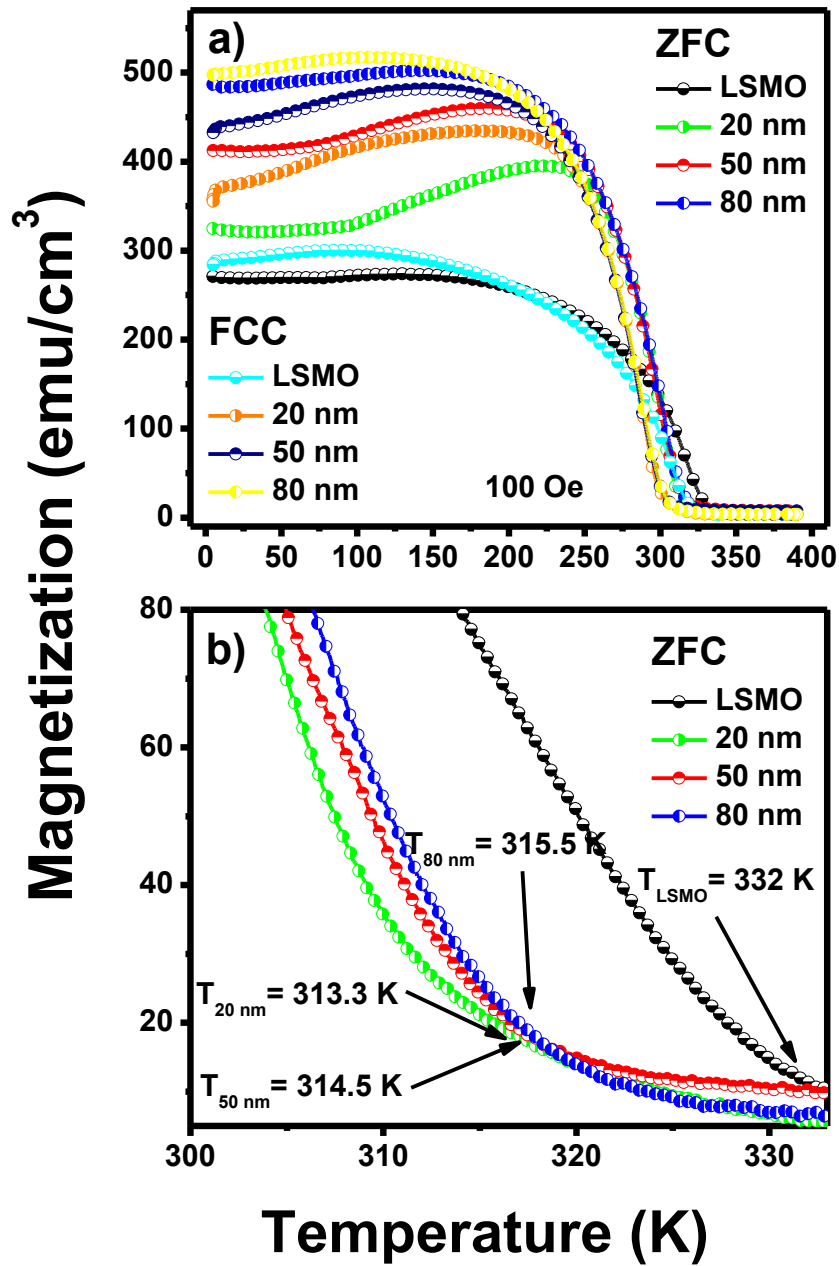


Figure 6.9. The magnetization versus temperature for PZTFT/LSMO hetero-structures for different thicknesses of PZTFT. (a) The irreversible ZFC and FCC curves show the presence of glassy behavior; (b) The transition temperature decreases when the PZTFT thickness was decreased.

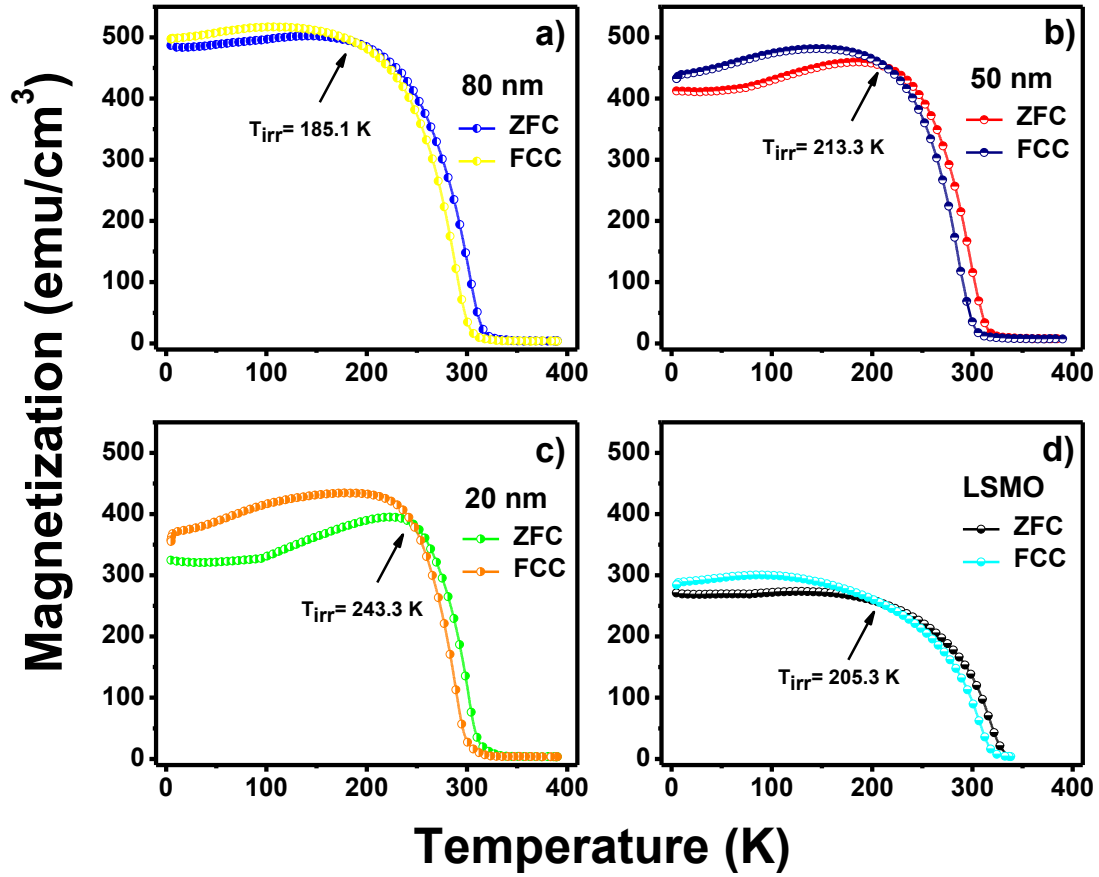


Figure 6.10. The magnetization versus temperature for PZTFT/LSMO hetero-structures for different thicknesses of PZTFT. The irreversible ZFC and FCC curves show the presence of glassy behavior. Ergodic temperature increases when the PZTFT thickness was decreased.

The results in Figure 6.9 (a) indicate that the interactions between spins become nonhomogeneous below a certain temperature depending of the thickness of the PZTFT films. The thermal irreversibility in the ZFC and FCC magnetizations (Figure 6.10) shows that the ferromagnetic order in PZTFT/LSMO heterostructures is affected by some glassy behavior.

The irreversible behavior of the magnetization in the PZTFT/LSMO heterostructures can be explained as follows: Under the ZFC condition, the directions of the spins in the spin-glass region are randomly oriented, and thus the spins in the spin-glass region are randomly coupled with the spins of the ferromagnetic region near the interface. Such random coupling makes the motion of the domain walls unfavorable. As a result, for decreasing temperature the ZFC magnetization becomes small (Figure 6.9(a)) and the coercive field becomes large, as shown above for 5 and 300 K. Under the FCC condition, the directions of the spins in the spin-glass region tend to align more with the external field, so the randomness in the magnetic coupling between the ferromagnetic and the spin-glass regions is diminished. Consequently, the magnetic domains move more easily, allowing the FCC magnetization to become large. However, the coercivity remains large because the directions of the spins in the spin-glass region are still random, even under the FCC condition. Also, the transition temperature decreases when the PZTFT thickness was decreased (Figure 6.9(b)). For another hand, the transition temperature of 300 nm thick pure PZTFT (Figure 6.11) have similar behavior of the ceramic-lamella reported [36].

6.7. MULTIFERROIC PROPERTIES AT NANOSCALE LEVEL.

Figure 6.12(a) shows the switching polarization of 7 nm thick PZTFT. This measurement was carried out by piezoresponse force microscopy at room temperature. This result shows the ferroelectric properties of PZTFT at the nanoscale thickness level. For ferroelectric ultrathin films finite screening occurring at ferroelectric/electrode

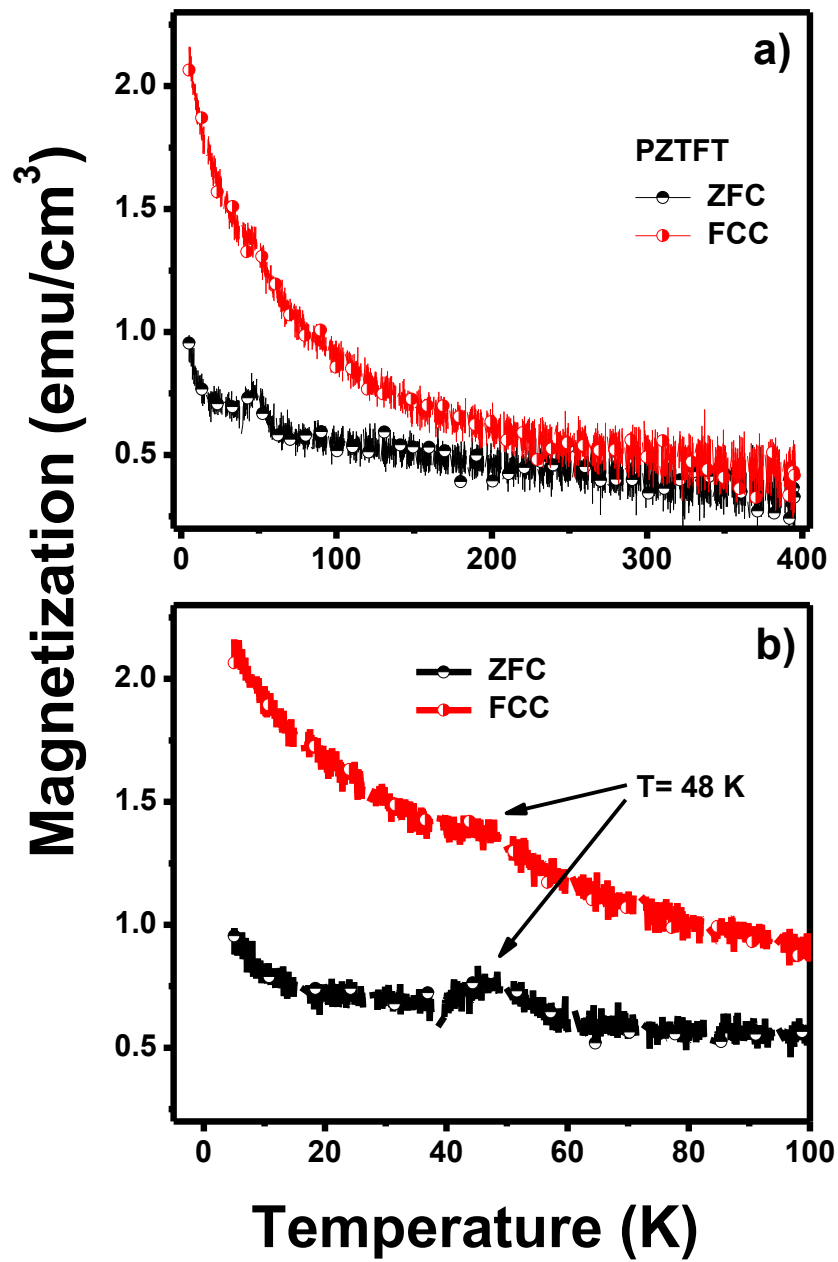


Figure 6.11. (a) and (b) show the magnetization versus temperature of 300 nm thick pure PZTFT films.

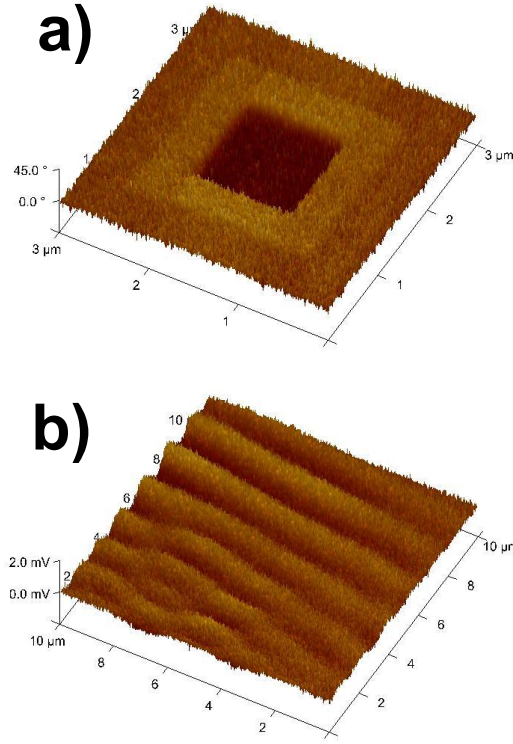


Figure 6.12. The multiferroic properties of ultrathin 7-nm PZTFT films. (a) Shows the switching polarization of 7-nm PZTFT using piezoresponse force microscopy, and (b) displays the stripe magnetic domains for ultrathin 7-nm PZTFT using magnetic force microscopy.

interfaces more significantly affect the ferroelectric stability. Incomplete compensation of the polarization charges happens due to the finite screening at ferroelectric/electrode interfaces, inducing a depolarization field E_d against the polarization inside the ferroelectric. Depolarization fields exist in all ferroelectric thin films, and this effect is higher in thinner films [63-65].

Further, Figure 6.12(b) shows stripe magnetic domains for ultrathin 7-nm of PZTFT film. This measurement was done by magnetic force microscopy at room temperature. It displays the magnetic properties of PZTFT at nanoscale level that is required for potential nano-devices.

6.8. TRANSPORT PROPERTIES

The study of conduction mechanisms in dielectric films is very important for different device applications (e.g. multiferroic tunnel junctions). There are three main types of conduction mechanisms in dielectric films: i) space-charge-limited (bulk-limited); ii) Poole-Frenkel bulk, and iii) interface-limited (Schottky and/or Simmons) [66]. The bulk-limited conduction mechanism depends on the electrical properties of the dielectric itself. Based on this type of conduction mechanism, some important electrical properties in the dielectric films can be extracted, including the dielectric relaxation time, the electronic drift mobility, and the density of states in the conduction band. For this type of conduction mechanism, we consider first space charge-limited conduction (SCLC), and afterwards, Poole-Frenkel.

Let us look initially at the voltage dependence: The $\ln J - \ln E$ plotted, where J is the density current and E is the electric field, for space-charge-limited current is shown in Figure 6.13. This conduction mechanism can be governed by two laws: Ohm's law ($J_{Ohm} \propto E$) for low electric field, and Child's law ($J_{Child} \propto E^2$) for high electric field.

$$J_{Ohm} = n_0 \mu e E \quad (\text{Ohm's law}) \quad (6.1)$$

$$J_{Child} = \frac{9}{8} \mu \epsilon_0 \epsilon_r \frac{E^2}{d} \quad (\text{Child's law}) \quad (6.2)$$

where n_0 is the concentration of the free charge carriers in thermal equilibrium; μ , the mobility of the charge carriers; e , the charge of the electron; E , the applied electric field; d , the thickness of thin films; ϵ_0 , the permittivity of free space; and ϵ_r is the relative dielectric constant of the thin film. At low applied electric field the plots are linear with a slope around 1 (Figure 6.13 (b)), indicating that Ohm's law may govern in this range of electric field (note however, that Schottky/Simmons conduction is also linear at low

fields E and is certainly not ohmic). This implies that the density of thermally generated free carriers inside of the films is larger than the injected carriers [67]. This ohmic-like behavior takes place in the electrically quasi-neutral state corresponding to the situation when trap centers are filled at weak injection. In this region the carrier transit time is larger than the dielectric relaxation time. This implies that the injected carrier density is small in comparison with free carriers and that the injected carriers will redistribute themselves with a tendency to maintain electric charge neutrality internally in a time comparable to the dielectric relaxation time. Therefore, the injected carriers have no chance to travel across the insulator. The redistribution of the charge is known as dielectric relaxation. The ohmic behavior can be observed only after these space charge carriers become trapped. When the transition from the ohmic to the space-charge limited region occurs, the carrier transit time at electric field transition ($E_t = 0.5$ MV/cm) of the linear to quadratic behavior becomes equal to the dielectric relaxation time. The traps are filled up and a space charge appears. The injected excess carriers dominate the thermally generated carrier since the injected carrier transit time is too short for their charge to be relaxed by the thermally generated carriers. The increase of electric field may increase the density of free carriers resulting from injection to such a value that the Fermi level moves up above the electron trapping level. It can be understood that after all traps are filled up, the subsequently injected carriers will be free to move in the dielectric films, so that at the sub-threshold voltage (voltage required to fill the traps or, the voltage at which Fermi level passes through trapping level) to set on this transition, the current will rapidly jump from its low trap limited value to a high trap-free space-charge-limited current.

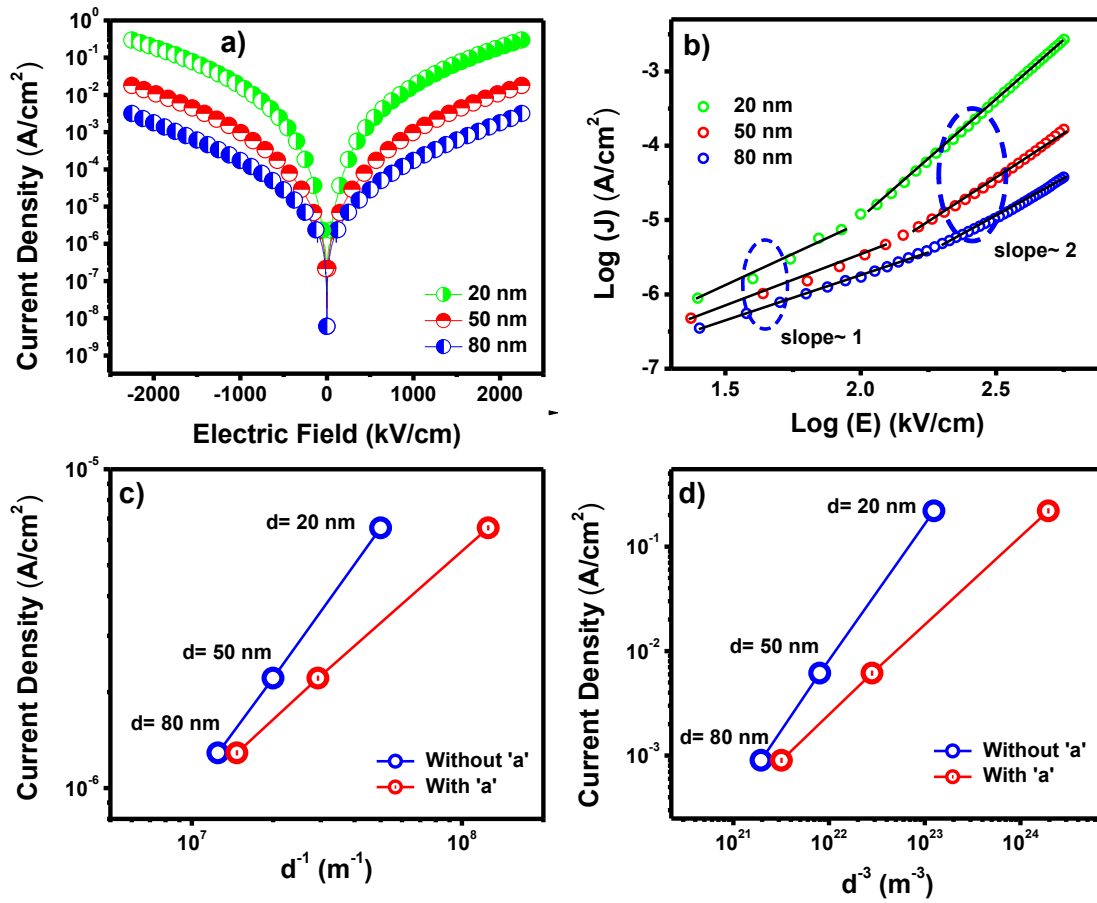


Figure 6.13. (a) The J vs. E plots for different thickness of PZTFT; (b) The $\ln J$ vs. $\ln E$ plots for space-charge-limited conduction (SCLC); Thickness dependence $I(d)$ for the leakage current in PZTFT. c) In the linear region (slope ~ 1 in (b)), the upper curve assumes d is the film thickness and yields $d^{-1.3}$, whereas the lower curve assumes ~ 7 nm accommodation length a and gives the expected space-charge-limited d^{-1} dependence. d) The quadratic region (slope ~ 2 in (b)), the upper curve yields $d^{-3.8}$, whereas the lower curve assumes ~ 7 nm accommodation a and gives d^{-3} dependence.

In the high electric field (more than 0.5 MV/cm), all traps are filled and the conduction becomes the space-charge-limited (Child's law). Hence a space charge layer in the dielectric builds up and the electric field cannot be observed as constant any longer. Further, when the traps gradually saturate, which means that the Fermi-level gets closer to the bottom of the conduction band, this results in a strong increase of the number of free electrons, thus explaining the increase of the current. The current is fully controlled

by the space charge, which limits the further injection of free carriers in the dielectric. We obtained the mobility of the PZTFT using Equation 6.2 (Child's law), where ϵ_r (the low frequency dielectric constant) was taken from the Figure 3(a); for 80 nm thickness of PZTFT that value is about 300. The mobility found was $9.2 \times 10^{-7} \text{ cm}^2/\text{V.s}$, this value agrees rather well with that $1 \times 10^{-6} \text{ cm}^2/\text{V.s}$ for pure PZT films [68]. This value of mobility (μ) was replaced in Equation 6.1 (Ohm's law), giving the concentration of free charge carriers (n_0) as $2.1 \times 10^{18} \text{ cm}^{-3}$. These values are comparable with those in pure PZT obtained from other works [69, 70]. This might suggest that in the bulk-limited conduction regime SCLC describes our data. Also, this is compatible with the thickness dependence of $J(V)$. For SCLC conduction J must vary rather precisely as V/d at low fields and V^2/d^3 at high fields. In the low-field linear regime (Figure 6.13(b)), the d -dependence at constant E over a wide range of E is linear in $1/d$ (Figure 6.13(c)). For high-field quadratic regime (Figure 6.13(b)), the d -dependence at constant E over a wide range of E is cubic in $1/d^3$ (Figure 6.13(d)); for example, at 700 kV/cm, we found the current ratio of different thickness of PZTFT, $I_{20\text{nm}}/I_{80\text{nm}}=(d_{80\text{nm}}/d_{20\text{nm}})^3=64.9$, this is very close to 64, $I_{20\text{nm}}/I_{50\text{nm}}=(d_{50\text{nm}}/d_{20\text{nm}})^3=16.3$, close to 15.6, and $I_{50\text{nm}}/I_{80\text{nm}}=(d_{80\text{nm}}/d_{50\text{nm}})^3=4.0$, very close to 4.01.

Hence, we see that based upon current-voltage $J(V)$ data alone, it is difficult to distinguish between interface-limited Schottky conduction (Simmons' limit of small electron mean free path) and bulk-limited SCLC; both give plausible numbers (as does Poole-Frenkel). However, as discussed elsewhere by one of us, [66] the thickness dependence at constant field for small E for SCLC predicts current proportional to $1/d$, whereas Schottky-Simmons is nearly independent of thickness d (it is limited by two

electrode interfaces and nearly independent of how thick the dielectric is between these two electrodes). Figure 8(c)-(d) shows that for all fields used, the current versus thickness at constant field E differ of the SCLC prediction, assuming that the voltage drop is uniform across the whole sample; but a more precise analysis [66] incorporates an “accommodation length” a at each electrode interface, such that $1/(d-2a)$ was predicted, where a is typically a few nm. In order to explain the thickness dependence observed in Figure 8(c)-(d), we found that a is approximately 7 nm for the PZTFT 20, 50, and 80 nm films. It shows that the mechanism is SCLC, whereas it rules out both Schottky/Simmons and Poole-Frenkel. Poole-Frenkel is a bulk mechanism, so it depends strongly upon film thickness d . It is of form $J = \frac{V}{d} \exp\{[a-(bV/d)^{1/2}]/kT\}$ and hence varies more rapidly than $1/d$ at constant voltage; but it is independent of d at constant field $E = V/d$.

REFERENCES

1. T. Kimura, T. Goto, H. Shintani, K. Ishizaka, T. Arima, Y. Tokura, *Nature* **426**, 55 (2003).
2. H. Zheng, J. Wang, S. E. Lofland, Z. Ma, L. Mohaddes-Ardabili, T. Zhao, L. Salamanca-Riba, S. R. Shinde, S. B. Ogale, F. Bai, D. Viehland, Y. Jia, D. G. Schlom, M. Wuttig, A. Roytburd, R. Ramesh, *Science* **303**, 5658 (2004).
3. N. A. Spaldin, M. Fiebig, *Science* **309**, 391 (2005).
4. M. Fiebig, *J. Phys. D: Appl. Phys.* **38**, R123-R152 (2005).
5. W. Eerenstein, N. D. Mathur, J. F. Scott, *Nature (London)* **442**, 759 (2006).
6. S. W. Cheong, M. Mostovoy, *Nat. Mater.* **6**, 13 (2007).
7. R. Ramesh, N. A. Spaldin. *Nat. Mater.* **6**, 21 (2007).
8. W. Eerenstein, M. Wiora, J. L. Prieto, J. F. Scott, N. D. Mathur, *Nat. Mater.* **6**, 348 (2007).
9. J. F. Scott, *Nat. Mater.* **6**, 256 (2007).
10. G. Radaelli, D. Petti, E. Plekhanov, I. Fina, P. Torelli, B. R. Salles, M. Cantoni, C. Rinaldi, D. Gutiérrez, G. Panaccione, M. Varela, S. Picozzi, J. Fontcuberta, R. Bertacco, *Nature Commun.* **5**, 3404 (2014).
11. S. W. Yang, R. C. Peng, T. Jiang, Y. K. Liu, L. Feng, J. J. Wang, L. Q. Chen, X. G. Li, C. W. Nan, *Adv. Mater.* **26**, 7091 (2014).
12. R. O. Cherifi, V. Ivanovskaya, L. C. Phillips, A. Zobelli, I. C. Infante, E. Jacquet, V. Garcia, S. Fusil, P. R. Briddon, N. Guiblin, A. Mougin, A. A. Ünal, F. Kronast, S. Valencia, B. Dkhil, A. Barthélémy, M. Bibes, *Nature Materials* **13**, 345-351 (2014).
13. J. T. Heron, M. Trassin, K. Ashraf, M. Gajek, Q. He, S. Y. Yang, D. E. Nikonov, Y-H. Chu, S. Salahuddin, R. Ramesh, *Phys. Rev. Lett.* **107**, 217202 (2011).
14. J. F. Scott, *J. Mater. Chem.* **22**, 4567 (2012).
15. M. Bibes, A. Barthélémy, *Nat. Mater.* **7**, 425 (2008).
16. H. J. Zhao, W. Ren, Y. Yang, J. Íñiguez, X. M. Chen, L. Bellaiche, *Nature Commun.* **5**, 4021 (2014).
17. N. D. Mathur, J. F. Scott, *Phil. Trans. R. Soc. A* **372**, 20120453 (2014).

18. J. F. Scott, *EPL* **103**, 37001 (2013).
19. J. F. Scott, *ISRN Materials Science* **2013**, 187313 (2013).
20. J. Ma, J. Hu, Z. Li, C.W. Nan, *Adv Mater.* **23**, 1062 (2011).
21. J. F. Scott, *NPG Asia Mater.* **5**, 72 (2013).
22. A. Roy, R. Gupta, A. Garg, *Advances in Condensed Matter Physics* **2012**, 926290 (2012).
23. M. Gich, I. Fina, A. Morelli, F. Sánchez, M. Alexe, J. Gàzquez, J. Fontcuberta, and A. Roig, *Adv. Mater.* **26**, 4645 (2014).
24. Y. Wang, J. Hu, Y. Lin and C. W. Nan, *NPG Asia Materials* **2**, 61 (2010).
25. R. Saha, A. Sundaresan, C. R. Rao, *Mater. Horiz.* **1**, 20 (2014).
26. T. Kimura, Y. Sekio, H. Nakamura, T. Siegrist, A. P. Ramirez, *Nat. Mater.* **7**, 291 (2008).
27. C. Ederer, N. A. Spaldin, *Phys. Rev. B* **71**, 060401 (2005).
28. J. P. Velez, S. S. Jaswal, E. Y. Tsymlal, *Phil. Trans. R. Soc. A* **369**, 3069 (2011).
29. S. P. Jones, S. M. Gaw, K. I. Doig, D. Prabhakaran, E. M. Hétyroy Wheeler, A. T. Boothroyd, J. Lloyd-Hughes, *Nat Commun.* **5**, 3787 (2014).
30. G. Catalan, J. F. Scott, *Adv. Mater.* **21**, 2463 (2009).
31. D. Sanchez, A. Kumar, N. Ortega, R. S. Katiyar, J. F. Scott, *Appl. Phys. Lett.* **97**, 202910 (2010).
32. D. Sanchez, N. Ortega, A. Kumar, G. Sreenivasulu, R. S. Katiyar, J. F. Scott, D. M. Evans, Miryam Arredondo-Arechavala, A. Schilling, J. M. Gregg, *J. Appl. Phys.* **113**, 074105 (2013).
33. D. M. Evans, A. Schilling, A. Kumar, D. Sanchez, N. Ortega, M. Arredondo, R. S. Katiyar, J. M. Gregg, J. F. Scott, *Nature Commun.* **4**, 1534 (2013).
34. D. Sanchez, N. Ortega, A. Kumar, R. Roque-Malherbe, R. Polanco, J. F. Scott, Ram S. Katiyar, *AIP Advances* **1**, 042169 (2011).
35. D. M. Evans, A. Schilling, A. Kumar, D. Sanchez, N. Ortega, R. S. Katiyar, J. F. Scott, J. M. Gregg, *Phil. Trans. R. Soc. A* **372**, 20120450 (2014).

36. J. Schiemer, M. A. Carpenter, D. M. Evans, J. M. Gregg, A. Schilling, M. Arredondo, M. Alexe, D. Sanchez, N. Ortega, R. S. Katiyar, M. Echizen, E. Colliver, S. Dutton, J. F. Scott, *Adv. Funct. Mater.* **24**, 2993 (2014).
37. D. M. Evans, M. Alexe, A. Schilling, A. Kumar, D. Sanchez, N. Ortega, R. S. Katiyar, J. F. Scott, J. M. Gregg, *Adv. Mater.* **27**, 6068 (2015).
38. M. Gajek, M. Bibes, S. Fusil, K. Bouzehouane, J. Fontcuberta, A. Barthélémy, A. Fert, *Nat. Mater.* **6**, 296 (2007).
39. D. M. Kim, C. B. Eom, V. Nagarajan, J. Ouyang, R. Ramesh, V. Vaithyanathan, D. G. Schlom, *Appl. Phys. Lett.* **88**, 142904 (2006).
40. R. Scherwitzl, P. Zubko, I. G. Lezama, Sh. Ono, A. F. Morpurgo, G. Catalan, J. M. Triscone, *Adv. Mater.* **22**, 5517 (2010).
41. D. Barrionuevo, N. Ortega, A. Kumar, R. Chatterjee, J. Scott, and R. S. Katiyar, *J. Appl. Phys.* **114**, 234103 (2013).
42. Y. W. Li, Z. G. Hu, F. Y. Yue, G. Y. Yang, W. Z. Shi, X. J. Meng, J. L. Sun, J. H. Chu, *Appl. Phys. Lett.* **91**, 232912 (2007).
43. M. Abazari, A. Safari, *J. Appl. Phys.* **105**, 094101 (2009).
44. D. Guo, C. Wang, Q. Shen, L. Zhang, M. Li, J. Liu, *Appl. Phys. A* **97**, 877 (2009).
45. S. Majumdar, H. Huhtinen, P. Paturi, H. S. Majumdar, *J. Mater. Science* **48**, 2115 (2013).
46. J. Pérez de la Cruz, E. Joanni, P. M. Vilarinho, A. L. Kholkin, *J. Appl. Phys.* **108**, 114106 (2010).
47. C-R Cho, W-J Lee, B-G Yu, B-W Kim, *J. Appl. Phys.* **86**, 2700 (1999).
48. H. Fujisawa, S. Nakashima, K. Kaibara, M. Shimizu, H. Niu, *Jpn. J. Appl. Phys.* **38**, 5392 (1999).
49. C. A. F. Vaz, Y. Segal, J. Hoffman, F. J. Walker, C. H. Ahn, *J. Vac. Sci. Technol. B* **28**, C5A6 (2010).
50. Z. J. Wang, H. Usuki, T. Kumagai, H. Kokawa, *J. Sol-Gel Sci. Technol.* **42**, 375 (2007).
51. J. Schwarzkopf, R. Fornari, *Prog. Cryst. Growth. Charact. Mater.* **52**, 159 (2006).

52. W. Wu, K. H. Wong, C. L. Choy, Y. H. Zhang, *Appl. Phys. Lett.* **77**, 3441 (2000).
53. J. K. Yang, W. S. Kim, H. H. Park, *Appl. Surf. Sci.* **169-170**, 544 (2001).
54. C. A. Randall, N. Kim, J. P. Kucera, W. Cao, T. R. Shrout, *J. Am. Ceram. Soc.* **81**, 677 (1998).
55. A. K. Tagantsev, M. Landivar, E. Colla, N. Setter, *J. Appl. Phys.* **78**, 2623(1995).
56. A. K. Tagantsev, L. E. Cross, J. Fousek, *Publisher Springer New York*, **2010**.
57. L. Ran, J. Gen-Shan, L. Bin, Z. Quan-Liang, Z. De-Qing, Y. Jie, C. Mao-Sheng, *Chin. Phys. Lett.* **29**, 058101 (2012).
58. T. Haccart, E. Cattani, D. Remiens, *Semicond. Phys. Quantum Electron.* **5**, 78. (2002).
59. R. Blinc, P. Cevc, A. Zorko, J. Holc, M. Kosec, Z. Trontelj, J. Pirnat, N. Dalal, V. Ramachandran, J. Krzystek, *J. Appl. Phys.* **101**, 033901 (2007).
60. M. Correa, A. Kumar, R. S. Katiyar, and C. Rinaldi, *Appl. Phys. Lett.* **93**, 192907 (2008).
61. R. Martinez, R. Palai, H. Huhtinen, J. Liu, J. F. Scott, R. S. Katiyar, *Phys. Rev. B* **82**, 134104 (2010).
62. M. Huijben, P. Yu, L. W. Martin, H. J. A. Molegraaf, Y. H. Chu, M. B. Holcomb, N. Balke, G. Rijnders, R. Ramesh, *Adv. Mater.* **25**, 4739 (2013).
63. R. R. Mehta, B. D. Silverman, J. T. Jacobs, *J. Appl. Phys.* **44**, 3379 (1973).
64. J. Junquera, P. Ghosez, *Nature* **422**, 506 (2003).
65. D. D. Fong, G. B. Stephenson, S. K. Streiffer, J. A. Eastman, O. Auciello, P. H. Fuoss, C. Thompson, *Science* **304**, 1650 (2004).
66. J. F. Scott, *J. Phys.: Condens. Matter* **26**, 142202 (2014).
67. M. A. Lambert, P. Mark, *Academic Press*, New York, USA. **1970**.
68. L. Pintilie, I. Vrejoiu, D. Hesse, G. LeRhun, M. Alexe, *Phys. Rev. B* **75**, 104103 (2007).
69. B. M. Melnick, J. F. Scott, C. A. Paz de Araujo, L. D. McMillan, *Ferroelectrics* **135**, 163 (1992).
70. S. K. Dey, R. Zuleeg, *Ferroelectrics* **112**, 309 (1992).

CHAPTER 7

7.1. CONCLUSIONS

- ❖ We have successfully growth, the ferroelectric $\text{PbZr}_{0.52}\text{Ti}_{0.48}\text{O}_3$ (PZT) thin films with various thicknesses ranging from 100 to 10 nm on $\text{La}_{0.67}\text{Sr}_{0.33}\text{MnO}_3/(\text{LaAlO}_3)_{0.3}(\text{Sr}_2\text{AlTaO}_6)_{0.7}$ (LSMO/LSAT) (001) substrates deposited by pulsed laser deposition technique.
- ❖ The effect of PZT thickness on the heterostructures properties was studied. X-ray diffraction analysis revealed that both PZT and LSMO films were well oriented along (001) plane; however, a gradually strengthening and sharpening diffraction pattern with slight shift to higher angles was observed with increase of PZT layers thickness.
- ❖ The frequency dependence of dielectric permittivity (real (ϵ') and imaginary (ϵ'')) showed that the ϵ' (ϵ'') increase from 68 (9.75) to 463 (39) when thickness of PZT increased from 10 nm to 100 nm at 10 kHz. The grain size and mechanical stress across different interfaces of PZT/LSMO/LSAT can be due to intrinsic effects responsible for the variation of dielectric properties.
- ❖ The anomalies observed in temperature-dependent ϵ' data in all PZT/LSMO heterostructures were assigned to LSMO T_{FM-PI} transition. Similar behavior was observed in the temperature dependent magnetization. The drastic decrease of

remanent polarization (P_r) and systematic increase of coercive field (E_c) in ultrathin films (~ 10 nm) may be due to the role of the passive layer between the ferroelectric layer and the electrode.

- ❖ An appreciable increase of saturated magnetization (M_s) was observed with the increase of PZT layer thickness at 300 K and 5 K. An enhancement in magnetization with increase in PZT thickness may be due to PZT/LSMO interface effects.
- ❖ We demonstrate the room temperature polar switching and tunneling in $\text{PbZr}_{0.52}\text{Ti}_{0.48}\text{O}_3$ (PZT) ultra-thin films of thickness 3-7 nm, sandwiched between platinum metal and ferromagnetic $\text{La}_{0.67}\text{Sr}_{0.33}\text{MnO}_3$ (LSMO) layers, which also shows magnetic field dependent tunnel current switching in $\text{Pt/PbZr}_{0.52}\text{Ti}_{0.48}\text{O}_3/\text{La}_{0.67}\text{Sr}_{0.33}\text{MnO}_3$ heterostructures.
- ❖ The epitaxial nature, surface quality and ferroelectric switching of all heterostructures films were examined with the help of X-ray diffraction (XRD) patterns, atomic force microscopy (AFM), and piezo force microscopy (PFM), respectively.
- ❖ The capacitance versus voltage graphs show butterfly loops above the coercive field ($> \pm 3$ V) of PZT for small probe area ($\sim 16 \mu\text{m}^2$). The effect of ferroelectric switching was observed in current density versus voltage curves with a large variation in high-resistance/low-resistance (HRS/LRS) ratio (2:1 to 100:1),

however, these effects were more prominent in the presence of in-plane external magnetic field. The conductance is fitted with Brinkman's model, and the parabolic conductance upon bias voltage implies electron tunneling governs the transport.

- ❖ Self-poled ultra-thin ferroelectric $\text{PbZr}_{0.52}\text{Ti}_{0.48}\text{O}_3$ (PZT) (5 and 7 nm) films have been grown on ferromagnetic $\text{La}_{0.67}\text{Sr}_{0.33}\text{MnO}_3$ (LSMO) (30 nm) to check the effect of polar capping on magnetization vital for ferroelectric tunnel junction (FTJ) devices.
- ❖ PZT/LSMO heterostructures with thick polar PZT (7 nm) capping show nearly 100% enhancement in magnetization compared with thin polar PZT (5 nm) films, probably due to excess hole transfer from the ferroelectric to the ferromagnetic layers.
- ❖ Core-level X-ray photoelectron spectroscopy (XPS) analysis revealed that 7-nm PZT capping generated excess holes from the polar layer to the magnetic layer producing large spin-orbit coupling ($\text{Mn}(3s)$) and more Mn^{4+} to Mn^{3+} transfer. In-plane compressive strain also decreased with increase in polar capping thickness, significantly modifying the PZT surface and PZT/LSMO interface.
- ❖ We have shown that the dielectric, ferroelectric, magnetic and transport properties of the single-phase multiferroic $\text{Pb}(\text{Zr}_{0.53}\text{Ti}_{0.47})_{0.60}(\text{Fe}_{0.5}\text{Ta}_{0.5})_{0.40}\text{O}_3$ (PZTFT) thin films change with different thicknesses.

- ❖ Due to evolution of device miniaturization and the potential application for new nonvolatile memory devices, this material can be used as a barrier in multiferroic tunnel junctions. Such devices have limitations in critical thickness (less than 8 nm) for ultrathin multiferroic tunnel barriers, which is vital to the properties and performance of this kind of memory.

- ❖ We show two things: (1) It remains a switching multiferroic at room temperature down to at least thickness $d = 7$ nm, thin enough for tunnel junctions; (2) both voltage and thickness dependence of leakage current density J confirm that it cannot be Simmons/Schottky interface-limited or Poole-Frenkel (bulk). The former requires thickness-independent current density J , and the latter requires that current be independent of d at constant field. The data satisfy space-charge-limited current (SCLC) in the linear voltage regime, or more precisely, vary as $1/(d-2a)$, where a is an accommodation length. A strong d -dependence is found over several decades of field and voltage, leading to an estimate of a . Which was estimated to be 7 nm for PZTFT films.